Removal of antimony from aqueous solutions as stable crystalline ferric antimonate ($FeSbO_4$) – tripuhyite

Ravinder S. Multani

Department of Mining and Materials Engineering

McGill University

Montreal, Quebec, Canada

December 2014

A thesis submitted to McGill University in partial fulfillment of the requirements of the degree of Master of Engineering

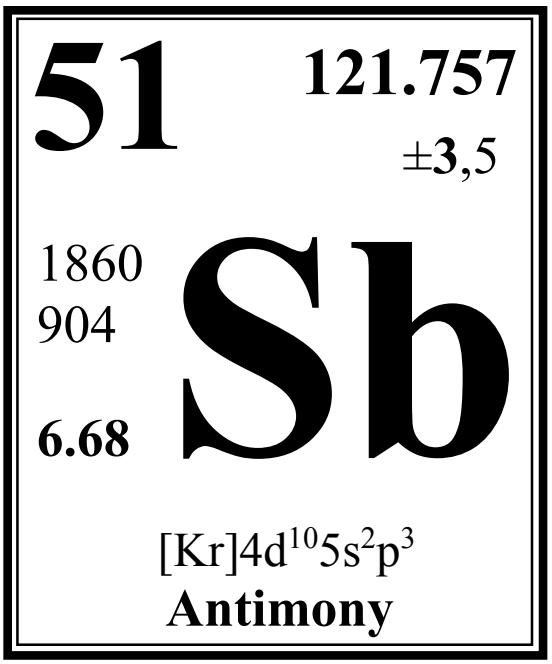
51
121.757
±3,5
1860
904
6.68
Sb
[Kr]4d10 5s2 p3
Antimony

Abstract

The scope of this research was to investigate the precipitation of antimony (Sb) from acidic aqueous solutions (6 $g \cdot L^{-1}$ Sb) as ferric antimonate, $FeSbO_4$ (tripuhyite), its further crystallization by hydrothermal treatment or calcination and the determination of its degree of leachability. This work was undertaken in order to assess the technical feasibility of isolating antimony from mineral and metallurgical process streams as an environmentally stable ferric antimonate compound.

Precipitation of ferric antimonate was studied over the pH range 1.5 – 5.3 at 95 °C via the co–oxidation of iron(II) and antimony(III) by drop–wise H_2O_2 addition. Among all tests, co–oxidation at pH 5.3 over 3 hrs with 10 wt% H_2O_2 was determined to be the best precipitation protocol. The precipitate was characterized as poorly crystalline tripuhyite (possessing high specific surface area - 160 – 200 $m^2 \cdot g^{-1}$), thus it was decided to subject it to thermal treatments to increase its crystallinity. Hydrothermal treatment at pH 1 was conducted at 200 °C for 12 hrs; calcination at 950 °C for 12 hrs. Both methods improved the crystallinity and growth of tripuhyite particles with the latter being more effective. A separate highly crystalline tripuhyite sample was synthesized by solid–state reaction at high temperature (950 °C) using reagent grade goethite and antimony pentoxide in order to serve as a reference.

The leachability/stability tests indicated that pseudo–equilibrium was attained by all materials (untreated precipitate, hydrothermal product, calcination product, reference material) in ~ 15 days. Between pH 6 and 8, the untreated precipitate released 100 – 170 $mg \cdot L^{-1}$ Sb, hydrothermally treated precipitate released ~ 0.5 $mg \cdot L^{-1}$ Sb, calcined precipitate released 10 – 35 $mg \cdot L^{-1}$ Sb, and the reference tripuhyite released less than 1 $mg \cdot L^{-1}$ Sb. The results suggested that stability was mainly a function of tripuhyite crystallinity rather than pH (over the 6 – 8 range tested). The hydrothermally treated precipitate demonstrated the highest stability (aside from the synthetic material). The relatively higher Sb release recorded by the calcined precipitate was traced to its contamination with $NaSbO_3$. Lastly, tripuhyite produced via aqueous precipitation and hydrothermal treatment appears to offer a viable option in fixing antimony from metallurgical waste streams and further work to this end is warranted.

Résumé

Le point essentiel de cette thèse est d'étudier la dissolution de l'antimoine (Sb) en solution aqueuse concentrée (6 $g.L^{-1}$) à partir d'antimoniate de fer $FeSbO_4$ (tripuhyite). Ce processus peut jouer un rôle important dans le contrôle des concentrations en antimoine dans les minéraux et les eaux de déchets métallurgiques.

Différentes conditions pH ont été étudiées (pH 1.5 – 5.3) à 95°C et l'élimination du fer(II) et d'antimoine(III) a été étudié grâce à une série de réactions d'oxidation-précipitation par additon de H_2O_2 au goutte-à-goutte. Il n'a cependant pas été possible d'obtenir un précipité hautement cristallin pour tous les tests; c'est pourquoi une procédure à deux étapes a été mise en place. Premièrement, le fer et l'antimoine ont précipités en tripuhyite pauvrement cristallisé au pH optimal de 5.3 (celui produisant un rapport molaire Fe/Sb le plus proche de 1). Dans un second temps, le précipité, une fois lavé, a été traité thermiquement (traitement hydrothermique ou calcination) pour augmenter la cristallinité du minéral. Un minéral synthétique tripuhyite, hautement cristallin, a été également fait grâce à une réaction à l'état solide à haute température (950°C) afin d'évaluer les relatives stabilités des précipités traités et non-traités. Enfin, tous les matériaux (précipité non-traité, produits hydrothermal, produit calciné et minéral synthétique) ont été soumis à des tests de libération/stabilité à des pH proches dans les conditions environnementales (6 – 8) afin de déterminer la libération d'antimoine.

Les tests de libération/stabilité ont indiqué que le pseudo-équilibre a été atteint par tous les matériaux au bout d'environ 15 jours (pour les solutions aux pH contrôlés). Entre les pH 6 et 8 les précipités non-traités ont libéré 100 – 170 $mg \cdot L^{-1}$ Sb, les précipités traités hydrothermiquement ~ 0.5 $mg \cdot L^{-1}$ Sb, les précipités calcinés 10 – 35 $mg \cdot L^{-1}$ Sb et la tripuhyite synthétique de référence moins de 1 $mg \cdot L^{-1}$ Sb. Une comparaison des solubilités des minéraux a également été faite pour chaque pH spécifique. Les résultats montrent que la libération la plus basse de Sb a lieu à partir du produit hydrothermique et de la tripuhyite de référence (pour tous les pH testés) alors le produit calciné libère un ordre de grandeur de plus de Sb et le précipité non-traité deux ordres de grandeur de plus. Les résultats suggèrent que la stabilité du minéral est principalement une fonction de sa cristallinité plutôt que du pH (entre 6 et 8) ; pH auquel le produit hydrothermique a montré la plus grande stabilité (à l'exception du matériau synthétique).

A partir des conditions de test de libération, il apparaît que l'élimination de l'antimoine en solutions aqueuses avec traitement post-précipitation peut générer un matériau semi-cristallin

avec une très faible solubilité, libérant moins de 1 $mg \cdot L^{-1}$ Sb. Cela pourrait donc constituer une option viable pour fixer l'antimoine des eaux de déchets métallurgiques.

Acknowledgements

Throughout the course of this research, I was able to learn from several individuals with various expertise, most of whom have influenced the research presented in this thesis. Firstly, my supervisor, Professor George P. Demopoulos, is sincerely acknowledged for granting me the opportunity to pursue graduate studies, but most importantly for continuously challenging me while providing insight and wisdom. Members of the HydroMet group, a unique mixture of researchers, are recognized for their constant support and assistance: Amrita; Fuqiang; Hsien–Chieh; Huijing; Ivonne; Liying; Marie–Christine; Matthew; Micah; Nathan; Nima; Thomas; Xia; and Zhuoran. I would specifically like to thank Thomas and Zhuoran who have provided great insight, I always thought of Thomas as "Mr. Encyclopedia", which couldn't be more accurate as he was a constant guide during my research, Zhuoran was always a great resource and provided a wealth of information in relation to characterization techniques. I was trained on several analytical equipment (AAS, ICP, and XRD) by Monique Riendeau, Ranjan Roy, Andrew Golsztajn, and Sriraman Rajagopalan, for whom I have the utmost respect as they were always approachable and helpful. McGill staff, Barbara Hanley and Terry Zatylny, are sincerely thanked for putting up with me and my shenanigans. Financial support from the Natural Sciences and Engineering Research Council (NSERC) is greatly acknowledged, this research would not have been possible without it. Lastly, my parents, sisters, and girlfriend Lindsay, are sincerely acknowledged for their constant support and reassured confidence, infinite thanks and love.

Table of Contents

List of figures

Appendix figures

List of tables

Appendix tables

Chapter 1 – Introduction

Antimony (Sb) is an element that is increasingly encountered globally and recognized as a priority pollutant by both the US EPA and EU (Álvarez–Ayuso et al., 2013). The anthropogenic sources of antimony are primarily fossil fuel burning, mining and smelting operations, and waste incineration (Filella et al., 2009). Of these, the deportment and disposal of antimony in mineral and metallurgical operations is of relevance to the present work in terms of its environmental implications.

Typically, antimony is encountered as an undesirable impurity in various mineral feedstocks treated by the gold, copper, and lead extraction sectors. The processing of such feeds results in the mobilization of antimony, reporting to the air pollution control (APC) residues, slags, flue dusts, and process solutions as well as waste waters, all of which are contaminated and must be freed of antimony (Anderson, 2001). Current industrial treatment is limited to internal processing of recycled antimony waste along with wastewater treatment for environmental disposal. The waste sludge entering the tailings disposal site contains significant amounts of antimony, however, there is limited information in the literature on the type and stability of these antimony–carrying compounds, which begs the question whether antimony is truly 'fixed' at these sites.

In many respects, antimony is similar to arsenic, both in chemical properties and toxicity. Arsenic and its various compounds have been extensively studied in terms of removal and disposal into industrial tailings. Currently, the synthetic mineral scorodite, $FeAsO_4 \cdot 2H_2O$, along with a few other select minerals, appear to be promising candidates for fixing arsenic as they have shown to release very little in select pH conditions in laboratory tests (< 1 $mg \cdot L^{-1}$ As at pH 5) (Filippou and Demopoulos, 1997). Unfortunately, antimony's environmental management is still not adequately developed within the metallurgical industry and requires extensive research as to which antimony compounds should be targeted for its safe immobilization in the supergene environment.

Based on assessment of the available literature, only quite recently has research emerged that identifies two Fe(II,III)–Sb(III,V) minerals, namely tripuhyite, $FeSbO_4$ (prominent in oxic conditions), and schafarzikite, $FeSb_2O_4$ (prominent in anoxic conditions), as "two of the ultimate sinks for antimony in the natural environment" (Leverett et al., 2012). Tripuhyite, an analog of scorodite for antimony (bound to ferric iron), appears to fix antimony in the supergene environment, having a solubility of only a few $\mu g \cdot L^{-1}$ Sb (Selim, 2012).

With such promising low antimony solubility, tripuhyite would appear to be an excellent target compound to fix antimony from mineral/metal processing–derived solutions and residues. Historically, tripuhyite has been synthesized via high temperature (800 – 1000 ^{o}C) solid state reactions (Tianshu et al., 1999). Very limited work has been done in terms of precipitation of tripuhyite–like compounds from aqueous solutions that could be applicable to hydrometallurgical solutions. In a recent study, Nag et al. (2012), reported the sonochemical precipitation using ammonia (pH 9 – 10) of a Fe(III)–Sb(III) brownish precipitate that upon subsequent calcination treatment in air yielded crystalline $FeSbO_4$. Such a process is not amenable to large scale industrial implementation. Hence, there is a need for additional work in this area.

The objective of this thesis is indeed to investigate the removal of antimony from acidic aqueous solutions as tripuhyite, $FeSbO_4$, and evaluate it in terms of stability as a potential candidate for the fixation of antimony from mineral and metallurgical processing waste streams. In carrying out this research, the precipitation and evaluation of tripuhyite was studied drawing from our group's experience with the analogous atmospheric scorodite precipitation system (Demopoulos, 2005). In particular, the present study's focus is placed on three main sections; (1) $FeSbO_4$ precipitation and subsequent treatment; (2) material characterization; and (3) tripuhyite precipitate stability under environmentally–relevant pH conditions.

The thesis comprises a comprehensive literature review on antimony and its behaviour in aqueous systems, available in Chapter 2; description of the experimental procedures used in Chapter 3; presentation and discussion of the generated results in Chapter 4; and lastly, global conclusions and recommendations for future studies are presented in Chapter 5. Some supplementary data is provided in an Appendix at the end of the thesis.

Chapter 2 – Literature review

2.1 Introduction

The intent of this literature review is to summarize the environmental behaviour and treatment, some health impacts, and industrial processing of antimony in mineral and metallurgical operations. Focus will be placed on alkaline sulfide processing of antimony–bearing minerals, primarily stibnite and the associated environmental issues and stabilization options.

2.2 Antimony

Antimony, (Sb, atomic number 51), is in Group 15 of the Periodic Table directly below arsenic and has a standard atomic weight of 121.76 $g \cdot mole^{-1}$. Its name is of Greek origin, "anti" plus "monos", translating to "a metal not found alone". This is accurate as native antimony metal is rarely found, usually found as a sulfide mineral, the most important being stibnite, Sb_2S_3 (Lide et al., 2007). Antimony metal is bluish–white in colour, has a fairly low melting point for a metal, 630.6 ^oC, is very brittle and a poor conductor of heat and electricity. Like arsenic, it is typically found in four oxidation states, as –3, 0, +3, and +5.

2.3 Antimony bearing minerals

More than 200 antimony minerals are found in nature. Primary and secondary antimony minerals are listed in Tables 2.1 and 2.2 below, respectively.

Table 2.1 – *Primary antimony minerals, adapted from Anderson (2012).*

Mineral	Stoichiometry	**Mineral**	Stoichiometry	**Mineral**	Stoichiometry
Andorite	$AgPbSb_3S_6$	**Gabrielite**	$Tl_6Ag_3Cu_6(As,Sb)_9S_{21}$	**Stibiconite**	$Sb_2O_4 \cdot H_2O$
Annivite	$Cu_{12}(As,Bi,Sb)_4S_{13}$	**Geocronite**	$Pb_5(As,Sb)_{12}S_8$	**Stibiobismuthine**	$(Bi,Sb)_4S_7$
Aurostibite	$AuSb_2$	**Gerstleyite**	$Na_2(As,Sb)_8S_{13} \cdot 2H_2O$	**Stibiocolumbite**	$Sb(Nb,Ta)O_4$
Berthierite	$FeSb_2S_4$	**Gudmundite**	FeSbS	**Stibiodomeykite**	$Cu_3(As,Sb)$
Boulangerite	$Pb_5Sb_4S_{11}$	**Horsfordite**	Cu_6Sb	**Stibioenargite**	$Cu_3(As,Sb)_4$
Bournonite	$PbCuSbS_3$	**Jamesonite**	$Pb_4FeSb_6S_{14}$	**Stibioluzonite**	$Cu_3(As,Sb)S_4$
Breithauptite	NiSb	**Kermesite**	Sb_2S_2O	**Stibio-tellurobismutite**	$(Bi,Sb)_2Te_3$
Cervantite	Sb_2O_4	**Livingstonite**	$HgSb_4S_7$	**Stibnite**	Sb_2S_3
Cylindrite	$Pb_3Sn_4Sb_2S_{14}$	**Meneghinite**	$Pb_4Sb_2S_7$	**Tetrahedrite**	$Cu_{12}Sb_4S_{13}$
Dyscrasite	Ag_3Sb	**Ramdohrite**	$Ag_2Pb_3Sb_3S_9$	**Ullmannite**	NiSbS
Falkmanite	$Pb_3Sb_2S_6$	**Romeite**	$5CaO_3 \cdot Sb_2O_5$	**Valentinite**	Sb_2O_3
Famatinite	Cu_3SbS_4	**Senarmontite**	Sb_2O_3	**Zinckenite**	$PbSb_2S_4$
Franckeite	$Pb_5Sn_3Sb_2S_{14}$	**Stenhuggarite**	$CaFeSbAs_2O_7$		
Freibergite	$(Cu,Ag)_{12}Sb_4S_{13}$	**Stephanite**	Ag_5SbS_4		

Primary antimony minerals are typically sulfides, mainly because antimony has a stronger affinity for sulfur than oxygen; it is a chalcophile (preference for sulfur). Under ambient pH and temperatures, most primary antimony minerals are fairly stable, little to no dissolved antimony is found in aqueous solutions, as such they are said to be insoluble. However, in oxygen–rich environments, the sulfide and sulfosalt minerals become unstable and react with oxygen to produce secondary minerals, which, depending on the geochemical conditions, can be either stable or unstable and may release antimony (Roper et al., 2012). Table 2.2 includes information on the frequency of occurrence of the specific secondary mineral based on the number of localities it has been found in, from which one may infer their relative stability when antimony fixation options are considered as in present work.

Table 2 2 – *Secondary antimony minerals, adapted from Roper et al. (2012).*

Mineral	Stoichiometry	Frequency of Occurrence
Biehlite	$[(Sb,As)O]_2MoO_4$	1
Bindheimite	$Pb_2Sb_2O_7$	394
Bismutostibiconite	$BiSb_2O_6OH$	6
Bottinoite	$Ni[Sb(OH)_6]_2 \cdot 6H_2O$	14
Brandholzite	$Mg[Sb(OH)_6]_2 \cdot 6H_2O$	4
Braithwaiteite	$NaCu_5(Ti,Sb)_2O_2(AsO_4)[AsO_3(OH)]_2 \cdot 8H_2O$	1
Brizziite	$NaSbO_3$	1
Byströmite	$MgSb_2O_6$	2
Camerolaite	$Cu_4Al_2(HSbO_4,SO_4)CO_3(OH)_{10} \cdot 2H_2O$	10
Cervantite	$Sb^{3+}Sb^{5+}O_4$	227
Cetineite	$(K,Na)_6(Sb_2O_3)_6(SbS_3)_2[(H_2O)_{6-x}(OH)_x](x - 0.5)$	6
Clinocervantite	$Sb^{3+}Sb^{5+}O_4$	2
Coquandite	$Sb_6O_8SO_4 \cdot H_2O$	7
Cualstibite	$Cu_2Al[Sb(OH)_6](OH)_6$	4
Cyanophyllite	$Cu_2Al[Sb(OH)_6](OH)_6$	8
Joëlbruggerite	$Pb_3Zn_3Sb^{5+}As_2O_{13}(OH)$	1
Kelyanite	$Hg_{12}Sb(Cl,Br)_3O_6$	1
Kermesite	Sb_2S_2O	201
Klebelsbergite	$Sb_4O_4SO_4(OH)_2$	15
Mallestigite	$Pb_3Sb(SO_4)(AsO_4)(OH)_6 \cdot 3H_2O$	2
Mammothite	$Pb_6Cu_4AlSbO_2(SO_4)_2Cl_4(OH)_{16}$	7
Mopungite	$NaSb(OH)_6$	6
Nadorite	$PbSbO_2Cl$	14
Onoratoite	$Sb_8O_{11}C_{l2}$	2
Ordóñezite	$ZnSb_2O_6$	2
Ottensite	$(Na,K)_3(Sb_2O_3)_3(SbS_3) \cdot 3H_2O$	1
Partzite	$Cu_2Sb_2(O,OH)_7$	57
Peretaite	$CaSb_4O_4(SO_4)_2(OH)_2 \cdot 2H_2O$	4
Richelsdorfite	$Ca_2Cu_5[Sb(OH)_6](AsO_4)_4Cl \cdot 6H_2O$	43
Roméite	$Ca_2Sb_2O_7$	32

Rosiaite	$PbSb_2O_6$	8
Sabelliite	$Cu_2Zn(AsO_4,SbO_4)(OH)_3$	3
Schafarzikite	$FeSb_2O_4$	11
Sénarmontite	Sb_2O_3	147
Shakhovite	$Hg_4SbO_3(OH)_3$	6
Stetefeldtite	$Ag_2Sb_2(O,OH)_7$	23
Stibiconite	$Sb^{3+}Sb^{5+}{}_2O_6(OH)$	373
Stibioclaudetite	$AsSbO_3$	1
Theisite	$Cu_5Zn_5(AsO_4,SbO_4)_2(OH)_{14}$	45
Thorikosite	$Pb_3(Sb,As)O_3(OH)Cl_2$	4
Tungstibite	Sb_2WO_6	1
Tripuhyite	$FeSbO_4$	48
Valentinite	Sb_2O_3	296
Zincalstibite	$Zn_2Al[Sb(OH)_6](OH)_6$	3

2.4 Applications

Antimony and its various compounds have been known and used since ancient times. There is evidence dating as far back as ancient Egypt, ~ 2000 B.C., to the use of synthetic antimonate compounds used as colorants for glass and as eye shadow, among other things (Shortland, 2002). The various applications continued over the ages, where it was used as material for ornaments, jewellery, and alloys. Antimony compounds also found use in medicine, primarily as hydrated potassium antimonyl tartrate, $K_2Sb_2(C_4H_2O_6)_2 \cdot 3H_2O$, better known as tartar emetic. It was mainly used as an emetic, which induces vomiting, and also as a laxative to purge the human body of illnesses and toxins (Lide et al., 2007).

In today's modern world, antimony compounds find a multitude of applications. They are used as semiconductors for gas sensing applications (liquefied petroleum gas, hydrogen gas, carbon monoxide gas, butane gas, etc.) (Tianshu et al., 1999), infrared detectors, diodes, and much more (Lide et al., 2007). Iron antimonates have been studied for at least thirty years and found to have specific catalytic properties, such as the ammoxidation of propylene (Teller et al., 1985), which may have the potential to replace tin oxide catalysts, SnO_2 type (Tianshu et al., 1999). Inorganic ion exchangers such as iron antimonates have also been found to be selective toward some alkali metals, they are said to be superior than ion–exchange resins due to their thermal stability and differential selectivity (Rawat et al., 1976 & 1984). Although the aforementioned applications seem as though they would account for the bulk of antimony commodities in the market, a large portion of the manufactured antimony compounds actually find their way into

flame retardants, paints, glass, pottery, and as a hardening agent in lead bullets and ammunition (Lide et al., 2007; Anderson, 2012).

2.5 Toxicity to humans and animals

Antimony and arsenic are typically associated together due to their several similarities in chemical behaviour as they both fall in Group 15 of the Periodic Table, even where toxicity is concerned. However, there are some noteworthy differences, the main being the degree of toxicity and the availability of each element in the environment, which play a significant role on its biological and ecological toxicity. Arsenic is likely more toxic than antimony, however, it is also more abundant due to both natural and anthropogenic activities, making it even more likely to be encountered than antimony. Arsenic has been proven to be a definite human carcinogen, as it has been the subject of numerous studies, affecting areas of the skin, lung, bladder, kidney and liver (Gebel, 1997). Antimony, on the other hand, has been much less studied and thus there is limited data on its toxicity as is the study described by Lauwers et al. (1990). Most antimony studies normally include antimony trioxide, Sb_2O_3, as their subject of toxicological tests since it is the most widely used antimony compound. Although the results are slightly skewed to the behaviours of Sb_2O_3 in biological studies, nonetheless, it was found to be a possible human carcinogen (IARC, 1980).

2.6 Antimony in the environment

2.6.1 Air

Antimony and its compounds, usually antimony trioxide, find their way into the atmosphere from several sources and exist as solid compounds suspended in air (Belzile et al., 2011). The many sources of atmospheric pollution can be separated into natural and anthropogenic. The latter, of interest in this work, consists of mining, smelting and refining operations, fossil fuel combustion, and the incineration of waste (Selim, 2012). Natural atmospheric concentration of antimony in urban areas is several $ng \cdot m^{-3}$, and closer to anthropogenic regions this value can increase to hundreds of $ng \cdot m^{-3}$ (Belzile et al., 2011). In China, in anthropogenic vicinities such as mining areas and waste incinerators, the concentration reported as high as 575 $mg \cdot m^{-3}$ (He et al., 2012). Worldwide regulations on the allowable antimony industrial air emissions vary from country to country, however, in Canada and China, the total allowable suspended particulate

emission is 70 and 87 $\mu g \cdot m^{-3}$, respectively, averaged over an annual basis (Canadian Council of Ministers of the Environment, 1999; He et al., 2012).

2.6.2 Soil

Antimony's concentration in the earth's crust is about 0.2 to 0.3 $mg \cdot kg^{-1}$ and is typically found as the sulfide mineral stibnite, sometimes as antimony trioxide. Due to increased antimony–bearing mineral mining and processing over the past few decades, there has been increased deposition of antimony into the environment (Selim, 2012). The anthropogenic sources have been outlined above and contribute to a significant portion of the pollution. Soil concentrations close to these sources can reach values of 15,000 $mg \cdot kg^{-1}$and even 80,000 $mg \cdot kg^{-1}$, as were the cases in southern Tuscany and a smelter site in New Zealand, respectively (Wilson, 2004; Selim, 2012). Table 2.3 gives examples of increased Sb contamination levels in soils surrounding anthropogenic sites such as mining, smelting and shooting range sites. One anthropogenic source worth mentioning is lead–antimony alloy bullets, which are the largest contributors of antimony in the soils of shooting ranges. Industrial regulations on environmental solid waste releases are not widely adopted. Typically the waste is transferred to settling or tailings areas and subjected to wastewater treatment for release. The maximum allowable concentration into agricultural soils is 10 $mg \cdot kg^{-1}$ for antimony, which is more stringent than arsenic (15 – 20 $mg \cdot kg^{-1}$) (Kabata–Pendias, 2011).

Table 2.3 – *Antimony concentration in contaminated soils from anthropogenic activities, adapted from Wilson et al. (2004).*

Soil Sb concentration range ($mg \cdot kg^{-1}$)	Contamination Source	Comments
80,200	Smelter site	From one sample classified as soil
2.5 – 175	Urban soils impacted by lead zinc smelter	0 – 25 cm surface soils
0 – 1,090	Area surrounding a goal–antimony mine	A horizon samples up to 7.5 km from tailing dam (in prevailing wind direction)
11.9 – 710	Previous mining activities	Low levels of water–soluble Sb
27.7 – 15,100	Previous mining activities	Shoots and leaf accumulation for 3 species of up to 1,160 and 1,370 $mg \cdot kg^{-1}$
2.5 – 237	Previous mining activities	Soils classified as highly contaminated
31 – 5,986	Abandoned mine area	B horizon soils, Portugal
0.1 – 39.4	Antimony mine 300 km upstream	Floodplain in NSW Australia, moderately contaminated with Sb
180 – 554	Antimony mine area approx. 2 km upstream	Rhizosphere soil adjacent to contaminated creek, NSW
7.4 – 13,610	Previous mining activities	A horizon soils

26 – 1,150	Mining contaminated area, S. France	Surface soils
35 – 17,500	Shooting range, Switzerland	< 0.5 mm soil fraction. High concentrations associated with Sb in bullets
1,300 – 17,500	Shooting range	0 – 0.45 cm depth
629 – 8,230	Shooting range	0.2 – 10 cm depth Rhizosphere soil

2.6.3 Water

Worldwide antimony concentration in unpolluted natural waters is commonly well below 1 $\mu g \cdot L^{-1}$. Most naturally occurring antimony in fresh waters is from rock weathering and soil runoffs (Filella et al. 2002a). One of few exceptions to low concentrations in natural waters are hot springs where the concentrations can sometimes exceed 500 $mg \cdot L^{-1}$, although the likelihood of encountering this situation is low. In oceans, the concentration is even less than fresh waters, estimated to be 200 $ng \cdot L^{-1}$ (Filella et al. 2002a). Anthropogenic sites and their vicinities typically have concentrations of one to two orders of magnitudes higher than natural waters, in China, this was found to be as high as 263 $\mu g \cdot L^{-1}$ in certain mine natural waters. Many regulatory bodies worldwide place strict limits on antimony content in drinking water as it has been labelled a hazardous substance. The World Health Organization, China, USEPA and European Union drinking water standards are set to 20 $\mu g \cdot L^{-1}$, 5 $\mu g \cdot L^{-1}$, 6 $\mu g \cdot L^{-1}$and 5 $\mu g \cdot L^{-1}$, respectively (Council of the European Union 1998; USEPA 1999; WHO 2006; He et al. 2012). Industrial environmental release regulation varies or is not specific for antimony and its compounds, however, sometimes arsenic limits are associated to antimony due to their similarities, which is 0.5 $mg \cdot L^{-1}$ (monthly average) and 1.0 $mg \cdot L^{-1}$ (for a grab sample) from the Canadian Metal Mining Effluent Regulation (Government of Canada 2014).

2.6.4 Treatment

Particulate and toxic substance releases such as antimony oxides are normally captured and subjected to subsequent treatment. They are collected in flues, condensing pipes, baghouses, and electrostatic precipitators (Anderson, 2012). Waste incineration is a prime example where municipal waste along with some landfill waste is burned, 20% of which becomes bottom ash and 2 – 3% results in air pollution control residue (APC). Elemental antimony being fairly volatile at temperatures > 500 ^{o}C, only about half reports to the bottom ash, while the other half reports to the APC residue, which contains many other toxic substances and must be further processed before moving onto landfill (Cornelis et al., 2008; Okkenhaug et al., 2013). Since the APC residue is very alkaline, the choice of treatment is neutralization with other industrial wastes containing sulfuric

acid and iron, to yield a final pH between 8 and 9. Iron compounds such iron hydroxides and iron oxyhydroxides precipitate out of solution due to neutralization and many metals either adsorb or co–precipitate with these compounds. The precipitate moves onto landfills, while the neutralized solution, which still contains trace metals, moves onto wastewater treatment for final processing (Okkenhaug et al., 2013). Pyrometallurgical processing of antimony results in antimony residues containing significant amounts of precious and base metals that must be recovered before recycling the antimony into the feed. This residue can be treated a number of ways, however, a very selective method for antimony and gold is alkaline sulfide leaching. An example of the conditions yielding more than 99% of antimony removal is outlined by Anderson (2001) where the pyrometallurgical antimony oxide residue was subjected to 6 hrs of leaching, at 105 ^{o}C, sulfide and free hydroxide concentrations of 100 and 25 $g \cdot L^{-1}$, respectively.

There are extensive soil remediation methods to treat highly polluted soils, these include leaching, soil amendment (immobilization), biodegradation (microbial degradation of substances), phytoremediation (removal of metals by plant uptake), vitrification (immobilization via melting into a glass–like solid), encapsulation, excavation (removed and placed in landfill), and isolation (placing subsurface barriers such as clay or plastic liners) (Kabata–Pendias, 2011). A fairly common method appears to be soil amendment since the processing can take place onsite and is relatively low cost. This is also the choice of treatment for antimony immobilization in many sites such as naturally polluted soils, industrial, and shooting range soils. Many materials have been tested over the past several years, as noted by Álvarez–Ayuso et al. (2013) which include phosphate and sulfur–based amendments, sodium humate, drinking water de–ironing sludge, calcium hydroxide, greenwaste compost mulch, Portland cement, wood bark, and phosphate fertilizers. Of these, sulfur–based amendments, drinking water de–iron sludge, calcium hydroxide, and Portland cement have proven to be effective. However, there is a lack of implementation of effective methods to treating mining derived wastes. From research, there are numerous metal oxides and oxyhydroxides such as iron and manganese oxyhydroxide that have demonstrated high extraction of antimony from soils, however, large–scale execution has yet to be established (Kabata–Pendias, 2011; Álvarez–Ayuso et al., 2013).

Antimony removal from industrial effluents (aqueous) is normally performed at wastewater treatment plants. A variety of methods are encompassed in treatment plants such as adsorption, membrane separation, and aluminum/iron based coagulation–flocculation–sedimentation (Gannon

et al., 1986; Wu et al., 2010). Treatment of antimony aqueous waste streams may be similar to arsenic, which has been studied extensively (Guo et al., 2009).

2.7 Industrial processing and treatment

2.7.1 Antimony metallurgy

Worldwide antimony production statistics and ore body reserves are summarized in Table 2.4, with China being the main producer, accounting for about 80% of total production (U.S. Geological Survey, 2014).

Table 2.4 – *Worldwide antimony production and ore body reserves from 2012 and 2013, U.S. Geological Survey (2014).*

Country	Mine Production (metric tons)		Ore Reserves (metric tons)
	2012	2013	
United States	--	--	--
Bolivia	4,000	5,000	310,000
China	145,000	130,000	950,000
Russia	6,500	6,500	350,000
South Africa	3,800	4,200	27,000
Tajikistan	2,000	4,700	50,000
Other Countries	13,000	13,000	150,000
World Total (rounded)	174,000	163,000	1,800,000

Antimony minerals are processed many different ways and the proper method is chosen based on several factors, i.e. grade and type of antimony mineral in ore feed, presence of other metals, type of final product and product quality. The processing of antimony, like most other minerals, can be broken into three sub–industries; mineral processing, pyrometallurgy, and hydrometallurgy. Mineral processing and pyrometallurgy of antimony minerals will be discussed in brief and hydrometallurgy will be discussed in detail since this process is at the heart of the research objective. Primary focus will be placed on alkaline sulfide leaching of stibnite from base metal and gold industries due to the overwhelming number of plants operating under such conditions as opposed to acidic chloride leaching (Anderson, 2012).

2.7.2 Mineral processing

Like most mineral processing, antimony ore processing consists of ore crushing, grinding, classification (gravity separation and cyclones) and flotation. The feed ore typically contains stibnite along with other gangue minerals. In China, it is pyrite, quartz, calcite, barite, kaolin, and

gypsum. The feed grade is usually between 2–3% antimony, and treated through hand sorting, spiral concentration, and flotation (Anderson, 2012).

2.7.3 Pyrometallurgy

There are different pyrometallurgical methods available to process antimony–bearing ores, however, the ore/concentrate grade of antimony dictates the most suitable method. As outlined by Anderson (2012), 5–25% antimony feedstocks are volatized by roasting at ~ 1000 ^{o}C; this treatment removes sulfur as SO_2 off–gas and antimony trioxide, Sb_2O_3, is retrieved as flue dust. Feedstocks with grades in the range of 25–40% are subjected to smelting in a blast furnace at 1300–1400 ^{o}C to yield pure antimony metal. Lastly, antimony raw materials, like antimony sulphide–Sb_2S_3 containing 45–60% Sb, are liquefied by heating at 550–600 ^{o}C and the liquefied product then is reduced to pure antimony metal.

2.7.4 Hydrometallurgy

Many simple and complex antimony sulfide minerals can be processed through hydrometallugical techniques, for both antimony and other valuable metal production. Usually, the main objective of the process is to recover a desired metal associated with the antimony mineral, primarily gold, however, other metals are typically present. The most effective and widely used method is known as alkaline sulfide leaching, it's very selective for antimony, gold, arsenic, mercury, and tin minerals. Another method is acidic chloride leaching, however, it is much less preferred due to chemical complexity and corrosion issues (Anderson, 2012).

In alkaline sulfide leaching, the lixiviant used to leach antimony and gold is usually a mixture of sodium sulfide and sodium hydroxide. The sodium hydroxide is used to ensure alkalinity and to prevent the hydrolysis of sodium sulfide and toxic hydrogen sulfide gas generation. These undesired reactions are summarized in Equations (1) and (2):

$$Na_2S + H_2O \rightarrow NaHS + NaOH \quad (1)$$

$$NaHS + H_2O \rightarrow H_2S + NaOH \quad (2)$$

The presence of sodium hydroxide, i.e. external reagent addition, largely prevents the completion of reaction (1) and (2) (Ubaldini et al., 2000). During the leaching stage, stibnite reacts with sodium sulfide to form sodium thioantimonite, Na_3SbS_3, demonstrated in Equations (3) and (4):

$$Na_2S + Sb_2S_3 \rightarrow 2NaSbS_{2\,(aq)} \quad (3)$$

$$NaSbS_{2\,(aq)} + Na_2S \rightarrow Na_3SbS_{3\,(aq)} \quad (4)$$

Dissolution of elemental sulfur in sodium hydroxide is used as a lixiviant as well. The chemistry can be more complex than the above reactions involving several sulphur and Sb(V) species like sulfide, S^{2-}, polysufide, S_x^{2-}, and thiosulfate, $S_2O_3^{2-}$ and Na_3SbS_4 (Jeffrey and Anderson, 2003).

The antimony–bearing solution is then passed to the electrowinning stage where solid antimony metal is plated at the cathode; Equations (5), (6), and (7) display the primary cathode and anode reactions (Anderson, 2012):

CATHODE: $$SbS_3^{3-} + 3e^- \rightarrow Sb^o + 3S^{2-} \quad (5)$$

ANODE: $$4OH^- \rightarrow 4e^- + H_2O + O_2 \quad (6)$$

ANODE: $$S^{2-} \rightarrow 2e^- + S^o \quad (7)$$

If other desirable metals are present in the stibnite ore such as gold, copper or silver, e.g. the mineral freibergite, $(Cu,Ag)_{12}Sb_4S_{13}$, the lixiviant described above is still very effective (Awe et al., 2013). For gold, the following reactions take place (Jeffrey and Anderson, 2003):

$$Au^o \rightarrow Au^+ + e^- \quad (8)$$

$$Au^+ + S^{2-} \rightarrow AuS^- \quad (9)$$

$$Au^+ + 2S_2O_3^{2-} \rightarrow Au(S_2O_3)_2^{2-} \quad (10)$$

Equations (8) to (10) describe gold dissolution in alkaline sulfide media as opposed to the traditional cyanidation of gold, which, in recent years has been challenged due its toxicity.

2.7.5 Treatment and antimony recovery

Remediation efforts have increased over the years to recover antimony from a variety of sources, primarily from intermediate smelter products such as slags, drosses, flue dusts, and residues from copper and lead smelters (Anderson, 2001). More specifically, these include lead–smelter speiss (containing precious metals), lead–softening skims (common in lead refining), lead–smelter copper dross flue dust (common in lead processing), and pyrometallurgical plant antimony oxide residue (collected at the electrostatic precipitator), most of which can be treated by alkaline sulfide leaching. Due to the very high selectivity of alkaline sulfide leaching, at least 90% antimony recovery is common (Anderson and Twidwell, 2008). Other secondary sources of antimony include recycled batteries, processed in a blast furnace to make lead bullion, and spent antimony catalysts from the petrochemical industry.

2.8 Antimony speciation

2.8.1 The Sb–H_2O system

Antimony can exist in four oxidation states, –3, 0, +3, and +5, however, in aqueous solutions, the predominant species exist in the +3 and +5 oxidation states, Sb(III) and Sb(V). Computer simulations of the relative abundance of both Sb(III) and Sb(V) species in oxic and anoxic waters, based on the best thermodynamic data currently available, showed that $Sb(OH)_6^-$ is exclusively present in oxic waters, whereas, $Sb(OH)_3^0$ is exclusively present in anoxic waters (Filella and May, 2003). In reality, several sources have reported the presence of both Sb(III) and Sb(V) in both oxic and anoxic waters, which contradicts the thermodynamic calculated data (Andreae and Froelich, 1984; Filella et al., 2009). Some researchers have attributed this to the result of biological activity, however, others have indicated the more likely causes, slow oxidation kinetics between Sb(III) and oxygen in oxic waters and Sb(III) oxidation to Sb(V) perhaps by polysulfide species (Quentel and Filella, 2002; Helz et al., 2002; Leuz and Johnson, 2005). Thermodynamic data for Sb(III) and Sb(V) is limited in literature, as compared to more common systems. According to the calculated Pourbaix diagram (Figure 2.1)[1], the hydrolytic Sb(V) species, $Sb(OH)_6^-$, is dominant at pH values greater than ~ 2.5 under oxic conditions. At reasonably reducing conditions, the dominant hydrolytic Sb(III) species is $Sb(OH)_2^+$, at pH values less than ~ 2, $Sb(OH)_3^0$, at pH values between ~ 2 and 12, and $Sb(OH)_4^-$, at pH values higher than ~ 12 (Krupka and Serne, 2002). For very dilute systems such as the one depicted in Figure 2.1, < 0.001M Sb, the dominant species are said to be independent of antimony concentrations. However, where more concentrated solutions are concerned, > 0.001M Sb, Sb(V) may form polynuclear species under acidic conditions (pH < 7) and Sb(III) is insignificantly affected at concentrations lower than 0.1 M Sb (Krupka and Serne, 2002). The polynuclear species are $Sb_{12}(OH)_{64}^{4-}$, $Sb_{12}(OH)_{65}^{5-}$, $Sb_{12}(OH)_{66}^{6-}$, and $Sb_{12}(OH)_{67}^{7-}$ (Accornero et al., 2008). Some stability diagrams for aqueous antimony species are presented as follows, although, it must noted that the data relates to very dilute solutions and direct application to concentrated solutions used later in this work can be only partly relevant.

[1] Calculated with MEDUSA (32 bit version – December 16, 2010).

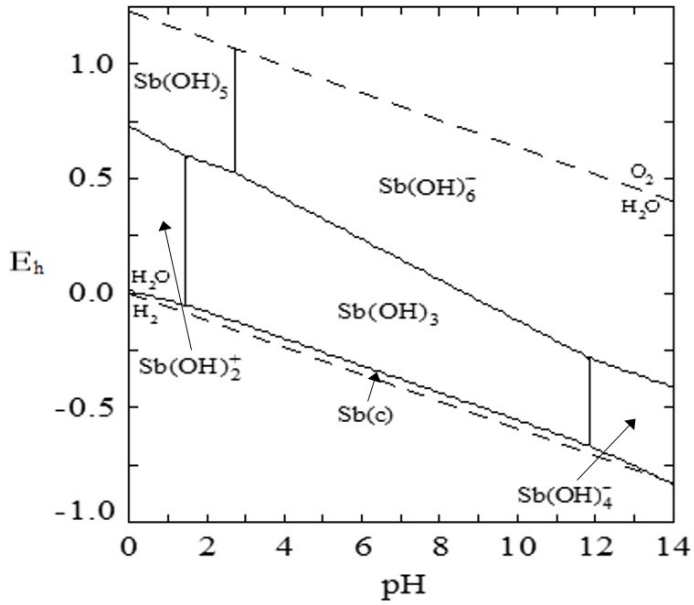

Figure 2.1 – *E_h–pH diagram for dilute aqueous antimony solutions, calculated at 25 °C, 10^{-10} mol·L^{-1} Sb.*

Figure 2.2[2] displays the change in the E_h–pH diagram of Figure 2.1 when antimony concentrations are increased to 10^{-7} and 10^{-5} mol·L^{-1}, resulting in solid species (Sb_2O_3 and Sb_2O_4). The solubility of the solid species was obtained from limited thermodynamic data and the results are qualitative at most, as also stated by Krupka and Serne (2002).

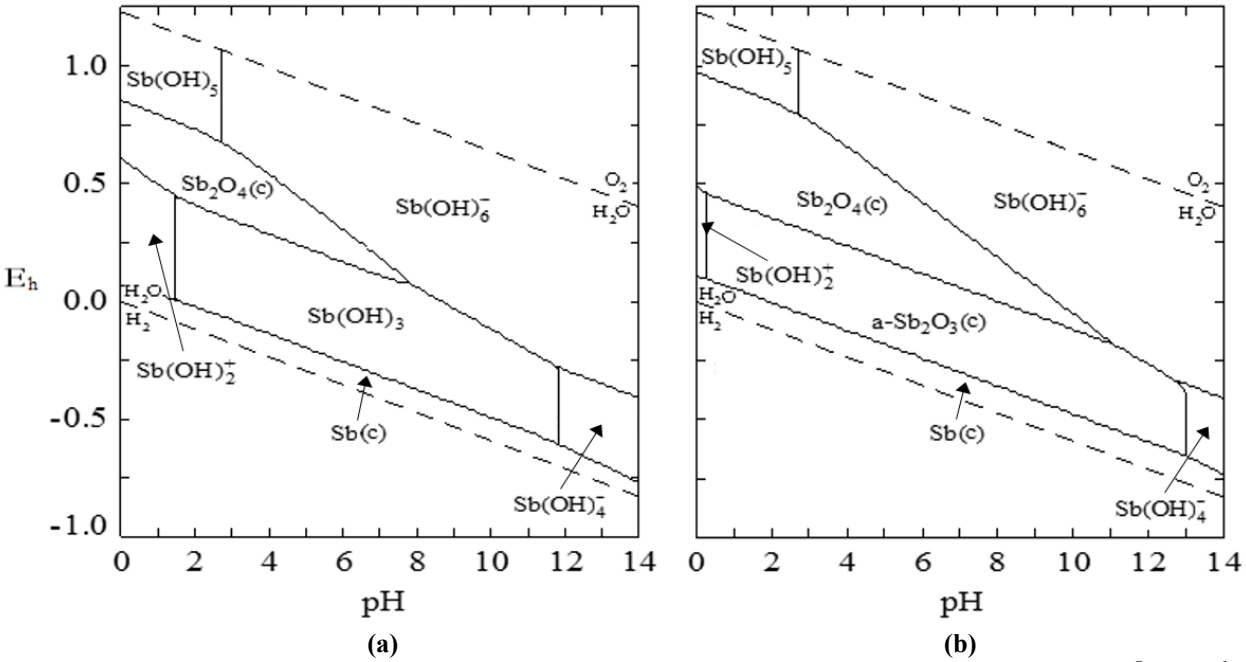

Figure 2.2 – *E_h–pH diagram for concentrated aqueous antimony solutions, calculated at 25 °C: (a) 10^{-7} mol·L^{-1} Sb, (b) 10^{-5} mol·L^{-1} Sb.*

[2] Calculated with MEDUSA (32 bit version – December 16, 2010).

Figure 2.3 displays the speciation of Sb(III) and Sb(V) as a function of pH in anoxic and oxic conditions, respectively, for dilute aqueous solutions (Tella and Porkovski, 2012).

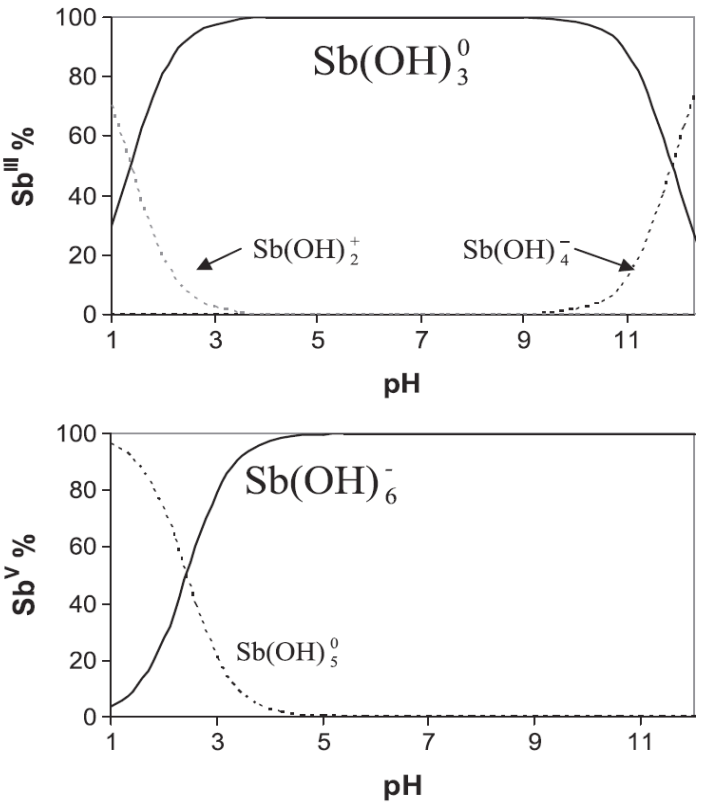

Figure 2.3 – *Speciation diagram for Sb(III) and Sb(V) in aqueous solutions as a function of pH, at 25 °C and 1 bar, reproduced from Tella and Porkovski (2012).*

Figure 2.4 displays the change in speciation of an Sb(III) aqueous system, studied over a large temperature range (25 – 300 °C) by Zakaznova–Herzog and Porkovski (2006). It can be seen that in the acidic region, there is a small change in speciation (relatively unchanged when comparing 25 °C and 300 °C). On the other hand, there is a significant decrease in the relative speciation of $Sb(OH)_3^0$, demonstrating decreased stability at higher temperatures.

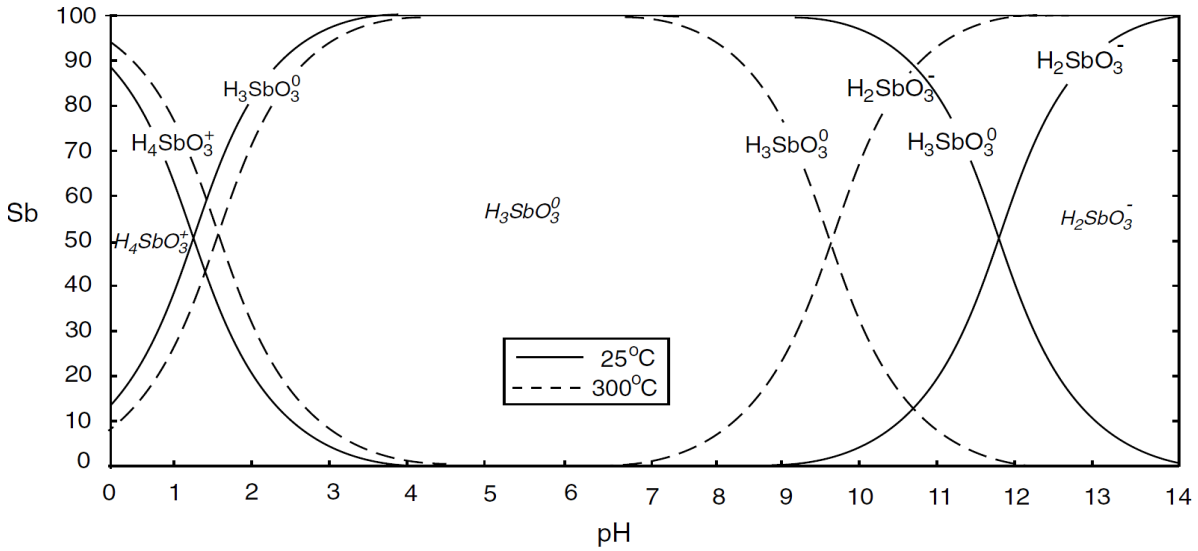

Figure 2.4 – *Comparison of speciation of Sb(III) at 25 °C and 300 °C, 0.0001 mol·L^{-1} Sb, reproduced from Zakaznova–Herzog and Seward (2006).*

2.8.2 The Sb–S–H_2O system

Due to the relevance of antimony in hydrothermal sulfidic solutions, acidic and especially alkaline, many studies have been carried out to understand the complex speciation of the Sb–S–H_2O system. The results are quite varied and Filella et al. (2002b) have suggested discrepancies may arise from variation of concentrations of reagents (Na_2S in particular) and the crystallinity of stibnite, Sb_2S_3. Filella and May (2003) have compiled the best available thermodynamic data on the antimony–sulfur system (stability constant data is summarized in Table A.2 in the Appendix). Relevant speciation diagrams at different pH values of sulfide–rich freshwaters are plotted in Figure 2.5. Both antimony sulfide and hydroxide species, predominantly SbS_4^{3-} and $Sb(OH)_6^-$ are seen to be present, the relative abundance of which depends on the redox character of the solution.

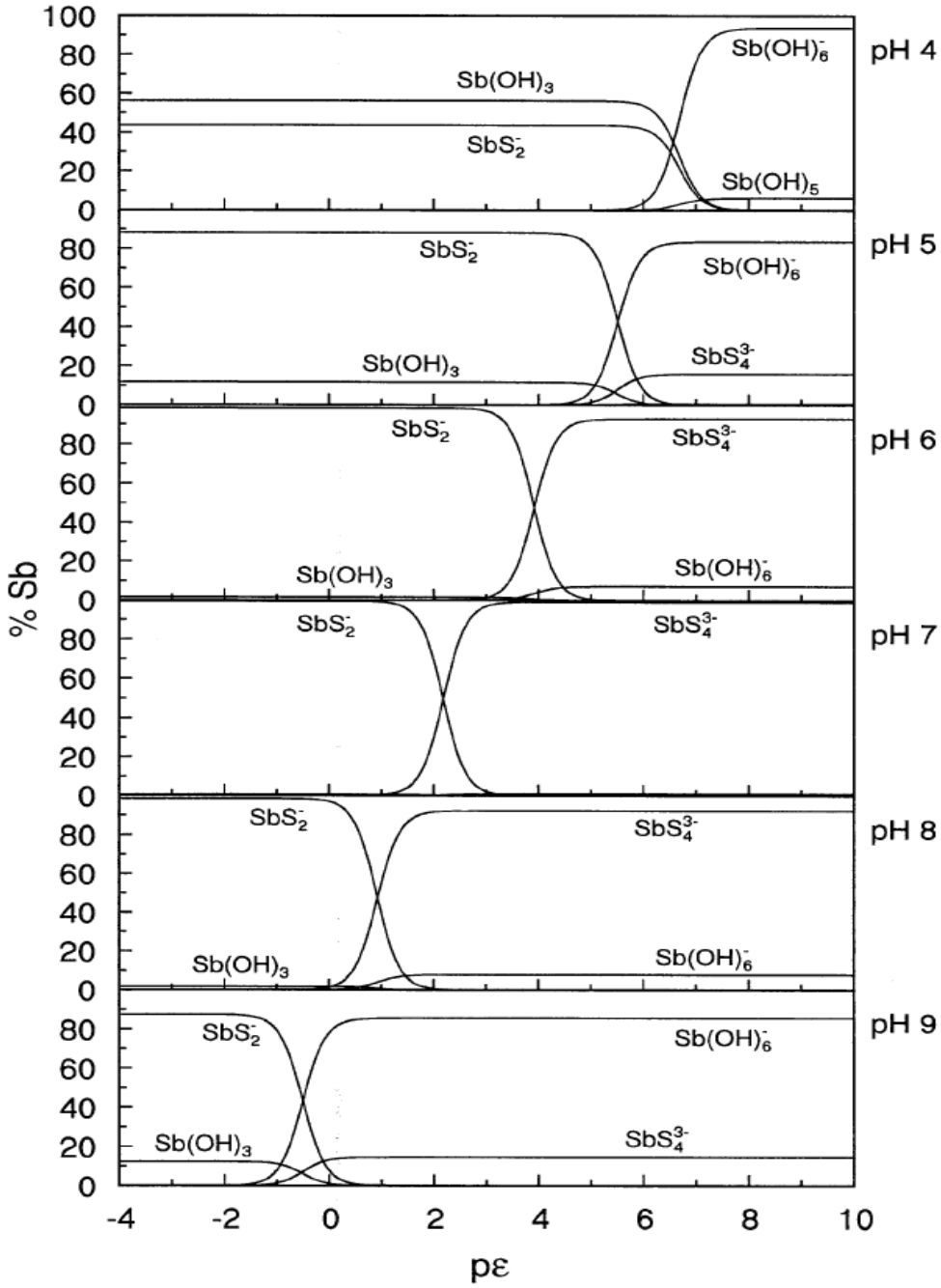

Figure 2.5 – *Antimony–sulfide system speciation as a function of redox conditions at different pH values. Concentrations: 1.10^{-9} mol·L^{-1} Sb, 1.10^{-6} mol·L^{-1} S, to resemble natural freshwater and sediment systems. The pε refers to the activity of the electron (pε = – log[e^{-}]), analogous to the redox potential E_h, the positive and negative values refer to oxidizing and reducing conditions, respectively. Note: this system assumes the system is in a 'quasi–equilibrium' where the oxidation of sulfide is kinetically precluded, reproduced from Filella and May (2003).*

Antimony–sulfide speciation has been researched at different antimony concentrations and temperatures. Sherman et al. (2000) studied the complexation of Sb(V) in alkaline sulfide solutions between 25 and 300 ºC, and stated that the dominant species was $Sb(HS)_4^+$ for all three

solutions under 150 °C, while higher temperatures yielded mixed–ligand species $Sb(HS)_{4-n}(OH)_n^+$, which further polymerize past 250 °C. The three solutions were: (1) *0.1M Sb + 1.15M Na_2S*; (2) *0.05M Sb + 0.2M NaHS + 0.06M NaOH*; (3) *0.05M Sb + 0.2M NaHS + 1M NaCl + 0.06M NaOH*. The study incorporated the use of X–ray absorption fine structure spectra (EXAFS) to determine Sb(V) speciation in solution, which could not distinguish between unprotonated SbS_4^{3-} and fully protonated $Sb(HS)_4^+$, Sherman et al. chose $Sb(HS)_4^+$ as the more likely species based on the higher presence of HS^- in the system. In another study, conducted by Mosselmans et al. (2000) EXAFS analysis was performed on a variety of antimony concentrated solutions and temperatures, ranging from 1–100 mM Sb, 0.009 – 2.5 M HS–, and –193–200 °C. Many of the solutions contained species of antimony bonded to four sulfur atoms, thus consistent with the SbS_4^{3-} species, supporting the results of Sherman et al. (2000) and Filella and May (2003) (depicted in Figure 2.5).

2.9 Antimony oxidation – Sb(III) to Sb(V)

Over the past decade, the oxidation (with different oxidants) of antimony in aqueous solutions has received much interest in particular in relation to its adsorption on iron and manganese hydroxides and oxyhydroxides, however this is not the focus of the present study (Belzile et al., 2001; Leuz et al., 2006b). Some of the information that is of relevance has been summarized.

2.9.1 Oxygen (O_2)

Leuz and Johnson (2005) studied the oxidation kinetics of Sb(III) via atmospheric oxygen at 25 °C and concluded that there was no significant oxidation between the pH range 3.6 to 9.8, even after 200 days. In the pH range of 10.9 to 12.9, they reported significant oxidation within 4 to 420 days, more so at pH 12.9. They attribute the relative increase in oxidation at higher pH to a more thermodynamically favourable transformation of Sb(III) species, more favourable to change from $Sb(OH)_4^-$ to $Sb(OH)_6^-$ (+45.8 kJ/mol) than $Sb(OH)_3^0$ to $Sb(OH)_6^-$ (+110.6 kJ/mol). At higher pH, the presence of $Sb(OH)_4^-$ is increased (Figure 2.3), especially past pH 12. Further, there is evidence that the oxidation kinetics can be increased due to hydrolysis, as noted by other researchers for cases of Fe(II) and Mn(II) oxidation, where the oxidation of the hydrolyzed antimony species ($Sb(OH)_4^-$) was observed by Leuz and Johnson (2005) to be faster than the non–hydrolyzed ($Sb(OH)_3^0$).

2.9.2 Hydrogen peroxide (H_2O_2)

Hydrogen peroxide is a stronger oxidizing agent than oxygen and is present in surface waters between 10^{-8} and 10^{-6} M, which is why it is also considered in oxidation kinetic studies of natural waters (Leuz et al., 2005). Only in the past decade has the influence of H_2O_2 on the oxidation kinetics been studied with effective results. Leuz and Johnson (2005) and Quentel et al. (2004) both studied the oxidation kinetics of Sb(III) by hydrogen peroxide and, as expected, determined it was much faster. The former researchers determined the reaction kinetics of Sb(III) to be independent of pH after ~ 11.7, below this, it is first order dependent on pH, as shown in Table 2.5, which displays the predicted half–lives of Sb(III) oxidation by H_2O_2 at different basic pH values for the rate law:

$$-\frac{\mathrm{d[Sb(III)]_{tot}}}{\mathrm{dt}} = k \cdot [\mathrm{Sb(III)}]_{\mathrm{tot}} \cdot [\mathrm{H_2O_2}]_{\mathrm{tot}} \quad \text{(k dependent on pH below 11.7)} \qquad (1)$$

This pH dependence of oxidation was also validated by Quentel et al. (2004) in the pH range of 8 to 9.7 and stated that there was no detection of oxidation below pH 7, where the existence of $Sb(OH)_3^0$ prevailed. Quentel et al. (2004) proposed the identical rate law for alkaline solutions, however, also elaborated on its ionic strength and temperature dependence, where an increase in both variables demonstrated linear increase in the oxidation rate:

$$-\frac{\mathrm{d[Sb(III)]_{tot}}}{\mathrm{dt}} = k \cdot [\mathrm{Sb(III)}]_{\mathrm{tot}} \cdot [\mathrm{H_2O_2}]_{\mathrm{tot}} \qquad (2)$$

Where, $\log \mathrm{k} = 1.26 + 1.01\sqrt{\mathrm{I}} - 0.22\mathrm{I} - 2603/\mathrm{T}$

Table 2.5 – *Estimated half–lives for the oxidation of Sb(III) with H_2O_2 at different surface water pH values with ionic strength = 0.01M, reproduced from Leuz and Johnson (2005).*

	pH 7	**pH 8**	**pH 9**
k [M^{-1} s^{-1}]	6.8 x 10^{-3}	6.8 x 10^{-2}	6.8 x 10^{-1}
$t_{1/2}$ [yr] with 10^{-8} M H_2O_2	324.2	32.4	3.2
$t_{1/2}$ [yr] with 10^{-6} M H_2O_2	3.2	0.32	0.03

2.9.3 Trace metal effects

Due to the presence of trace metals in many aqueous solutions containing antimony, especially seawaters, their effects on Sb(III) oxidation by hydrogen peroxide has been the focus of a few studies. The trace metals Cu(II), Mn(II), Zn(II), and Pb(II) were studied by Elleouet et al.

(2005), while Fe(II) and (III) effects were investigated by Leuz et al. (2006a). Elleouet et al. (2005) concluded that the oxidation kinetics in the presence of most of the observed trace metals did indeed increase in the natural water pH range and concentrations. Zinc(II) had not effect at all, whereas Cu(II), Mn(II), and Pb(II) did. Copper(II) demonstrated significant oxidation acceleration kinetics whereas the remaining two were not as pronounced. Leuz et al. (2006a) demonstrated the effectiveness of iron–assisted oxidation, where within the acidic pH range the co–oxidation with Sb(III) was similar for both Fe(II) and (III). However, in the alkaline region, only Fe(II) co–oxidation was effective in accelerating oxidation kinetics. Relevant results from this study are summarized as follows:

Sb(III) oxidation in the presence of Fe(III) and Fe(II)

Since Fe(III) is produced during Fe(II)–facilitated oxidation of Sb(III), its influence on the oxidation kinetics was also studied with Fe(II). Leuz et al. (2006a) found that in acidic solutions, pH 2.2 to 3.2, with Fe:Sb of ~ 90, Fe(III) oxidized Sb(III) with pseudo–first order rate coefficients, which was essentially similar to the reactions with Fe(II). The total oxidation time may be estimated to ~ 1.5 years, with 1 μM Sb(III), 90 μM Fe, and at 25 ^{o}C. In the mildly acidic region, pH 5 and 6.2, no Sb(V) formed via Fe(III) oxidation, however, the total antimony concentration was found to decrease, which was likely the result of Sb(III) sorption onto iron hydroxide colloids. Further, with Fe(II) in the same pH range, total oxidation of antimony (1 μM) occurred within 7 days (pH 5) and 10 hrs (pH 6.2), thus it was concluded that Fe(III) oxidation was insignificant above pH of 5. At pH 7.2, total oxidation with Fe(II) occurred within 10 mins.

Sb(III) oxidation in the presence of Fe(II) and O_2

Subsequent experiments were performed on Sb(III) oxidation with Fe(II) and O_2 (1 μM Sb(III), 90 μM Fe(II)), studied between pH 2.2 and 7.6. The results greatly resembled the trend of Fe(II) oxidation via oxygen, which has been known to be strongly pH dependent. The results demonstrated that slow oxidation occurred between 2.2 and 3.6, while it was faster between 6.2 and 7.1. Ratios of iron to antimony were then varied in the neutral pH range, between 6.4 and 7.5, the results showed that higher ratios with higher pH yielded faster oxidation kinetics (much better with Fe:Sb > 3:1 at pH 7.5).

Sb(III) oxidation in the presence of Fe(II) and H_2O_2

Oxidation of Sb(III) in the presence of both Fe(II) and H_2O_2 was found to be extremely fast, more than 95% oxidation occurred within 20 seconds at pH 6.8 while it required 1 hr at pH 2.9 (Figure 2.6). Thus, with increasing pH, the dramatic increase in the oxidation rate was evident. Lastly, the oxidation effect of the iron to antimony ratio in the solution was also investigated in the alkaline pH range, therefore different ratios, Fe:Sb = 1:100, 1:10, 1:1, 3:1, were also tested (Figure 2.6(D)). It was found that even trace amounts of Fe(II), Fe:Sb = 0.01, can catalyze the oxidation of significant amounts Sb(III), up to ~ 45%, in presence of 3 μM H_2O_2. Ratios above 0.1 were found to result in the complete oxidation of Sb(III).

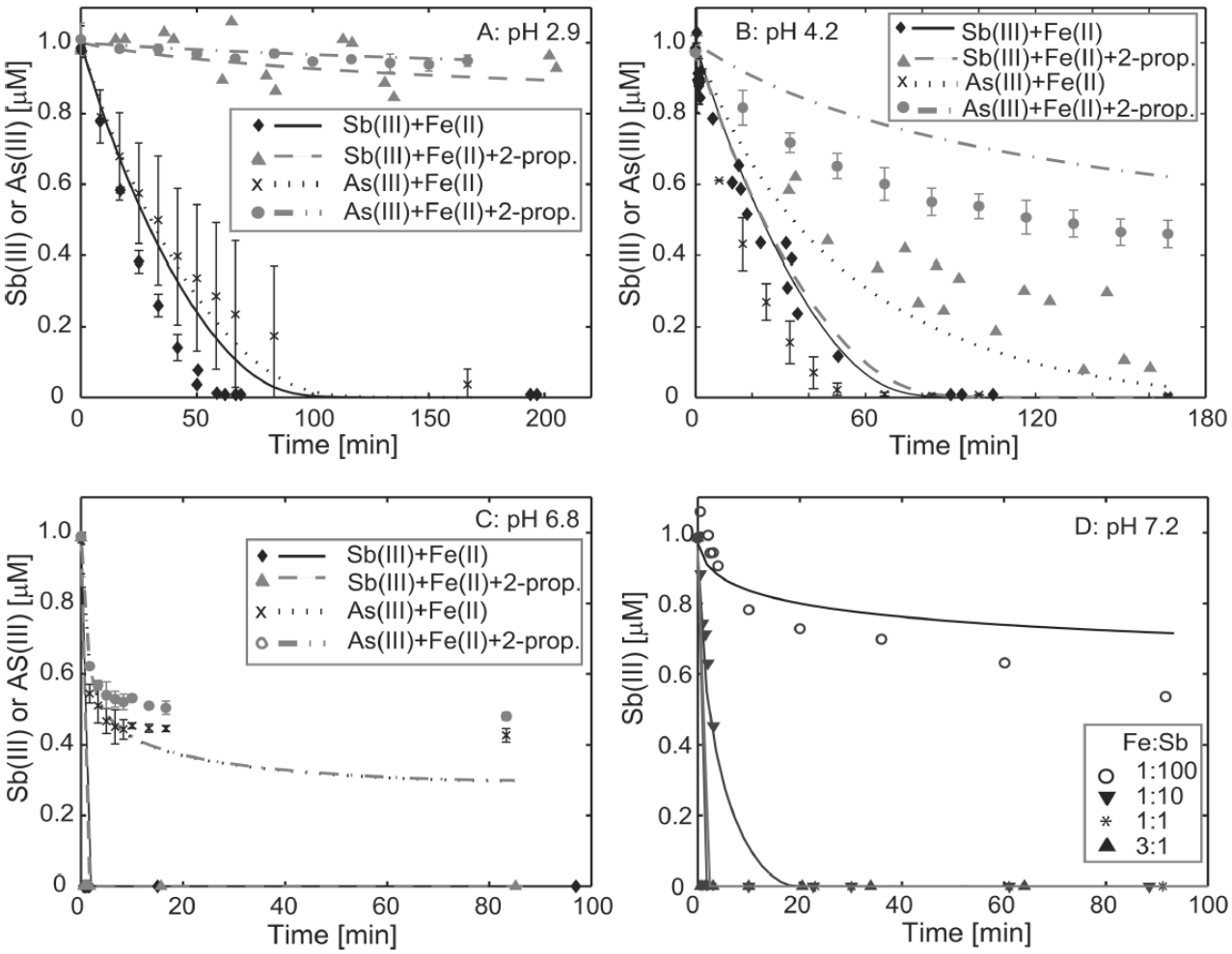

Figure 2.6 – *(A) – (C): pH dependence of 1μM Sb(III) and 1μM As(III) oxidation in the presence of 3μM Fe(II) and 3μM H_2O_2 in aerated solutions. Lines represent linear fits based on hypothetical reaction models. (D): Sb(III) concentrations as a function of time with different initial Fe(II) concentrations, with 1μM Sb(III) and 3μM H_2O_2, reproduced from Leuz et al. (2006a).*

2.10 Ultimate sinks of antimony in the environment

In Tables 2.1 and 2.2 presented in the first part of this chapter the various primary and secondary antimony minerals along with their respective occurrences were summarized. Of interest to the present work is to identify the ones that can serve as model compounds for fixing antimony mobilized as result of mineral processing activities. In the past the stability of several of these minerals has been questioned due to possible contamination by less stable compounds as is the case of antimony pentoxide, Sb_2O_5 (Vink, 1996; Filella et al., 2009). In addition there is still a lack of reliable thermodynamic data relating to the formation of secondary minerals, especially Sb(V) precipitates from aqueous solutions (Selim, 2012; Roper et al., 2012). The kinetics of crystallization and transformation of secondary minerals into other ones still remains to be fully understood.

Due to the abundance of calcium, magnesium, sodium and potassium in soils, antimony compounds typically form many precipitates with these elements. Many of these alkali metal hydroxyantimonate salts have a high solubility at ambient conditions, 0.4 $g \cdot L^{-1}$ for mopungite, $Na[Sb(OH)_6]$, 0.5 $g \cdot L^{-1}$ for brandholzite, $[Mg(H_2O)_6][Sb(OH)_6]_2$, 15 $g \cdot L^{-1}$ for potassium hexahydroxoantimonate, $K[Sb(OH)_6]$ (Selim, 2012). Calcium antimonates, normally referred to as the roméite group, have shown to limit the solubility of antimony in supergene environments such as shooting range soils and mine site soils, where antimony concentrations are extremely high (Okkenhaug et al., 2011). Many calcium antimonates such as $Ca[Sb(OH)_6]_2$ and $Ca_2Sb_2O_7$ appear to be among the most insoluble antimony compounds in soils, 0.016 $g \cdot L^{-1}$ and 0.040 $mg \cdot L^{-1}$, respectively (Diemar et al., 2009; Selim, 2012). It is important to note that the latter compound roméite, $Ca_2Sb_2O_7$, as reported by Diemar et al. (2009) was shown to have a solubility that was three orders of magnitude smaller than previously reported by other researchers, which was the result of the crystallinity of the compound. Thus, the conditions of mineral synthesis, mainly the ratio Sb:Ca and pH, play a major role on the end crystalline structure and therefore its stability (Selim, 2012).

Antimony species, especially oxyanions, have shown to form precipitates in soils with heavy metals as well, when present. The heavy metals normally include lead, nickel, and iron, and are usually more plentiful in areas near anthropogenic sites. In particular, bindheimite, $Pb_2Sb_2O_7$ and iron antimonates schafarzikite, $FeSb_2O_4$, and tripuhyite, $FeSbO_4$, have shown extremely low solubilities, up to 9.3 $\mu g \cdot L^{-1}$ and a few $\mu g \cdot L^{-1}$, respectively (Diemar et al., 2009; Selim, 2012).

There is also ample evidence of adsorption of antimony onto iron and manganese oxyhydroxides that largely limit mobility in oxic environments (Belzile et al., 2001; Mitsunobu et al., 2010).

Due to its increasing documentation in the environment along with demonstrated industrial applications, tripuhyite has been the subject of several studies. Only in the past decade has it received more attention as a mineral that could limit the mobility of antimony, its historic occurrences were likely overlooked because it resembles goethite (Diemar et al., 2009; Leverett et al., 2012). Moreover, it has also been found in soils near antimony mine tailing sites by Mitsunobu et al. (2011) they have speculated that it likely formed in the aqueous wastewater solution and subsequently adsorbed onto soil grains. If this is the case, then tripuhyite may limit the mobility of antimony in both water and soil systems. Lastly, Leverett et al. (2012) have associated both tripuhyite and schafarzikite as being "ultimate sinks" of antimony in the natural environment because of their exceptional stabilities, likewise, Roper et al. (2012) concur and state that the minerals are "extraordinarily important with respect to immobilizing Sb under supergene conditions at ambient temperatures".

2.11 Review of tripuhyite synthesis

Since at least the 1980s, tripuhyite has received attention for its properties as a catalyst for hydrocarbon (amm)oxidation and gas sensing technologies (Teller et al., 1985; Centi et al., 1986; Tojo et al., 2008). There are a few methods of preparation, most of which consist of high temperature treatment rather than completely in–solution crystallization. The traditional methodology has been in–solution precursor precipitation with subsequent high temperature calcination or solely high temperature calcination of iron and antimony compounds. The main reason for why this methodology has been adopted is because the in–solution precipitation method has almost always resulted in amorphous to poorly crystalline tripuhyite, thus requiring high temperature treatments for further crystallization. There are countless research papers that have followed this methodology and it appears to have been the accepted norm where tripuhyite, or sometimes referred to as iron(III) antimonate, production is concerned. Although these methods may not be necessarily suitable for direct application to treatment of effluents or metallurgical flue dusts or residues nevertheless they can be provide useful insight hence they are reviewed. More specifically general flowsheets of the two processes are summarized below followed by newer methods of synthesis that have emerged over the past 5–10 years.

2.11.1 Precipitation and calcination

Iron and antimony compounds are introduced into an acidic medium, typically hydrochloric acid, followed by neutralization to an alkaline pH either with ammonia or sodium hydroxide to form a precursor precipitate (Berry et al., 1987; Gadgil et al., 1995; Tianshu et al., 1999; Sasaki, 2000; Huang et al., 2006). The precipitate is then processed in an oven by calcination at varying lengths of time (Figure 2.7 and 2.8(a)). An enhancement to this procedure was introduced by Nag et al. (2012) where prior to and after neutralization the solution was sonicated with ultrasound for 30 mins, after which the precipitate was calcined at lower temperatures (300 and 450 ^{o}C). The results indicate the presence of tripuhyite at lower temperatures in comparison to historic results, and as expected, crystallinity increased at higher temperatures (Figure 2.8(b)).

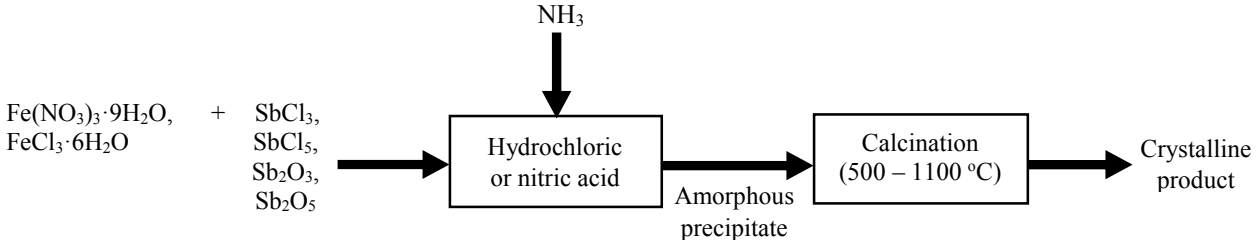

Figure 2.7 – *General flowsheet depicting the precipitation and calcination procedure to form crystalline tripuhyite, $FeSbO_4$.*

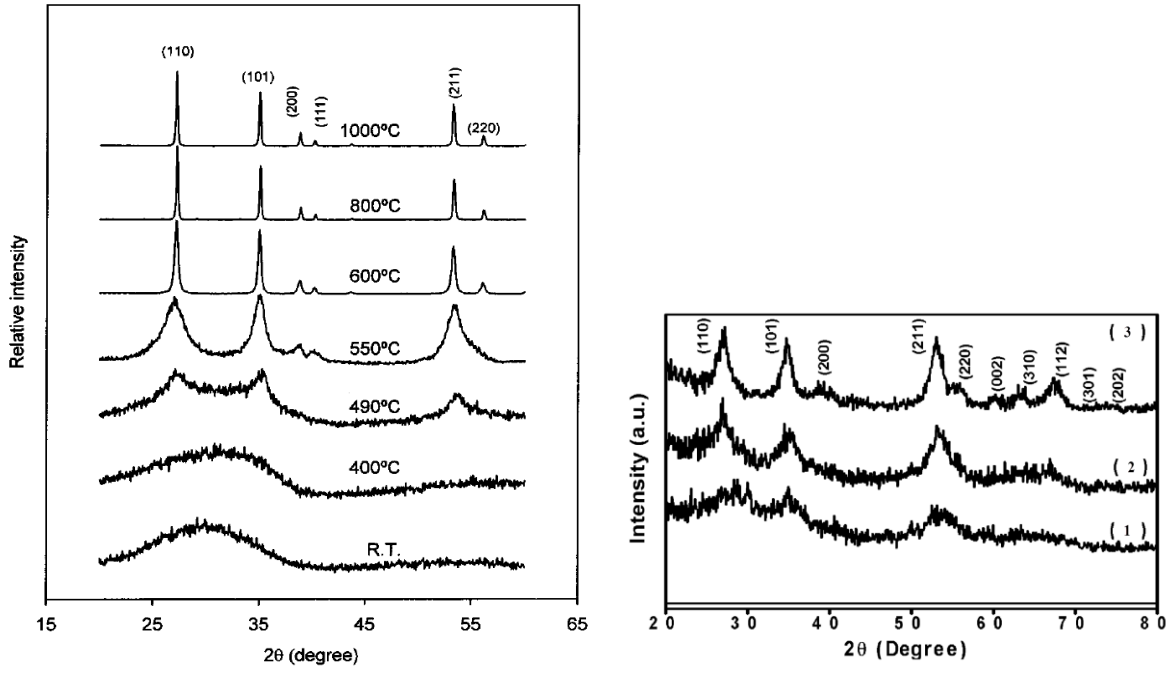

Figure 2.8 – *(a) X–ray diffraction patterns of co–precipitated powders calcined at room temperature to 1000 ^{o}C for 3 hrs in air, reproduced from Tianshu et al. (1999). (b) X–ray diffraction patterns of co–precipitated powders, (1) as prepared, (2) 300 ^{o}C calcined for 6 hrs, (3) 450 ^{o}C calcined for 6 hrs, modified from Nag et al. (2012).*

2.11.2 Grinding and/or calcination

Grinding and calcination

A few studies have tried to determine the effectiveness of solid–state reactions (grinding) prior to calcination as opposed to precipitation. Hematite, Fe_2O_3, ground with antimony trioxide, Sb_2O_3, followed by calcination was the method used in studies by Tianshu et al. (1999) and Huang et al. (2005). The results demonstrate the plausibility of producing tripuhyite in this fashion, however, due to the incongruent oxidation of both compounds, the production of tripuhyite still takes place at a fairly high temperature (> 800 ^oC) with other species still present until ~ 1000 ^oC.

Grinding only

The production of tripuhyite by milling without the addition of heat or subsequent calcination was studied by Berry et al. (2004) and Tojo et al. (2008). Barry et al. (2004) used mixtures of α–Fe_2O_3 and Sb_2O_3 at various grind times to determine phase changes of the compounds and residence time requirements for tripuhyite synthesis. Their results are summarized in Figure 2.9 where the onset of tripuhyite formation takes place at ~ 190 hrs, after which its crystallinity increases with more grind time.

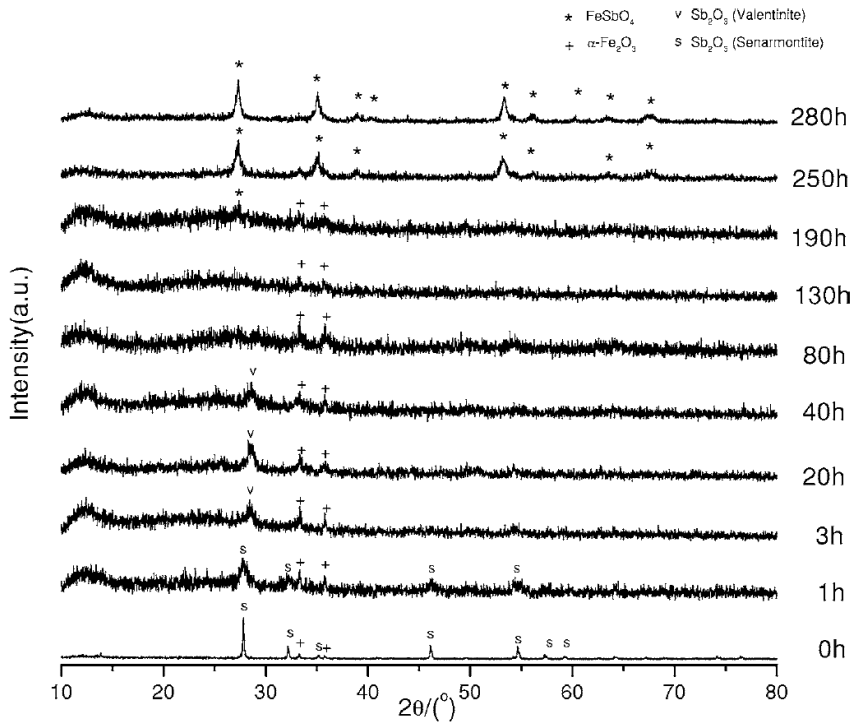

Figure 2.9 – *X–ray powder diffraction patterns of α– Fe_2O_3 and Sb_2O_3 mixtures (1:1 Fe:Sb molar ratio) at various mechanical milling times, reproduced from Berry and Ren (2004).*

Tojo et al. (2008) also performed mechanical milling at room temperature on iron and antimony powders, however, they chose iron oxy–hydroxide, FeOOH, and antimony pentoxide, Sb_2O_5, as their starting raw materials. As a result of this, the residence time for tripuhyite synthesis was considerably reduced, where the onset of formation took place at ~ 1 hr, after which subsequent grinding resulted in increased crystallinity (Figure 2.10(a)). Moreover, the authors also varied the starting Fe:Sb ratio to determine its effect, the results in Figure 2.10(b) show the decreasing peak intensity of tripuhyite with increasing Fe:Sb ratios, demonstrating the importance of initial Fe:Sb ratios on product crystallinity.

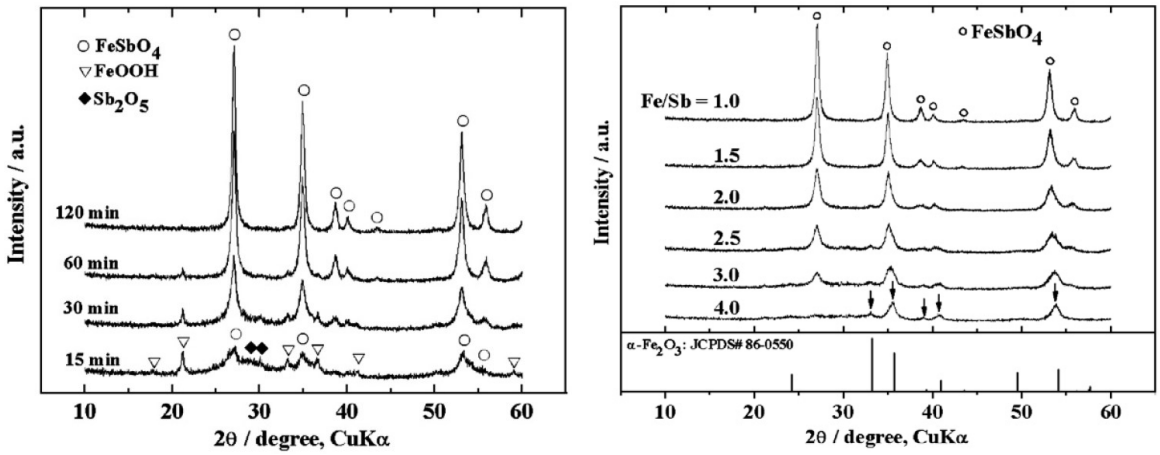

(a) **(b)**

Figure 2.10 – *(a) X–ray powder diffraction patterns of FeOOH and Sb_2O_5 mixtures (1:1 Fe:Sb molar ratio) at various mechanical milling times. (b) X–ray powder diffraction patterns of FeOOH and Sb_2O_5 at different Fe:Sb ratios, milled for 120 mins, reproduced from Tojo et al. (2008).*

From an industrial point of view, synthesizing tripuhyite for market or environmental waste disposal from these methods, whether calcination or grinding alone at room temperatures, seems to be very energy intensive and therefore costly. The cost of the process can be separated into high electricity costs (to maintain oven/furnace temperatures for continuous production or continuous milling), capital costs (oven/furnace, mills, mill media, extra supporting infrastructure), pretreatment of raw materials (filtration, drying, pelletizing, etc.), potential lengthy downtimes (oven/furnace start up and shutdowns, mill re–lining and maintenance), reagent costs, and general maintenance. Therefore, a process that is cost effective and better suited for large scale mining–derived Sb bearing–waste treatment. Although unsuccessful up to date in the case of Sb compounds, in–solution crystallization seems to be an attractive method considering that antimony is either in effluent solutions or previously solubilized before fixed in the case of mineral processing applications. Historically, the very stable arsenic compound scorodite, $FeAsO_4 \cdot 2H_2O$,

has been produced in solution to immobilize arsenic, either with hydrothermal autoclave treatment or supersaturation control at relatively low temperatures (< 100 ºC), yielding highly crystalline products. Antimony, which has many similarities with arsenic, can likely be treated in–solution to yield highly crystalline tripuhyite. This methodology has been validated in nature, where tripuhyite was observed in mine soils (Mitsunobu et al., 2011). The authors believed that the formation of tripuhyite likely involved the direct precipitation via neutralization from the acidic mine wastewater. Furthermore, they also note that a Fe:Sb threshold value of 1 lead to the formation of tripuhyite, where higher ratios resulted in other phases.

2.12 Stability of tripuhyite and schafarzikite

A comprehensive study concerning the stabilities of tripuhyite and schafarzikite was conducted by Leverett et al. (2012) with important findings. The authors synthesized both minerals and conducted solubility studies, resulting in stability constants of log K = –10.68 ± 0.10 and ΔG_f^o = –836.8 ±2.2 kJ/mol for tripuhyite (25 ºC, 0.195M HNO_3), and log K = –0.81 ± 0.01 and ΔG_f^o = –962.5 ±3.5 kJ/mol for schafarzikite (25 ºC, 0.1M HNO_3). They further extrapolated high temperature Gibb's free energies (from 771–981 K) from relationships determined by Swaminathan et al. (2003) and found that these calculated values were in excellent agreement with theirs at 298 K, demonstrating the viability of the relationship over a very large temperature range. Lastly, Leverett et al. (2012) developed a Pourbaix diagram, Figure 2.11, to illustrate the Fe–Sb–H_2O behaviour for dilute systems at ambient temperatures, which should prove useful in tripuhyite synthesis from aqueous solutions.

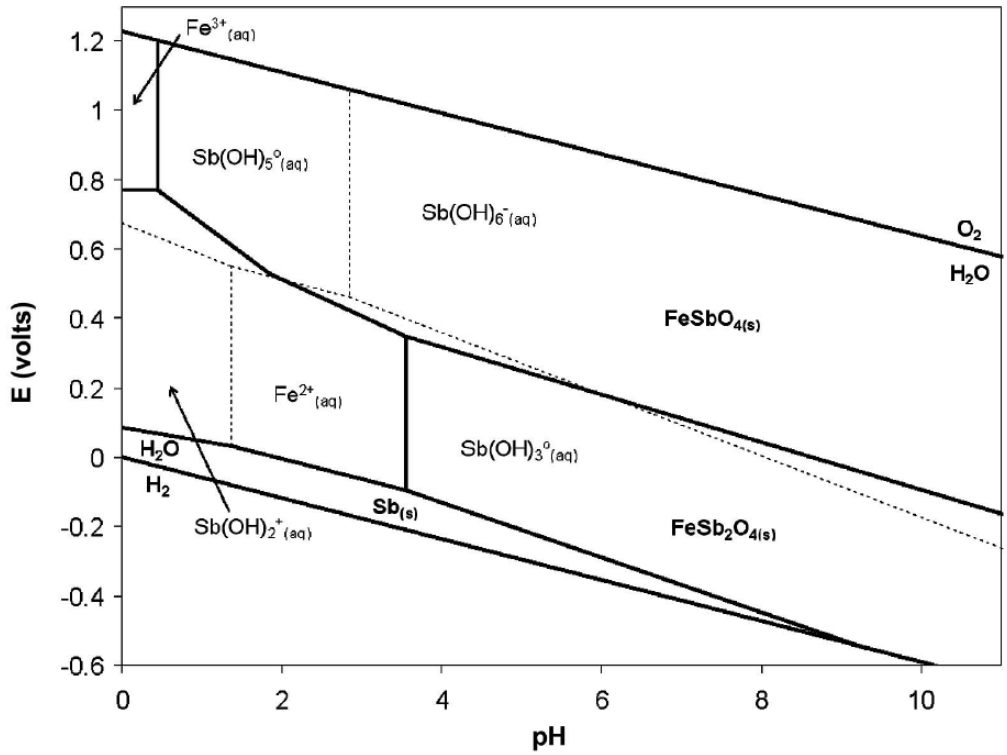

Figure 2.11 – *E_h–pH diagram for the Fe–Sb–H_2O system, calculated at 298.15K and total dissolved Sb and Fe concentrations of 10^{-6} mol·L^{-1}. Areas of predominant dissolved Sb species are separated by dashed lines, reproduced from Leverett et al. (2012).*

2.13 Crystallization and supersaturation control

There is a wealth of information available on the crystallization or precipitation of compounds from aqueous solutions. Crystallization is induced from supersaturated solutions through a specific mechanism. In general terms, it is: supersaturation of the aqueous solution, nucleation, followed by growth. The resulting precipitate(s) can exhibit a variety of properties and these are largely dependent on the processing conditions, namely (a) solid–liquid equilibria; (b) crystallization kinetics (supersaturation, nucleation, growth); (c) colloid–surface chemistry; and (d) reactor selection and design (Demopoulos, 2009).

2.13.1 Phase equilibria and kinetics

Precipitation of desired compounds requires information on the phase equilibria to determine conditions that favour one phase over another, these typically include temperature, pressure, concentrations, redox potentials, pH, essentially the system is defined thermodynamically. Caution needs to be used however as often various simplification assumptions and the use of unreliable data can lead to errors. Another aspect to consider is kinetics, although

the diagrams dictate which phases will eventually form after reaching equilibrium, there is no mention of kinetics, which gives rise to many metastable phases that co–exist with others, thus complicating matters even further. To induce precipitation of insoluble compounds the molar Gibbs free energy (ΔG) of the system must be $\Delta G < 0$:

$$\Delta G = -RT \ln(S) \tag{1}$$

Where, S ≡ saturation ratio

$$S = \frac{C}{C_{eq}} \tag{2}$$

Where, C ≡ concentration of the solute
C_{eq} ≡ equilibrium concentration

Equation (3) can be modified to yield the supersaturation ratio term as:

$$\frac{(C - C_{eq})}{C_{eq}} = S - 1 \tag{3}$$

Furthermore, solubility products may be used for ionic crystal precipitation ($A^+ + B^- \leftrightarrow AB_{(s)}$):

$$S = \frac{[A^+][B^-]}{K_{sp}} \tag{4}$$

Where, $K_{sp} \equiv [A^+]_{eq}[B^-]_{eq}$

Supersaturation is considered the driving force for crystallization, which takes place as nucleation followed by growth. Nucleation mainly occurs as (a) primary homogeneous (in the absence of a solid surface); (b) primary heterogeneous (on a foreign solid surface); (c) secondary heterogeneous (on a solid particle surface of the same type that precipitates) (Dirksen et al., 1991; Demopoulos, 2009).

The degree of supersaturation determines the type of nucleation. For homogeneous nucleation, the critical supersaturation ratio, $S_{cr,homogeneous}$, must be exceeded for it to take place (Demopoulos, 2009). For heterogeneous nucleation to take place, either primary or secondary, a surface must be provided. These are favoured over homogeneous nucleation when referring to energy requirements. Thus, nucleation can take place at lower supersaturation ratios, yielding the order $1 < S_{cr,surface} < S_{cr,heterogeneous} < S_{cr,homogeneous}$.

Figure 2.12 displays a plot of nucleation/growth rate as a function of the saturation ratio. As can be seen, there are two distinct regions of precipitation, homogenous (J_{homo}), which proceeds

exponentially with S ratio, and heterogeneous (G), which proceeds linearly with the ratio. Homogeneous precipitation leads to the formation of extremely fine particles. Heterogeneous precipitation, requiring a surface (i.e. seed), occurs when the saturation ratio is lower than $S_{cr,homogeneous}$, and leads to the production of well grown particles. Thus, from an industrial and crystal product perspective, the control of supersaturation is fundamental and must be operated below $S_{cr,homogeneous}$ (Demopoulos, 2009). Homogeneous nucleation leads to aggregation of fine particles and results in amorphous precipitates, whereas, heterogeneous nucleation & growth (with solid seeds of the same kind) results in a more crystalline precipitate, which takes place at a low supersaturation ratio. Crystalline precipitates are much more stable and normally have a considerably lower solubility than their respective amorphous counterparts, an example is the difference in solubility of roméite, $Ca_2Sb_2O_7$, as determined by two independent researchers, where the synthetic crystalline roméite exhibited a solubility that was at least three orders of magnitude lower than the amorphous solid (Diemar et al., 2009). Another example is of crystalline scorodite, $FeAsO_4 \cdot 2H_2O$, as opposed to amorphous ferric arsenate, $FeAsO_4 \cdot xH_2O$, having a reported solubility of at least two orders of magnitude lower than the amorphous compound (Krause and Ettel, 1989).

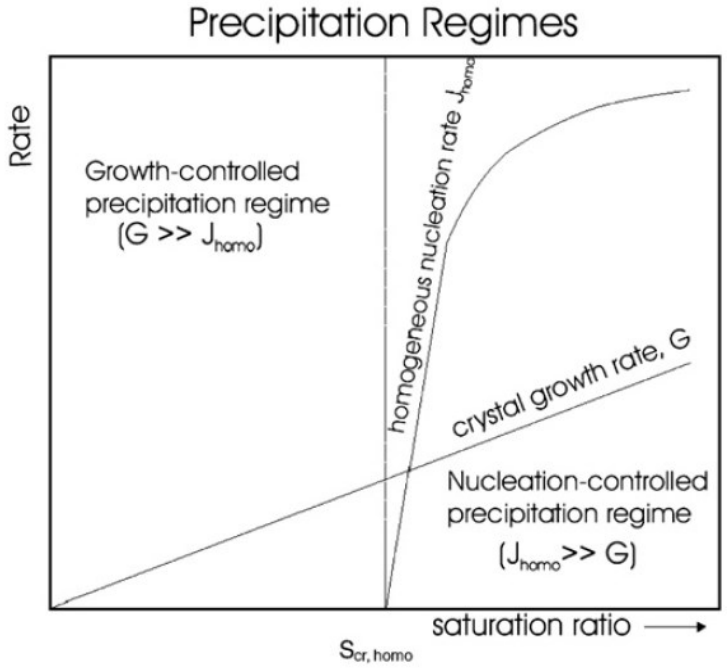

Figure 2.12 – *Nucleation and crystal growth rate as a function of the saturation ratio, displaying two distinct regions of precipitation, reproduced from Demopoulos (2009).*

2.13.2 Supersaturation control

There are several methods available to control supersaturation in practice, allowing the intricate manipulation of the nucleation and growth rate and morphology of the resulting precipitates. One of particular interest in relation to tripuhyite synthesis is the method of supersaturation control via pH regulation that was developed for the production of crystalline scorodite (Filippou and Demopoulos, 1997). Figure 2.13 displays the concept of supersaturation control. Initially, the solubility line, C_{eq}, is determined experimentally for solutions of similar concentration and temperature. Controlled precipitation of scorodite is carried out by stepwise neutralization as shown (stages 1 and 2 in Figure 2.13) with the addition of seed without surpassing the critical supersaturation line, C_{cr}. Thus, precipitation only takes place in the heterogeneous region, resulting in crystalline scorodite. If, however, the critical supersaturation line were surpassed at any stage, homogenous nucleation would ensue instantaneously, resulting in amorphous precipitates (Filippou et al., 1997). Figure 2.14 shows two distinct morphologies of scorodite, amorphous and crystalline, both of which are possible after neutralization, however, the actual method of neutralization yields one or the other, or even both. An example of transforming arsenic industrial waste into crystalline scorodite is demonstrated in Figure 2.15, which depicts a flowsheet to dissolve and oxidize arsenic trioxide waste in acid and treat via stepwise neutralization, effectively removing > 90% of the arsenic as scorodite.

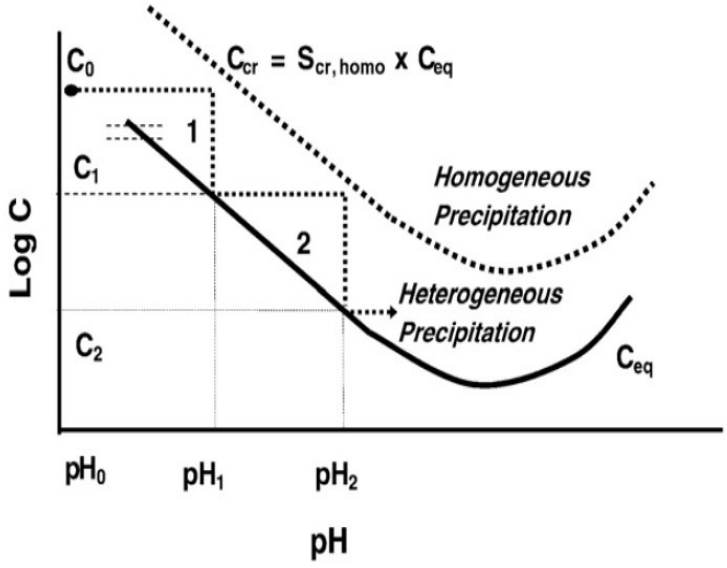

Figure 2.13 – *Concept of supersaturation control by stepwise neutralization; C_{eq} – equilibrium concentration, C_{cr} – critical supersaturation; $S_{cr,homo}$ – critical supersaturation ratio, reproduced from Demopoulos (2009).*

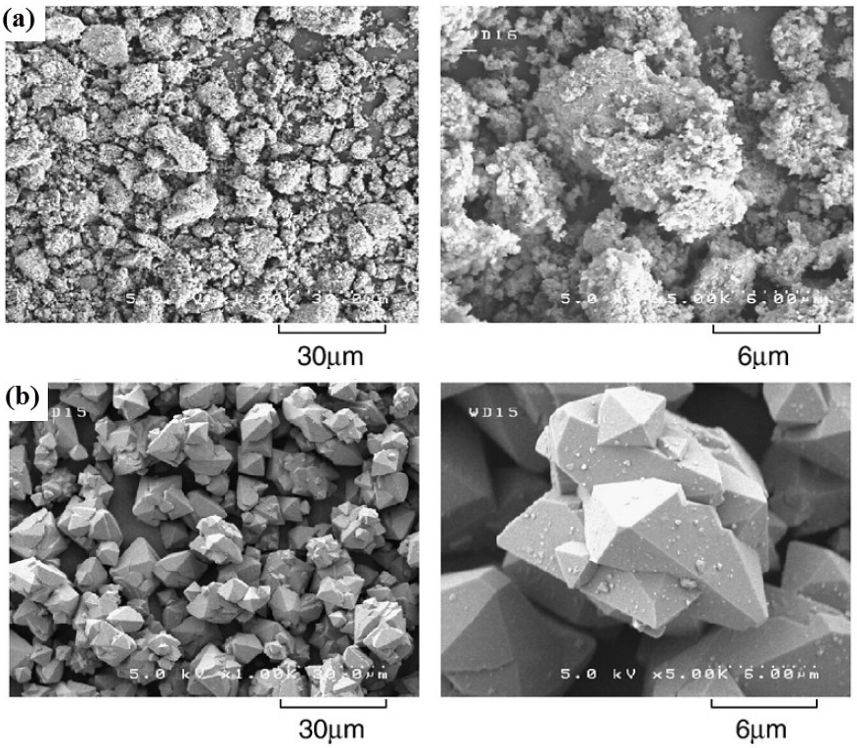

Figure 2.14 – *Displays different morphologies of scorodite, $FeAsO_4 \cdot 2H_2O$. (a) amorphous; (b) crystalline; reproduced from Fujita et al. (2009).*

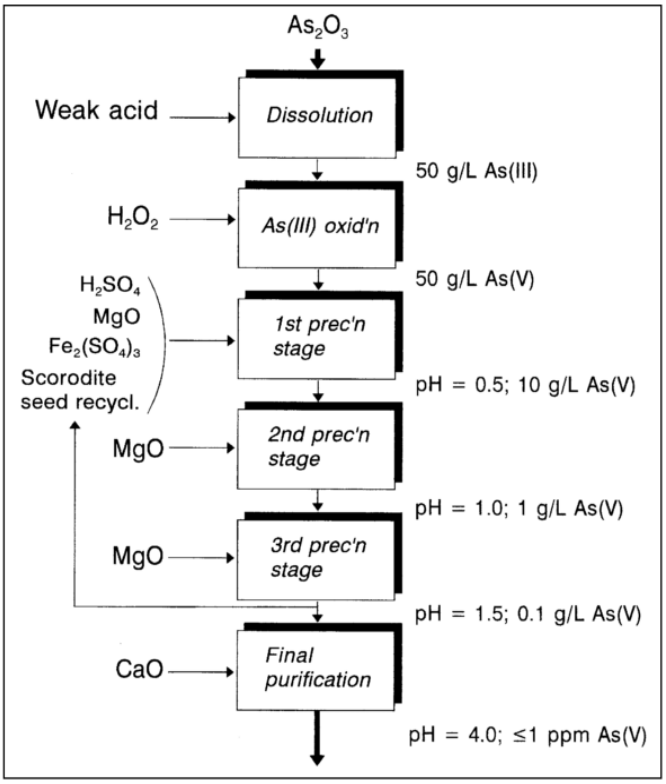

Figure 2.15 – *Flowsheet for the conversion of arsenic trioxide to crystalline scorodite; 95 °C, molar Fe:As = 1.2, reproduced from Filippou and Demopoulos (1997).*

Chapter 3 – Experimental

In this chapter, information is provided relating to methods, materials, and equipment used to synthesize, characterize and test tripuhyite, $FeSbO_4$. A flowchart describing the preparation sequence and stability testing that was followed is given in Figure 3.1. The synthesis involved (i) solution preparation using Fe(II) and Sb(III) salts, pH adjustment, and oxidative precipitation using hydrogen peroxide; (ii) treatment of precipitate in an autoclave (hydrothermal) or box furnace (calcination); (iii) stability testing; and (iv) characterization of different solid materials and solutions.

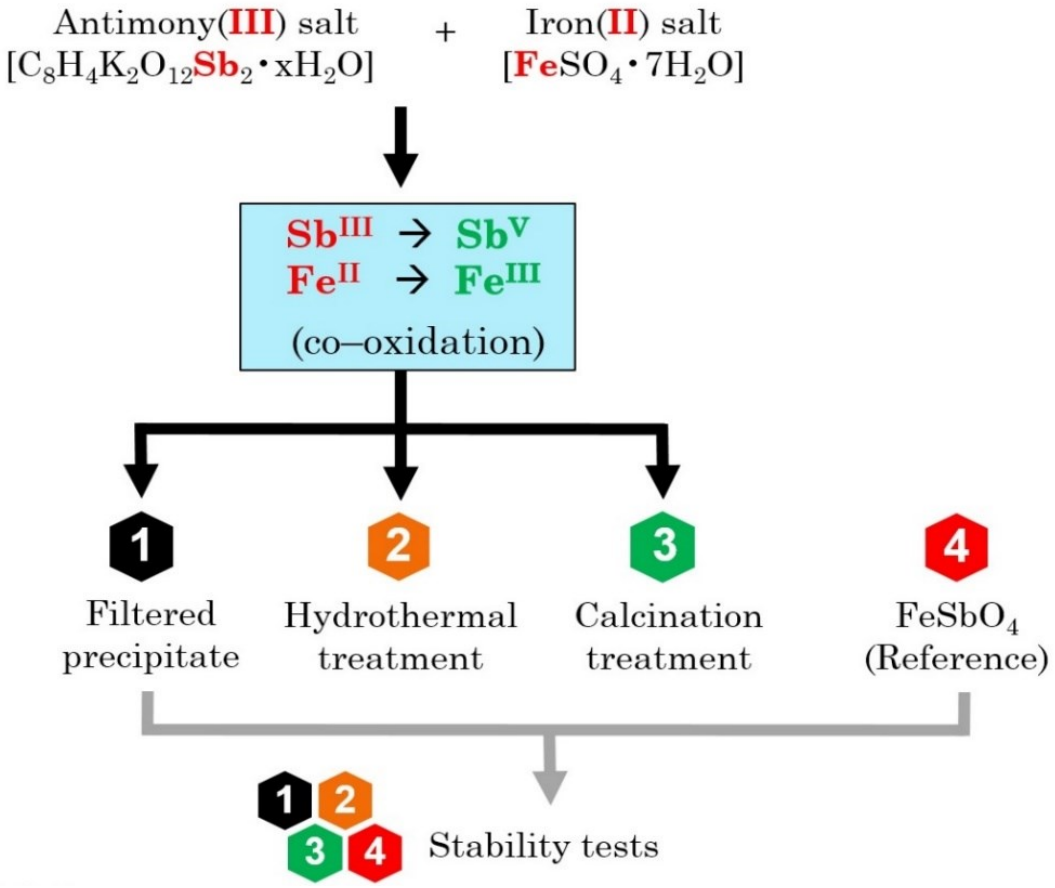

Figure 3.1 – *General flowchart employed in the synthesis and stability testing of different tripuhyite materials.*

3.1 Chemicals

All chemicals used are summarized in Table 3.1. Solutions were made using deionized water produced by reverse osmosis.

Table 3.1 – *Chemicals used in the experiments or processing of solids and solutions.*

Chemical	Formula	Purity	Source
Antimony(V) Oxide *(powder)*	Sb_2O_5	99.995%	Sigma Aldrich
Antimony(III) potassium tartrate hydrate *(powder)*	$C_8H_4K_2O_{12}Sb_2 \cdot xH_2O$	98%	Alfa Aesar
Calcium hydroxide *(powder)*	$Ca(OH)_2$	99%	Fisher Scientific
Ferric hydroxide oxide *(powder)*	FeOOH	96.9%	Sigma Aldrich
Hydrogen peroxide *(solution)*	H_2O_2	50 wt%	Fisher Scientific
Hydrochloric acid *(liquid)*	HCl	37.3%	Fisher Scientific
Iron(II) sulfate heptahydrate *(crystals)*	$FeSO_4 \cdot 7H_2O$	98%	Sigma Aldrich
Nitric acid *(liquid)*	HNO_3	67–70%	Fisher Scientific
Sodium hydroxide *(pellets)*	NaOH	99%	Fisher Scientific
Sulfuric acid *(liquid)*	H_2SO_4	96.5%	Fisher Scientific

3.2 Oxidation–precipitation reactor and procedure

The first step of the synthesis procedure involved preparation of the starting solution of Sb(III) and Fe(II) (0.05 M each)[3] followed by heating to 95 ^oC, pH adjustment (using 1 M NaOH as base) to pH 5.3, after which 10 wt% H_2O_2 addition was initiated to cause the precipitation of antimony as $FeSbO_4$. Over the course of H_2O_2 drop–wise addition (~ 3.5 hrs), the pH was kept constant (5.3). The conditions are summarized in Table 3.2. For one test, where quick oxidation (~ 20 mins) was investigated, following oxidation–precipitation, the precipitate–solution mixture was allowed to equilibrate for ~ 24 hrs at 95 ^oC and without the maintenance of pH.

The oxidative precipitation tests were run in a 2–liter glass stirred reactor[4] using the experimental setup depicted in Figure 3.2. The custom–made reactor was equipped with baffles to promote efficient mixing. The top of the reactor was sealed with a non–reactive plastic cover to prevent air infiltration. To ensure complete seal/air exclusion, the top of the reactor was lined with an adhesive tape. The solution temperature was maintained with a programmable Torrey Pines Inc. hot plate within ±1 ^oC. A Thermo Scientific pH meter monitored the solution pH (calibrated with standard buffer solutions of 4.01 and 7.0) with a temperature reference probe. A Cole Palmer

[3] To account for premature oxidation of Fe(II) by air, the use of excess iron was briefly investigated, however, it was found not to have a noticeable effect on precipitate crystallinity and an Sb/Fe ratio of 1 was used for all tests.

[4] Reactor diameter = 14 cm, marine–type propeller used for axial dispersion – diameter = 4.45 cm.

peristaltic pump (calibrated to operate at a specific dosage rate) was used to regulate the addition of hydrogen peroxide solution into the reactor over the course of 3.5 hrs.

Table 3.2 – *Oxidation reaction experimental conditions.*

Condition	Value
Solution volume (L)	2
Temperature (^{o}C)	95
Operating pH	5.3
NaOH base concentration (mol·L^{-1})	1
10 wt% H_2O_2 total volume (mL)	260
H_2O_2 dosage rate (mL/min)	1.2
Agitation speed (rpm)	500
Sb(III) concentration (g·L^{-1}, mol·L^{-1})	6.0, 0.05
Fe(II) concentration (g·L^{-1}, mol·L^{-1})	2.8, 0.05

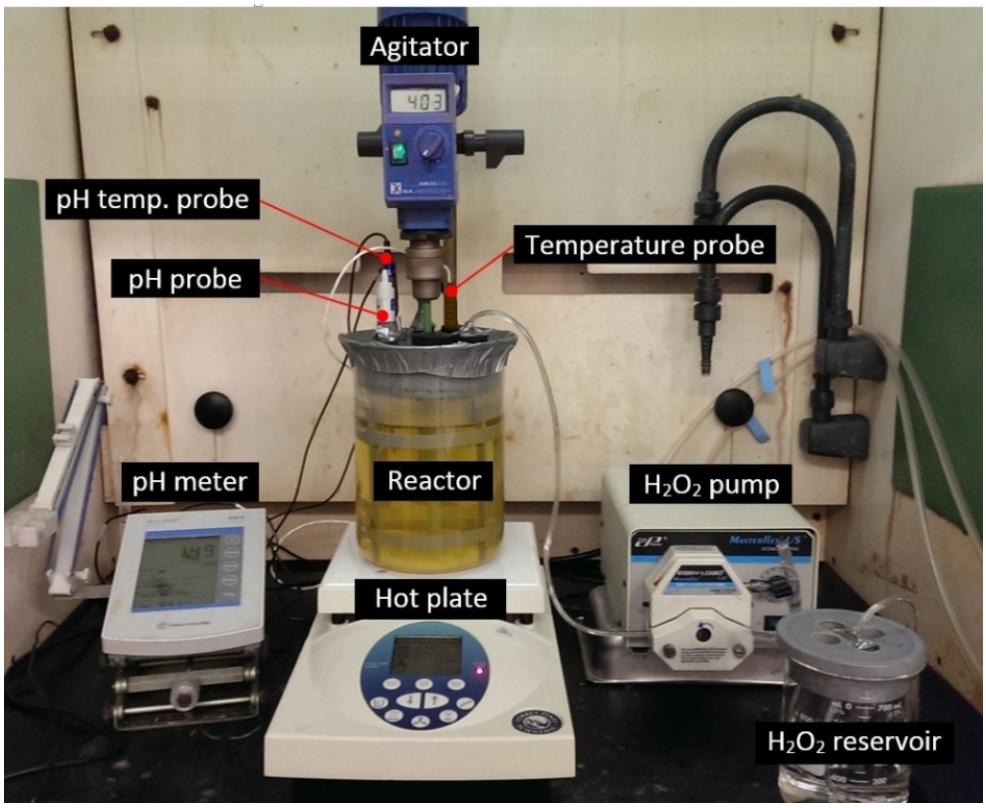

Figure 3.2 – *Oxidation–precipitation reactor setup.*

3.3 Pressure filtration, washing and drying

Upon completion of a precipitation test, the hot slurry was filtered and subsequently washed and dried before being further treated or tested/characterized. Filtration of the precipitate was rather difficult necessitating the use of a pressure filter. Due to the presence of very fine

particles settling took a very long time to be practical. The pressure filtration setup is displayed in Figure 3.3. The slurry was placed in the pressure filter (lined with an inert Teflon coating), pressurized to approximately 50 psi for 24 hrs after which the filtrate (2 L) was collected in a glass beaker. The typical filtration time for the slurry was between 20 – 24 hrs. The filter cake was collected using a filter membrane (0.22 µm PTFE)[5] and subjected to wash cycles.

In the wash cycle procedure, the filter cake was re–pulped in 1 L de–ionized water and agitated/mixed for 3 hrs, after which the slurry was pressure filtered again. Following the completion of wash cycles, the final filter cake was dried for 24 hrs at 50 ºC. The dried precipitate (~ 24 g) was ground by mortar and pestle and separated into 3 equal parts (~ 8 g), where 1 part (untreated) was retained for stability testing, 1 part was treated hydrothermally, and the remaining part treated by calcination. The hydrothermally and calcined products were also subjected to the same wash cycle procedure mentioned previously, where the only differences were the filtration times (4 – 5 hrs for the hydrothermal product, < 5 mins for the calcined product). The product filter cakes were also dried for 24 hrs at 50 ºC.

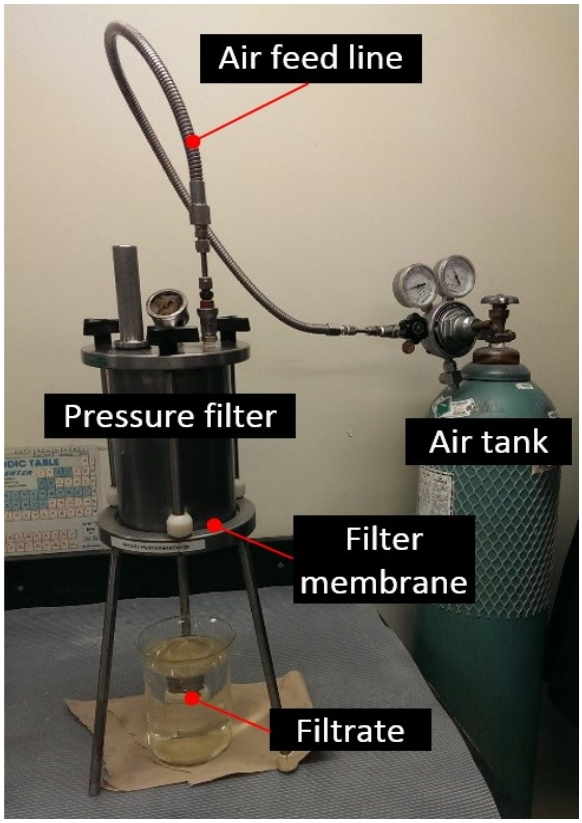

Figure 3.3 – *Pressure filtration setup with 0.22 µm PTFE filter membrane.*

[5] Effective filter membrane area = 17.7 in^2

3.4 Hydrothermal treatment (autoclave)

The hydrothermal treatment of the precipitate was conducted in a non–agitated Parr pressure bomb of 100 mL capacity equipped with a Teflon container as depicted in Figure 3.4. The dried precipitate was added into acidified (with H_2SO_4) deionized water (pH 1) placed in the Teflon container that was transferred into the pressure vessel for hydrothermal treatment as per conditions given in Table 3.3.

Figure 3.4 – *Teflon container (left) and the closed pressure bomb (right).*

Table 3.3 – *Hydrothermal treatment conditions.*

Condition	Value
Vessel volume (mL)	100
Temperature (^oC)	200
Mass of precipitate (g)	4.0
Solution volume (mL)	50
Solution pH	1.0
Treatment duration (hrs)	12

3.5 Calcination treatment and synthetic reference material (box furnace)

Calcination of the dried precipitate powder was conducted in a Thermo Scientific box furnace, depicted in Figure 3.5. The powder (8 g) was placed in a ceramic bowl, which was then calcined in the furnace in the presence of stagnant air. The synthetic reference material was made under the same conditions, however, the starting powder (15.67 g) was a mixture of 5.67 g goethite (FeOOH) and 10 g antimony pentoxide (Sb_2O_5), having a molar Fe:Sb ratio of ~ 1. The operating conditions are given in Table 3.4. After calcination, the powders were lightly ground by mortar and pestle to break down agglomerates.

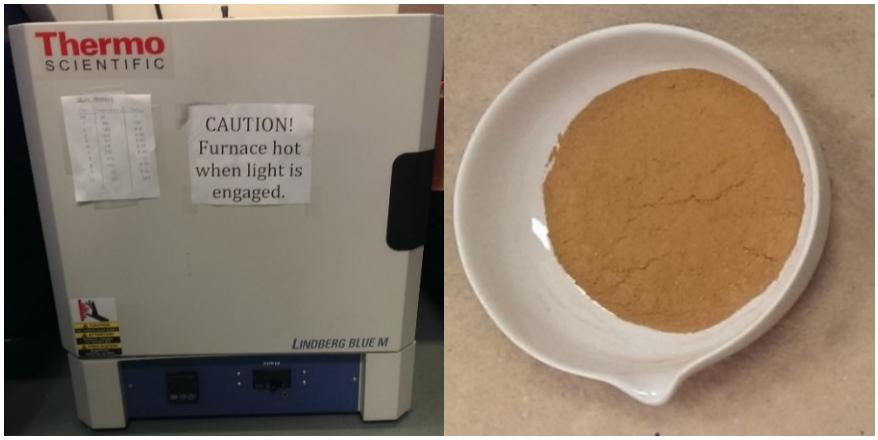

Figure 3.5 – *Thermo Scientific box furnace (left) and calcined precipitate in ceramic bowl (right).*

Table 3.4 – *Calcination treatment conditions.*

Condition	Value
Ramp up heating rate (degrees/hr)	230
Ramp up heating duration (hrs)	4
Operating temperature (^{o}C)	950
Treatment duration (hrs)	12

3.6 Stability tests

Representative powder samples of the different products (after washed/filtered, dried, and characterized) were subjected to stability testing to quantify the amount of antimony released along with other ions. Dried powder samples were placed in flasks containing deionized water, after which the solution pH was adjusted with 5 mM nitric acid or 1 mM lime (base)[6]. The flasks were sealed with Parafilm tape and placed on a shaker table (100 rpm) – Figure 3.6, they were opened only during sampling periods. Solution pH was monitored and aliquots were taken periodically (filtered with 0.22 μm syringe filters) to determine antimony concentration (among other elements). For each tested precipitate, a separate solution was monitored for natural pH drift and antimony release. Solutions whose pH drifted > ± 0.5 units were adjusted accordingly, except for the 'drift pH' series. The stability test parameters and pH test range evaluated are given in Tables 3.5 and 3.6, respectively.

[6] For high pH solutions (8 – 9), 20 mM lime was sometimes used to maintain pH if 1 mM were found to be insufficient.

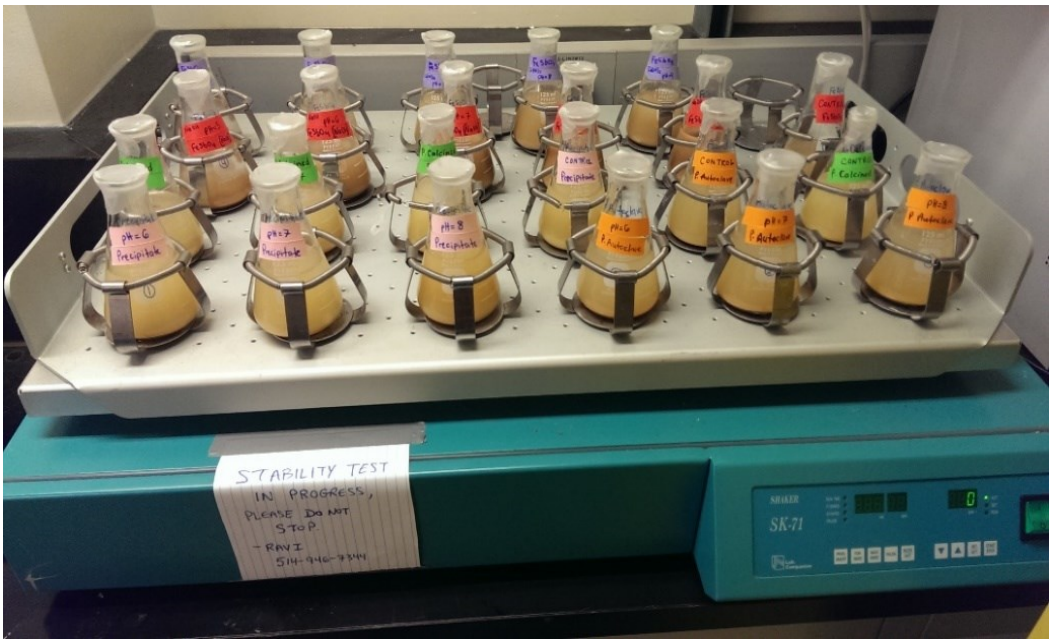

Figure 3.6 – *Stability test – precipitate samples in pH controlled solutions agitated on a shaker table.*

Table 3.5 – *Stability test parameters.*

Parameter	Value
Temperature (^{o}C)	22
Deionized water volume (mL)	100
Powder mass (g)	1.0
Acid concentration, HNO_3 (mol·L^{-1})	0.005
Base concentration, $Ca(OH)_2$ (mol·L^{-1})	0.001

Table 3.6 – *Solution pH range for each test. The 'unadjusted' indicates the natural pH drift samples.*

Test	Description	pH						Acid	Base
1	Untreated precipitate	--	6	7	8	--	unadjusted	HNO_3	$Ca(OH)_2$
2	Hydrothermal product	--	6	7	8	--	unadjusted		
3	Calcined product	--	6	7	8	--	unadjusted		
4	Calcined $FeOOH/Sb_2O_5$	5	6	7	8	9	unadjusted		

3.7 Characterization

3.7.1 Solution analysis (ICP–OES)

Solution samples (precipitation and stability tests) were analyzed with Thermo Scientific iCAP 6500 ICP–OES CID Spectrometer (Inductively Coupled Plasma – Optical Emission Spectroscopy). The precipitation test solution samples were diluted at a ratio of 400:1 and the stability test samples were diluted at 10:1 to fall within the 0 – 25 ppm (mg·L^{-1}) ICP–OES linear calibration range. The samples were diluted with 4% nitric acid to prevent subsequent precipitation

and were analyzed for antimony (Sb), iron (Fe), sodium (Na), sulfur (S), and calcium (Ca) at 217.5 nm, 259.9 nm, 588.9 nm, 182.0 nm, and 396.8 nm wavelengths, respectively.

3.7.2 Powder composition (ICP–OES)

Dried precipitate (powder) was ground by mortar and pestle to break down agglomerates and 0.01 g of material was placed in 4 mL of *aqua regia* (3mL concentrated HCl and 1mL concentrated HNO_3, 3:1 ratio) and brought to 95 ^oC. The powders were digested in 4 hrs and the acidic solution was then diluted to 50 mL with deionized water, after which they were further diluted by a factor of 10 to fall within the range of analysis. Antimony and iron concentrations were then measured by ICP–OES as described above.

3.7.3 Powder identification (XRD, Raman Spectroscopy)

Powder characterization for phase identification was performed with a Bruker Discover D8 – 2D Diffractometer using Co Kα radiation, which resulted in better–defined peaks than the Cu Kα radiation source. Samples were crushed with mortar and pestle to break down agglomerated particles before being analyzed. The diffractometer scan rate was set to approximately $3.5^o2\theta$/min, with the total acquisition time of 30 mins. The 2θ range was between 12.8 and 116.4^o.

Additionally, for further powder characterization, Raman spectroscopy was used – Renishaw System 1000 Raman microprobe, argon-ion laser (514.5 nm) excitation source – low power (25 mW), a holographic spectrometer, and a Leica microscope. The system used a 50x objective lens to collect the Raman signal, the spectra were acquired over 4 cycles.

3.7.4 Powder morphology (SEM)

For precipitate surface morphology, a Hitachi SU3500 scanning electron microscope was used at various accelerating voltages, all acquired in the secondary electron image mode. The powder samples were coated with nano–platinum to increase their conductivity and thus provide higher definition particle images. Without such coating, the samples exhibited charging, resulting in sub–adequate surface images.

3.7.5 Surface area (BET analysis)

Precipitate surface areas were determined with a Micromeritics Tristar surface area and porosity analyzer, using the Brunauer–Emmett–Teller (BET) model for gas adsorption. All powder samples were placed under vacuum for 24 hrs prior to the analysis. Further, at the time of analysis, samples were heat treated to between 200 and 350 ^oC for 2 hrs under the presence of nitrogen gas

to remove any remaining adsorbed gases, after which they were immediately placed in the analyzer.

3.7.6 Particle size analysis (PSA)

Particle size distribution (PSD) of the powder precipitates was determined with a Horiba Laser Scattering Particle Size Analyzer (LA–920). The powder samples were suspended in isopropanol and subjected to ultrasonication in the analyzer prior to analysis. Moreover, finer particle aggregates (untreated precipitate and synthetic reference material) were additionally treated with an ultrasonic horn (Cole Palmer Ultrasonic Processor Model CP 750 – CV 33) for 1 hr to ensure fully dispersible particles for representative results. The particle size distribution results were based on an equivalent spherical diameter, however, since all particles were not spherical, necessary corrections were made in the analyzer to account for different shapes. The refractive index for tripuhyite, between 2.14 and 2.27 (min and max), was retrieved from Berlepsch et al. (2003), and corrected for isopropanol.

Chapter 4 – Results and Discussion

4.1 Introduction

The aim of this work was to precipitate crystalline tripuhyite (ferric antimonate) from aqueous solutions and evaluate it in terms of stability as potential candidate for the fixation of antimony encountered in mineral and metallurgical waste streams. To this end, various tests were carried out under different conditions drawing from our group's experience with the analogous atmospheric scorodite precipitation system (Demopoulos, 2005). These precipitation tests are described in Sections 4.2 and 4.3. As it was not possible to obtain high crystallinity tripuhyite by direct precipitation, a two–step crystallization approach was investigated where the precipitate after filtration was subjected to either hydrothermal treatment or calcination. These tests are described in Sections 4.4 and 4.5. In Section 4.6 the synthesis of tripuhyite by solid–state reaction at high temperature, for the purpose of using it as reference, is described. Finally in Section 4.7 the precipitate, as–prepared and after hydrothermal treatment or calcination, is subjected to leachability tests along with the reference tripuhyite material to determine their stability as a function of pH.

4.2 Preliminary precipitation tests

Iron and antimony can be present in the starting solution as either reduced (II, III, respectively) or oxidized (III, V, respectively) species, yielding several reaction combinations. Ultimately, both elements must exist in their oxidized states when precipitating from solution since the target compound, tripuhyite ($FeSbO_4$), contains iron and antimony at these oxidation states. In the early stage of the work different combinations of Fe(II), Fe(III), Sb(III), and Sb(V) were studied and it was determined for ease of supersaturation control, the reduced oxidation states of iron and antimony (II, III, respectively) would be preferred for the starting solution, as tests using either species in their respective oxidized states resulted in premature precipitation. For the co–oxidation of Fe(II) and Sb(III), H_2O_2 was used. Oxidation with other less costly reagents such air and oxygen were not investigated in the present work.

After having selected co–oxidation to effect the precipitation of ferric antimonate, several preliminary tests were conducted to determine the effect of pH on the precipitate crystallinity as well as if the Fe(II)/Sb(III) molar ratio and equilibration following precipitation were critical. For all tests, the precipitation temperature was set at 95 ^{o}C, initial concentrations of Sb(III) and Fe(II)

were 0.05 mol·L^{-1} (Sb/Fe molar ratio = 1), and 10 wt% hydrogen peroxide (H_2O_2) was used at 100% excess.

The effect of small iron excess was briefly investigated and it was found not to have a noticeable effect on precipitate crystallinity, thus for the tests described here the Sb/Fe ratio was 1 unless if explicitly stated otherwise. Typical precipitation results from a preliminary oxidation test (pH = 5.3), where Fe(II) and Sb(III) were simultaneously oxidized by drop–wise H_2O_2 addition, are plotted in Figure 4.1. In this test excess iron was used (Fe(II)/Sb(III) ≈ 1.15) to account for partial oxidation of Fe(II) by air as was also observed in the case of the Fe(II)/As(V) system studied by Daenzer et al. (2014). With co–oxidation, the solution becomes supersaturated with respect to the oxidized species (Fe(III) and Sb(V)), resulting in precipitation. At the end of co–oxidation period all Sb had precipitated while a minor fraction of iron that was used in excess remained in solution. The latter, at all likelihood, was in the form of ferrous as otherwise ferric iron, if present, would have precipitated via hydrolysis due to elevated pH (5.3). Following oxidation, the precipitate/solution mixture was allowed to equilibrate for ~ 24 hrs for the purpose of increasing precipitate crystallinity via ripening (Demopoulos, 2009). At the end of this equilibration period all remaining dissolved iron species had precipitated due to apparent oxidation by air infiltration and hydrolysis.

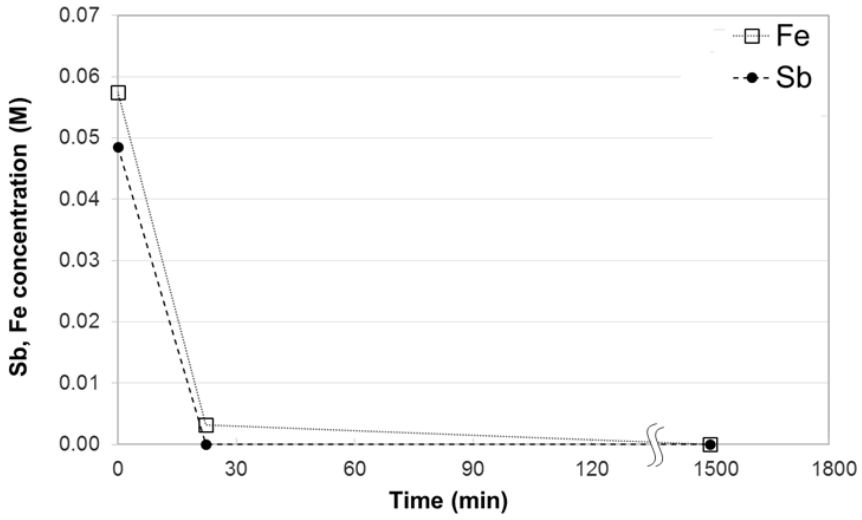

Figure 4.1 – *Iron and antimony concentrations (mol·L^{-1}) for the co–oxidation experiment with equilibrium treatment as a function of time, constant pH 5.3, 95 °C, after ~ 20 mins of oxidation, solution was allowed to equilibrate for ~ 24 hrs.*

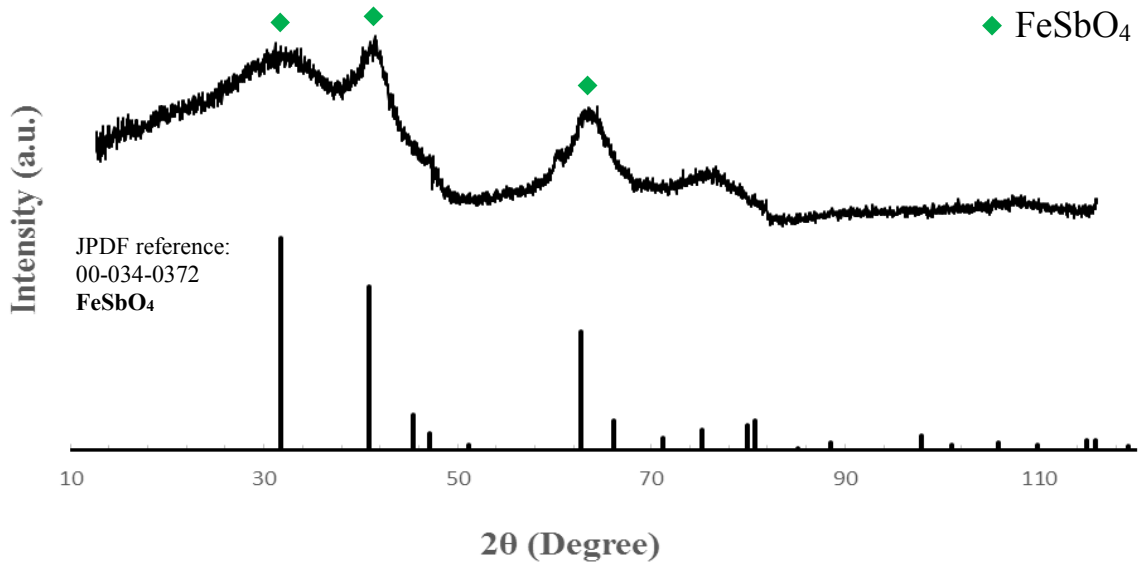

Figure 4.2 – *(Top) X–ray powder diffraction pattern of precipitate produced after quick oxidation (~ 20 mins) followed by equilibration (~ 24 hrs), pH = 5.3; (Bottom) reference tripuhyite pattern ($FeSbO_4$) – JPDF (00-034-0372).*

The X–ray diffraction pattern of the precipitate from the above described preliminary test is shown in Figure 4.2. There is good resemblance to tripuhyite's pattern, however, the material was found to be poorly crystalline. Although peaks at 2θ angles of 32°, 41°, 63°, and also 80° are present, they are rather broad with large backgrounds. In the following series of tests it was chosen that the oxidation be carried at slower rate by using drop–wise addition of H_2O_2 over 3.5 hrs instead of the 20 mins used in the test described in Figure 4.1. Slow drop–wise addition of H_2O_2 has proven effective in previous work dealing with the oxidation of As(III) as it considerably avoids the loss of the reagent that undergoes rapid decomposition at high temperature (90 °C) (Lin et al., 1991; Dabekaussen et al., 2001). In the present case, in addition to this factor the motivation was the potential beneficial effect that slow oxidation can have on tripuhyite crystallization. This is because quick oxidation (about 20 mins) may be linked to a high degree of supersaturation that is conducive to homogeneous nucleation, which in turn can lead to the production of fine and poorly crystalline particles as a consequence of Stranski's rule (Demopoulos, 2009). This series of slow oxidation tests was carried out at different pH values with no equilibration treatment.

Figure 4.3[7] displays antimony and iron concentration profiles over 3.5 hrs of oxidation time at constant pH of 1.5, 2.8, 3.95, and 5.3. No equilibration treatment was employed in this series. The oxidation time was about 10 times that of the preliminary tests with same amount of

[7] All concentration data for each test in Figure 4.3 are given in the Appendix.

oxidant used (still at 100% excess), however, diluted to 10 wt%. There are some characteristic differences among the various pH oxidation–precipitation results. In the very acidic region, pH = 1.5 (a), selective removal of antimony was observed via the apparent oxidation of Sb(III) to Sb(V) and the formation of an unidentified phase, most likely antimony pentoxide. Iron precipitation started when antimony precipitation was almost complete. It was not possible to confirm the formation of Sb_2O_5 by XRD, possibly because of its amorphous nature. However, Sb_2O_5 in contrast to Sb_2O_3 is very insoluble, 0.02 $g \cdot L^{-1}$ Sb at 35 °C according to Baes and Mesmer (1986), and since iron had stayed in solution this is the most likely phase. The behaviour of iron deserves specific consideration. Surprisingly, it appears that at this pH, H_2O_2 acted preferentially on Sb(III) and only after the latter was mostly oxidized did the oxidation and precipitation of iron start[8]. However iron precipitation was still not complete, with approximately 1/3 remaining in solution as Fe(II). At this pH, ferrous is soluble but not ferric (Daezner et al., 2014). The incomplete oxidation of Fe(II) may be attributed to decomposition of H_2O_2 but it was not investigated further. Incidentally, after 24 hrs, the filtrate showed signs of ferric precipitation (brownish colouration), apparently owing to slow air oxidation, indirectly confirming the assumption of H_2O_2 decomposition.

[8] Leuz et al. (2006a) proposed the following reaction mechanism for the preferential oxidation of Sb(III) to Sb(V), consuming and generating Fe(II) ions, at pH 2.9, 25 °C:

(1) $Fe^{II} + H_2O_2 \rightarrow Fe^{III} + {}^{\bullet}OH$ (or a reactive intermediate, possibly Fe^{IV})
(2) $Sb^{III} + {}^{\bullet}OH \rightarrow Sb^{IV}$
(3) $Sb^{IV} + O_2 \rightarrow Sb^{V} + O_2^{\bullet -}$
(4) $Fe^{III} + O_2^{\bullet -} \rightarrow Fe^{II} + O_2$

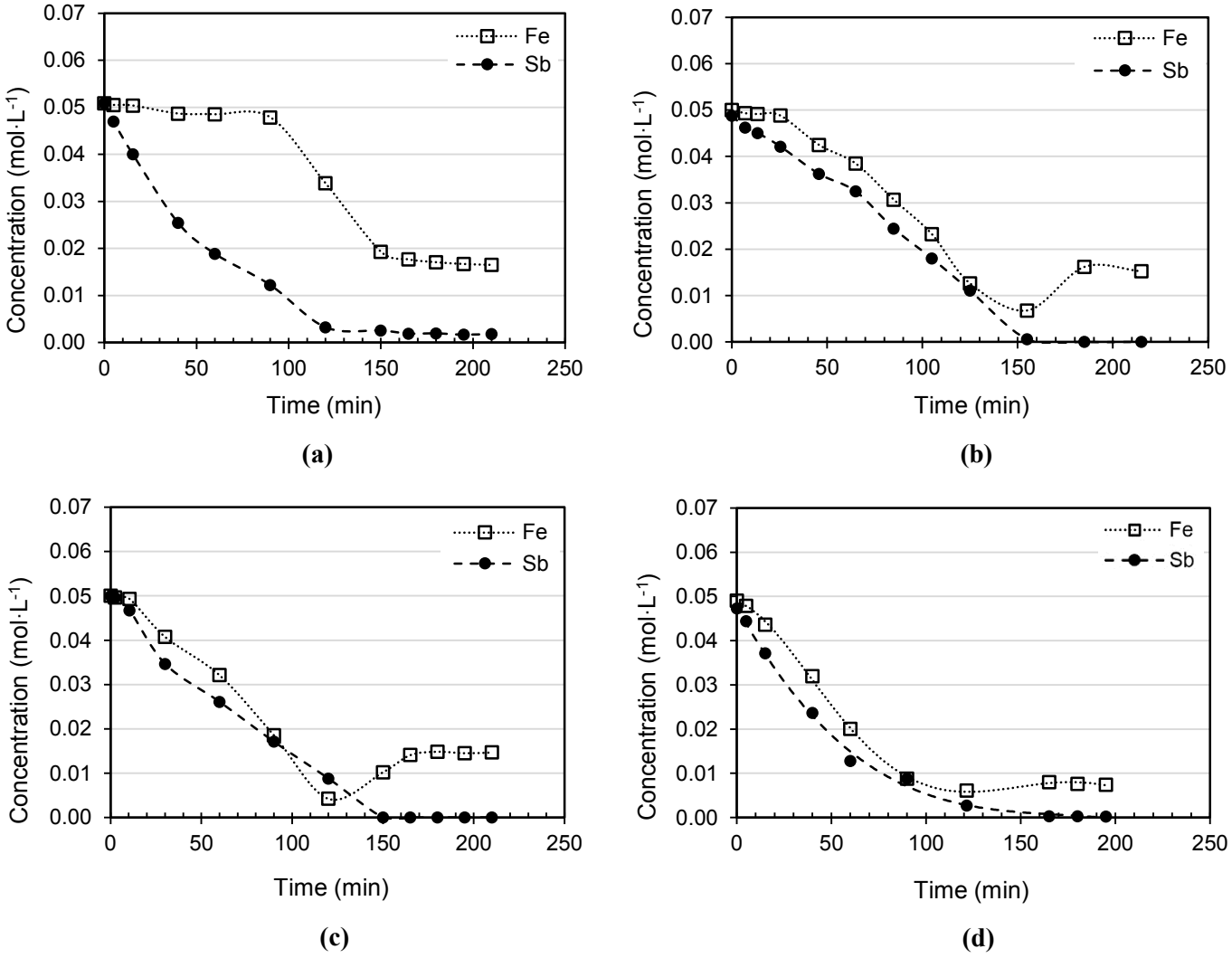

Figure 4.3 – *Iron and antimony concentrations (mol·L^{-1}) as a function of oxidation time, oxidized via drop wise addition of 10wt% H_2O_2 at a rate of 1.2 mL·min^{-1} and constant pH, 1M NaOH base, 95 ^{o}C; (a) pH = 1.5; (b) pH = 2.8; (c) pH = 3.95; (d) pH = 5.3.*

With increasing pH (2.8 and above) (Figure 4.3(b), (c), and (d)), there was co–current removal of both Fe(II) and Sb(III) with strange Fe(II) behaviour near the end of H_2O_2 addition, where Fe(II) was observed to reappear in solution. The reason for this behaviour was not apparent but it once more points to incomplete oxidation of Fe(II). At higher pH this behaviour was minimized, implying more complete Fe(II) oxidation apparently due to less H_2O_2 decomposition. Notwithstanding this intriguing iron precipitation feature, from the standpoint of antimony removal the precipitation of antimony was complete and subsequent tests sought to ascertain the type of precipitate formed.

After filtration the dried powders were ground and analysed by X–ray diffraction (XRD). Figure 4.4[9] displays the powder XRD patterns. It can be observed that there is good correspondence of the diffraction peaks of the precipitates with those of tripuhyite's reference pattern. While the co–precipitation profiles of Sb and Fe at pH 2.8 and higher were indicative of a tripuhyite stoichiometry (Fe/Sb ratio one) the same is not true for the test run at pH 1.5. It seems in this case following the preferential early stage precipitation of Sb_2O_5, the latter started reacting with the in–situ forming Fe(III) to ultimately yield a precipitate with the apparent features of tripuhyite.

By closely examining the XRD patterns it becomes evident that with increasing pH (Figure 4.4(a) to (d)), there is a noticeable decrease in precipitate crystallinity, however, all precipitates demonstrated a higher degree of crystallinity than the preliminary test in which 10 times faster oxidation was effected (Figure 4.2). The better crystallinity obtained with slower oxidation may be attributed to lower supersaturation that allowed for the relative growth of semicrystalline particles after the initial homogeneous nucleation event as per LaMer's theory (Demopoulos, 2009). Along the same lines, the observed trend of decreasing crystallinity with increasing pH could be the result of high supersaturation at higher pH. This behaviour is similar to the iron and arsenic system (scorodite crystallization) where at higher pH (2 to 6) the degree of supersaturation is much higher than the critical supersaturation ratio and results in the production of amorphous particles (Filippou et al., 1997; Demopoulos, 2009).

[9] The X-ray powder diffraction patterns in terms of 'counts' is given in the Appendix.

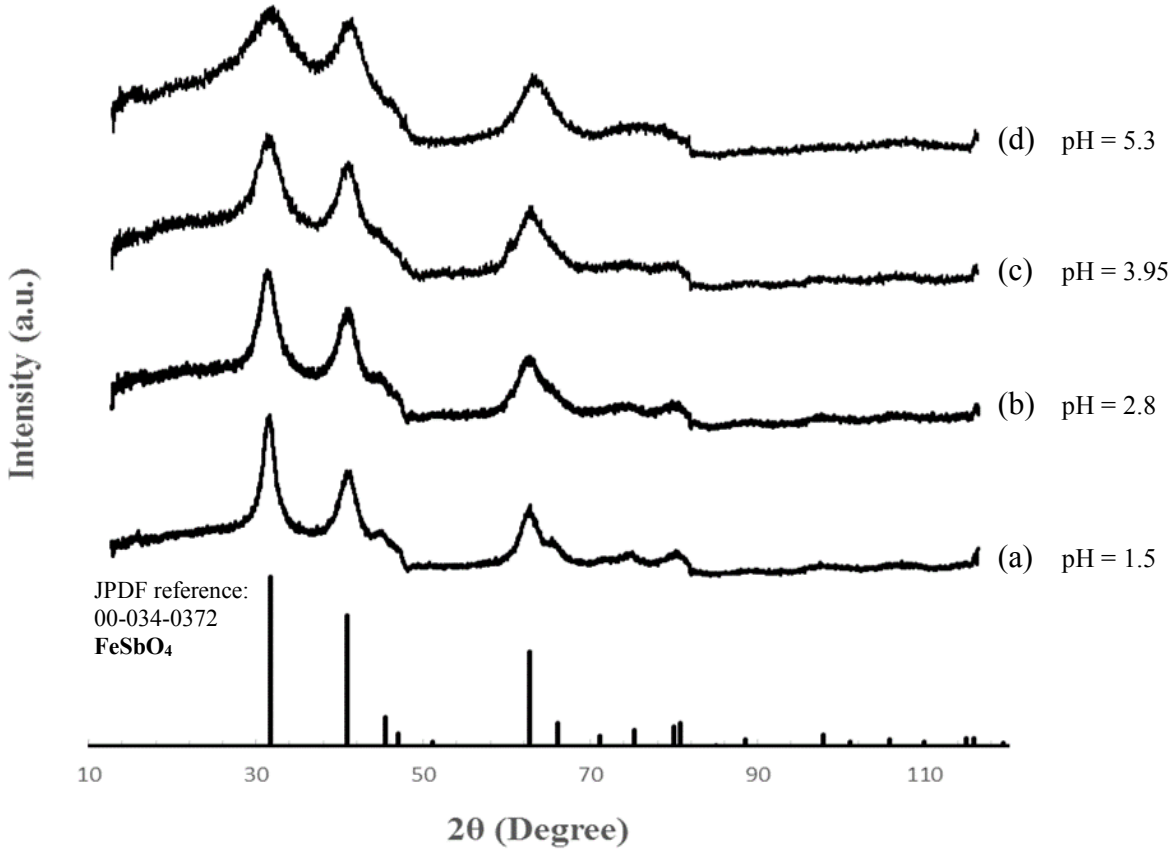

Figure 4.4 – *X–ray powder diffraction patterns of the precipitates produced at different pH: (a) pH = 1.5, (b) pH = 2.8, (c) pH = 3.95, (d) pH = 5.3, and the reference tripuhyite pattern ($FeSbO_4$) – JPDF (00-034-0372).*

Analysis of the precipitate composition yielded Sb/Fe molar ratios of 1.32, 1.27, 1.22, and 1.14 at pH 1.5, 2.8, 3.95, and 5.3, respectively (Table 4.1). With increasing pH, the precipitate molar ratio follows a linear trend (in the tested pH range) as seen in Figure 4.5, approaching the ideal ratio of one. From the excess Sb, it was inferred that the precipitates were not comprised solely of a tripuhyite–like phase, which has a molar ratio of one, but of other co–precipitated minor phases. The fact that Fe(II) was not completely oxidized may suggest that a Fe(II)–SbO_4 co–precipitate with Fe/Sb ratio more than one (like $Fe_3(SbO_4)_2$) cannot be ruled out until more analytical data is collected. XRD could not detect any other phases than poorly crystalline tripuhyite because even if present most likely were masked under the broad background in the XRD pattern. Among the possible phases that were cross–checked in the database and not detected were: $FeSb_2O_4$; $NaSb(OH)_6$; $NaSbO_3$; Sb_2O_3; Sb_2O_4; and Sb_2O_5. Their "absence" could have been due to either low concentration or amorphous/poorly crystalline character or a combination of both.

Table 4.1 – *Precipitate Sb/Fe molar ratios, calculated after digesting solids in aqua regia.*

Precipitate	Sb/Fe ratio (molar)
(a) pH = 1.5	1.32
(b) pH = 2.8	1.27
(c) pH = 3.95	1.22
(d) pH = 5.3	1.14

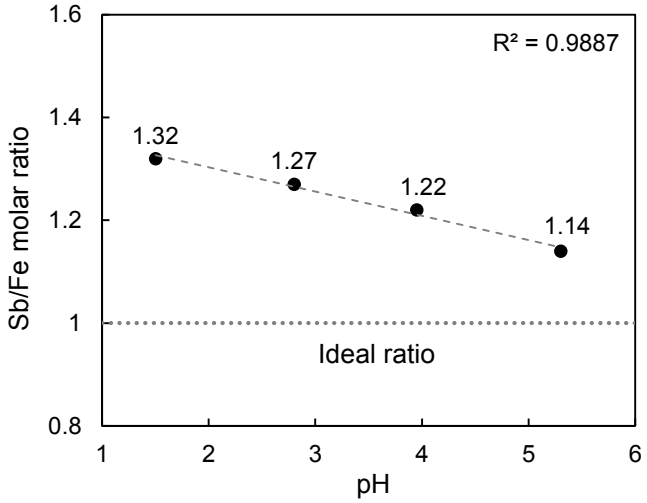

Figure 4.5 – *Precipitate Sb/Fe molar ratio as a function of precipitation pH.*

Upon evaluation of the presented preliminary precipitation data, pH 5.3 was chosen as the most ideal to produce tripuhyite from aqueous solutions by the co–oxidation method. This is so because at this pH the Sb/Fe molar ratio was nearly one (less likelihood of co–precipitation of other phases) and iron oxidation–precipitation was also almost complete under the applied conditions. The precipitation of tripuhyite at pH 5.3 is more closely studied in the following section.

4.3 Oxidation–precipitation at pH 5.3

4.3.1 Oxidation–precipitation reaction chemistry

The experiment was repeated at the specified pH (5.3) with minimal differences, indicative of good reproducibility as shown with the concentration profiles in Figure 4.6[10]. Once more the slow oxidation resulted in co–current removal of both Sb(III) and Fe(II) with all antimony

[10] Sb(III) and Fe(II) concentration profiles (see Appendix) at pH 5.3 without the addition of oxidant (H_2O_2) display minimal decrease in concentrations, thus the drops in Sb(III) and Fe(II) concentrations in Figure 4.6 was effected by the drop–wise addition of H_2O_2.

removed, while still ~ 20% of Fe(II) remained in the final solution. As a result, precipitate Sb/Fe molar ratio was determined to be 1.14.

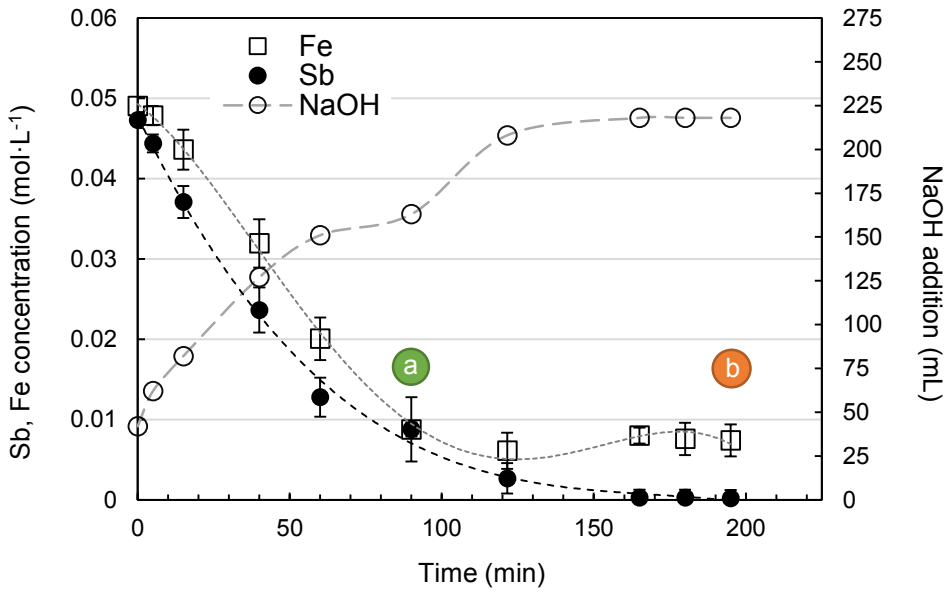

Figure 4.6 – *(Left axis) Antimony and iron concentration (mol·L^{-1}) as a function of oxidation time; oxidized via drop wise addition of 10 wt% H_2O_2 at a rate of 1.2 mL·min^{-1} and constant pH (5.3), 1M NaOH base, 95 °C. (Right axis) total sodium hydroxide addition over oxidation time. Circles 'a' and 'b' represent sample points at 90 and 195 mins, respectively.*

The progress of oxidation–precipitation was also monitored visually as per pictures shown in Figure 4.7. The first tank (golden yellow) depicts the solution at 95 °C and pH 3.3. The second tank represents the solution after pH adjustment to 5.3 (with NaOH) and just before H_2O_2 drop–wise addition, having a green colour (it was speculated that the colour represented very minor oxidation of Fe(II) to Fe(III) possibly in the form of green rust, a mixed Fe oxidation state complex). With further addition of the oxidant, the solution became opaque due to precipitation and gradually changed from green to orange, the colour change was due to increased mass of suspended particles, which were orange/brown in colour (depicted bottom–right). The filtrate solution samples taken over oxidation time became lighter in colour (depicted bottom–left), which transitioned from green to medium–yellow to virtually colourless, indicating the removal of dissolved species over the course of oxidation.

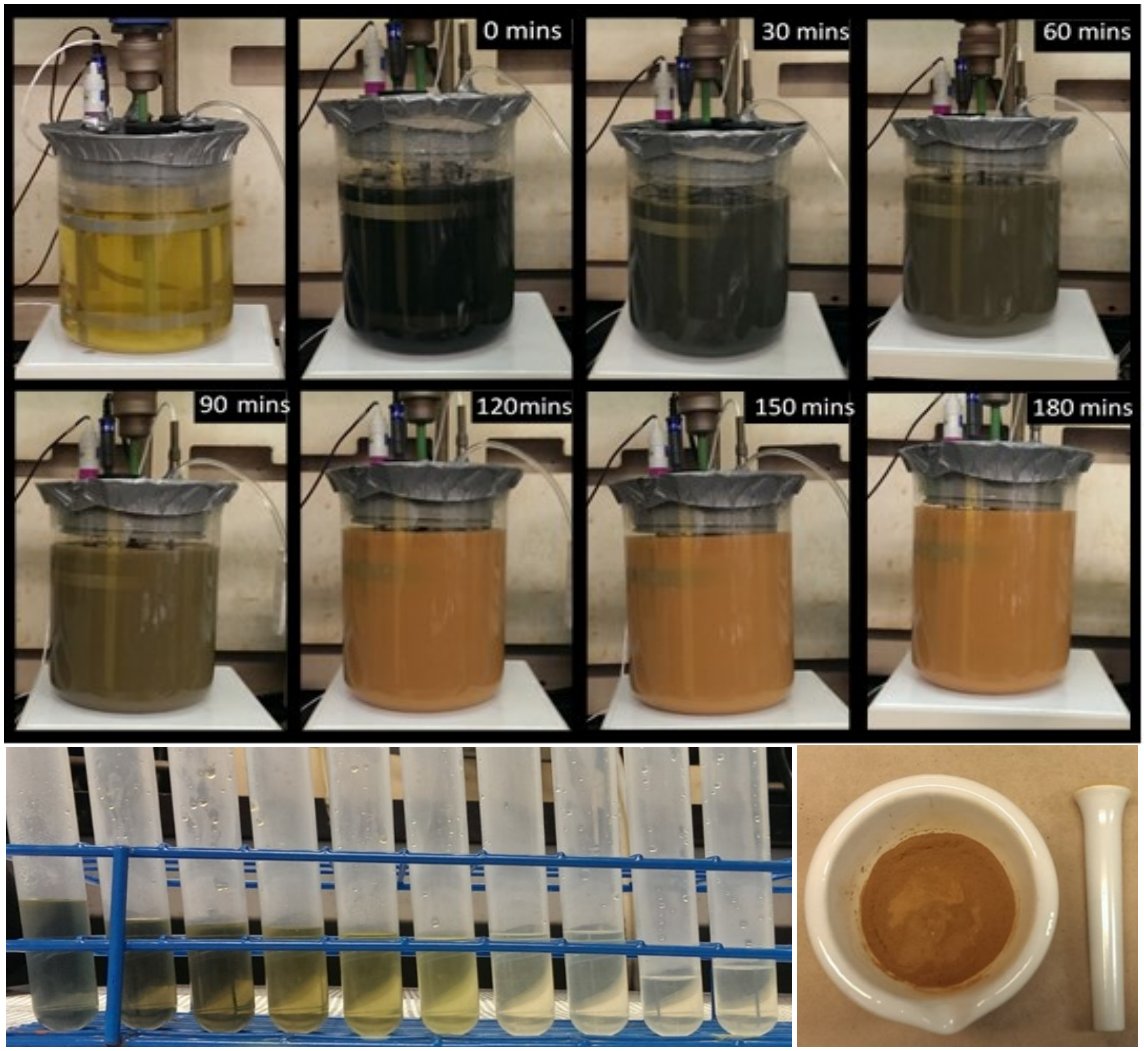

Figure 4.7 – *Solution colour change during oxidation–precipitation (top); filtrate solution over oxidation time (bottom left); ground dried precipitate powder (bottom right).*

In terms of reactions taken place during oxidation–precipitation, the following are tentatively proposed. The oxidation of antimony is represented by making use of the dominant Sb(III) and Sb(V) species, $Sb(OH)_3$ and $Sb(OH)_6^-$, as discussed in Section 2.8.1:

$$Sb(OH)_3 + H_2O_2 + H_2O \rightarrow Sb(OH)_6^- + H^+ \quad (1)$$

$$2Fe^{2+} + H_2O_2 + 2H^+ \rightarrow 2Fe^{3+} + 2H_2O \quad (2)$$

Upon oxidation, Fe(III) and Sb(V) species start accumulating in solution, reaching a critical supersaturation value that triggers formation of the first precipitate nuclei:

$$Sb(OH)_6^- + Fe^{3+} \rightarrow FeSbO_4 + 2H_2O + 2H^+ \quad (3)$$

The above (simplified) reaction scheme is a net acid producer that required NaOH addition for pH maintenance.

According to the Sb and Fe concentration profiles presented in Figure 4.6, Fe was always in excess to Sb, signifying Sb/Fe > 1 in the solid precipitate. In order to elucidate the nature of the forming precipitate and its evolution with time it was decided to collect samples at points 'a' and 'b', as marked in Figure 4.6, and determine the type of Sb (III vs. V) and Fe (II vs. III) species. At both sample points, the slurry and its filtrate were titrated for Fe(II) content[11]; total Fe was determined by ICP–OES; the slurry was filtered, washed and dried, and the solids were analyzed by XRD and Raman spectroscopy (Figure 4.8). For sample 'a', at 90 mins, slurry titration indicated that about 95% of Fe in the solid was present as Fe(II) and the filtrate Fe was entirely Fe(II) (matching the total Fe in solution). For sample 'b', at 195 mins (end of experiment), slurry titration indicated that about 1% of Fe in the solid was present as Fe(II) and the final filtrate Fe was 33% Fe(II) (5% of initial Fe(II) concentration), the remaining Fe in solution was most likely colloidal Fe(III) hydroxide/ferrihydrite that passed through the 0.22 μm filter as also previously observed during scorodite dissolution studies (Bluteau and Demopoulos, 2007). The XRD (a; Left) pattern in Figure 4.8 suggests a mixed phase material for sample 'a'; many of the sharp peaks can be attributed to Sb_2O_4 ($Sb^{III}Sb^{V}O_4$) whereas the broad background is attributed to 2–line ferrihydrite (Cornell and Schwertmann, 2003). The latter was not expected as according to titration results Fe in the solid was primarily (95%) Fe(II). As the fresh solid had a greenish appearance, it is postulated that at least part of the iron was in the form of 'green rust' (i.e. $Fe^{II}_2Fe^{III}(OH)_5SO_4$) that was oxidized (although precautions were taken to prevent this) to 2–line ferrihydrite by the time XRD analysis was conducted. The Raman spectrum of sample 'a' (a; Right in Figure 4.8) shows no resemblance to the reference pattern of tripuhyite, however the sharp peaks are characteristic of iron oxides (Oh et al., 1998) and likely the result of air oxidation (similar to the XRD result). By contrast the XRD pattern of sample 'b' carries the characteristic features of tripuhyite (XRD (b; Left)), though still poorly crystalline that is also validated by the Raman spectrum (b; Right), where the strongest peaks can be matched to the reference tripuhyite.

[11] For Fe(II) titration procedure, see Appendix.

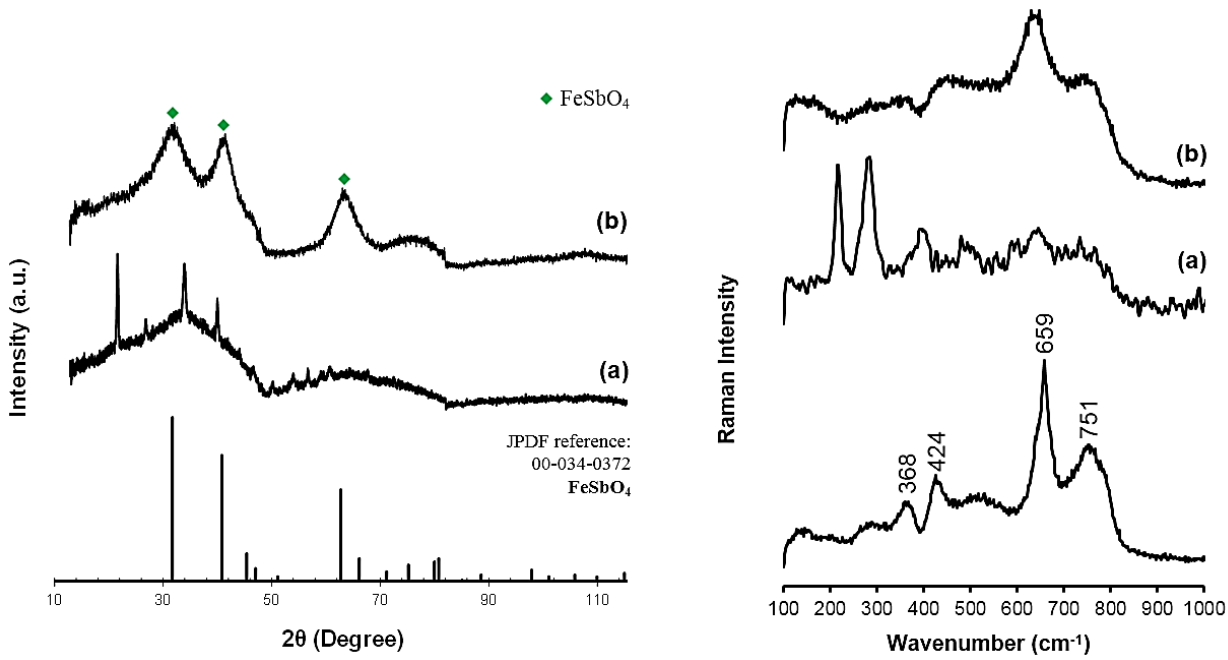

Figure 4.8 – *(Left) X–ray powder diffraction: {bottom} reference tripuhyite pattern ($FeSbO_4$) – JPDF (00-034-0372), filtered/dried precipitate at (a) 90 mins and (b) 195 mins; (Right) Raman spectra: {bottom} reference tripuhyite (synthetic), filtered/dried precipitate at (a) 90 mins and (b) 195 mins.*

On the basis of the above findings, the mechanism of tripuhyite formation in the above Fe(II)–Sb(III) co–oxidation system appears to have proceeded in two steps. Firstly, Sb(III) was preferentially (vis-à-vis Fe(II)) oxidized to an intermediate oxidation state oxide, Sb_2O_4 with co–current precipitation of Fe(II). The latter at least in part may be thought to have precipitated as green rust with the remaining Fe(II) co–precipitated via adsorption onto Sb_2O_4. A third possibility is that some sort of amorphous compound of the form 'Fe(II)–Sb(III,V)' had precipitated but no reports of such compound could be found in literature, making this scenario highly unlikely. The preferential Sb(III) oxidation over Fe(II) has been proposed by other researchers as well (Leuz et al., 2006a), although in more acidic solutions and lower temperatures, as well as oxidation of Sb(III) from $Fe(OH)_3$ surface sites where Fe(III) is reduced to Fe(II) (Belzile et al., 2001). Secondly, with continued oxidation, Sb(III) oxidized to Sb(V) and Fe(II) to Fe(III) yielding the final poorly crystalline tripuhyite product. The proposed two step selective oxidation, firstly of Sb(III) followed by Fe(II), is indirectly supported from the NaOH base demand (Figure 4.6) for neutralization of the acid generated by hydrolysis. Base requirement was significant at the beginning (levelling off at 90 mins) and significant once more after 100 mins (levelling off near

end of experiment), suggesting two hydrolysis events that coincided with the two–step invoked mechanism.

To explain the strange behaviour of Fe reintroduction into solution, sodium concentration was studied for possible correlation, this was pursued because sodium may form the following two salts with Sb(V); mopungite ($NaSb(OH)_6$) and/or brizziite ($NaSbO_3$). During the experiment, all solution additions (H_2O_2 and NaOH) and subtractions (due to sampling) were precisely monitored to account for dilution effects on antimony and iron concentrations over time. Since both the volume and concentration (1 M) of added NaOH were known at every sampling point, a theoretical sodium concentration was calculated and compared to actual concentration from ICP analysis. Figure 4.9[12] displays the expected (calculated) sodium concentration with the assumption that sodium was not a participant in the reaction. As observed in the Figure the actual Na concentration begins to diverge approximately after 90 mins of oxidation. From this correlation, it was inferred that some sodium was removed from solution becoming more pronounced after 90 mins. As it can be seen, antimony and iron concentrations follow a similar trend (co–current removal) for the initial half of oxidation period, however, after approximately 100 mins, iron removal was halted and its concentration was virtually constant. Coinciding with this behaviour, sodium concentration was observed to decrease near the same time when iron concentration became steady, suggesting preferential removal/substitution of sodium over iron after ~ 80% antimony removal. The mechanism by which sodium was removed was most likely via adsorption rather than precipitation of the two possible sodium antimonates, $NaSb(OH)_6$ and $NaSbO_3$, considering the higher (than tripuhyite) solubility of these salts.

[12] Concentration data for Figure 4.9 is given in the Appendix.

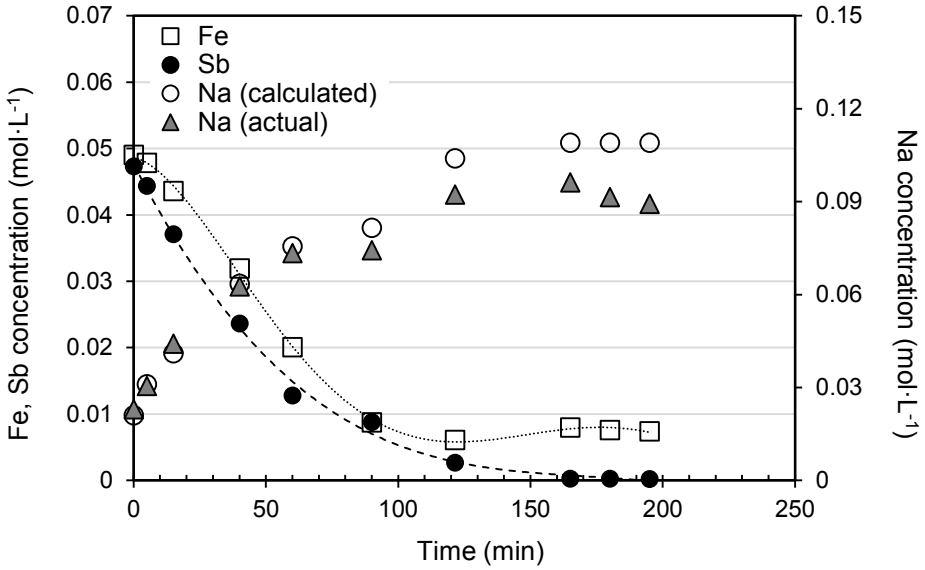

Figure 4.8 – *Antimony (left axis), iron (left axis), and sodium concentrations (calculated and actual) (right axis) over oxidation time.*

4.3.2 Precipitate characterization

The produced precipitate was subjected to different characterizations after first being washed and dried. In terms of washing, the 2 liter slurry following pressure filtration as per procedure outlined in section 3.3, yielded filtrate iron, antimony, and sodium concentrations ($mg \cdot L^{-1}$) as a function of wash cycles, which are displayed in Figure 4.10. The wash cycles were continued until a constant concentration of the species was observed, where free iron was removed below the detection limit of the ICP, however, antimony and sodium concentrations remained constant after 3 wash cycles. With continuous washing, the sodium impurity was still present within the pores of the agglomerated precipitate particles and it was deemed impractical to continue past 5 wash cycles. In terms of moles, the residual Sb and Na values (~ 10 $mg \cdot L^{-1}$ each) reported in the 5^{th} wash cycle give a molar ratio ~ 5 – 6, i.e. they do not seem to relate to soluble $NaSb(OH)_6$ co–precipitated impurity but rather adsorbed species released slowly upon repeated equilibration in de–ionized water.

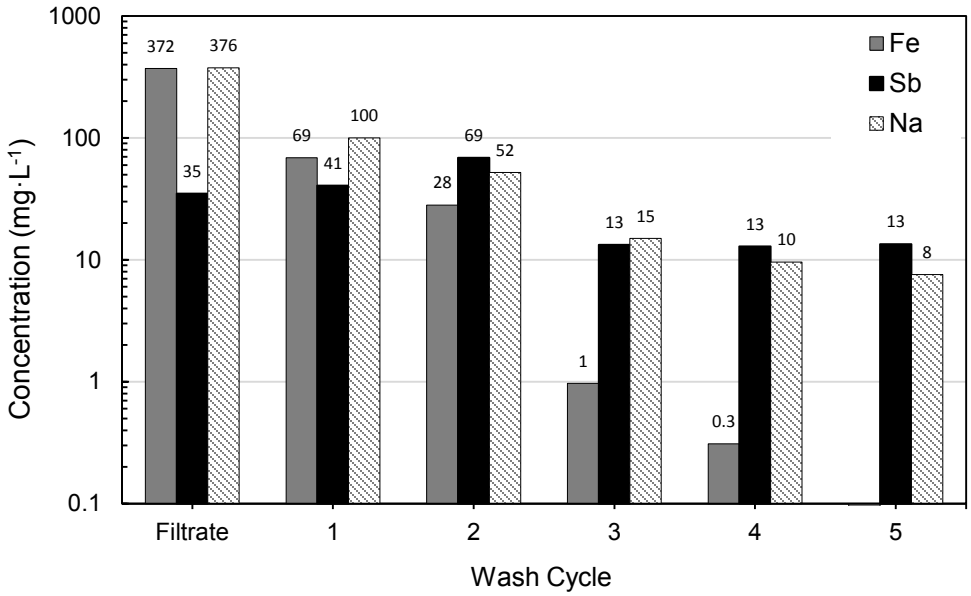

Figure 4.9 – *Iron, antimony and sodium filtrate concentrations at different wash cycles.*

The dried precipitate powder was analyzed by X–ray diffraction, Figure 4.11, confirming its poorly crystalline tripuhyite–like phase that was also detected during the preliminary experiments. Peaks matching those of the reference pattern for tripuhyite were noted, however, they are broad and indicative of poor degree of crystallinity. Thus, post–precipitation treatments were investigated to increase the precipitate crystallinity as described in the next sections.

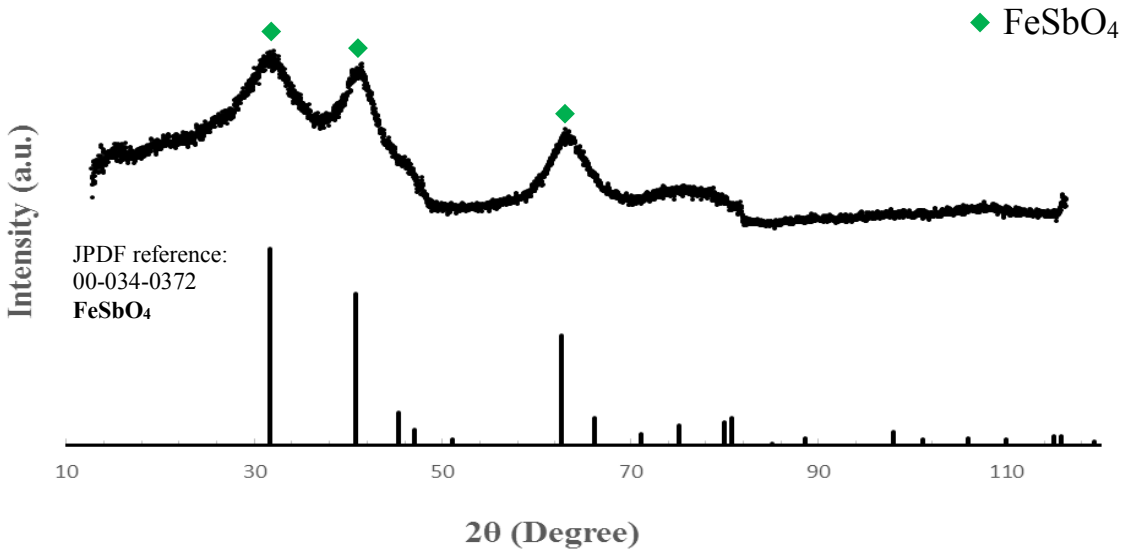

Figure 4.10 – *X–ray powder diffraction pattern of the poorly crystalline precipitate obtained at pH 5.3 compared to reference tripuhyite pattern ($FeSbO_4$) – JPDF (00-034-0372).*

Figure 4.12 gives the precipitate particle size distribution (PSD) that is seen to be bimodal[13]. The bulk of the material (coarse fraction) had ~ 6 μm average size while the minor fine fraction had ~ 0.5 μm average size. It must be noted that the PSD measurements refer to dried precipitates that were broken down by mortar and pestle as well as by an ultrasonic horn (1 hr) before being analyzed. As it can be evaluated by examining the SEM images in Figure 4.13, the dried precipitate particles were heavily agglomerated. Upon performing BET analysis, the precipitate was determined to have a very high specific surface area (161.5 $m^2 \cdot g^{-1}$) from which the mean spherical primary particle size was calculated to be in the nanometer–scale (6.4 nm)[14]. The very fine size of the as–prepared precipitate can thus explain its rather poor filterability. On the basis of these observations, it appears that precipitation took place predominantly via homogeneous nucleation resulting in nano–scale primary particles that formed aggregates, which eventually became large (highly porous) agglomerates upon drying.

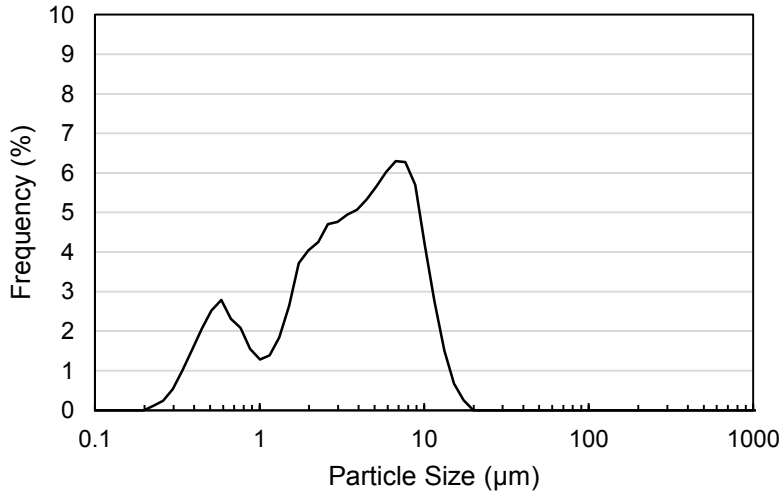

Figure 4.11 – *Particle size distribution of the precipitate.*

[13] Prior to particle size distribution analysis, the precipitate powder was washed and dried, which may have induced particle agglomeration.

[14] Particle size (nm) = 6000/(ρ·S); ρ = density (5.82 $g \cdot cm^{-3}$ for tripuhyite), S = BET surface area ($m^2 \cdot g^{-1}$).

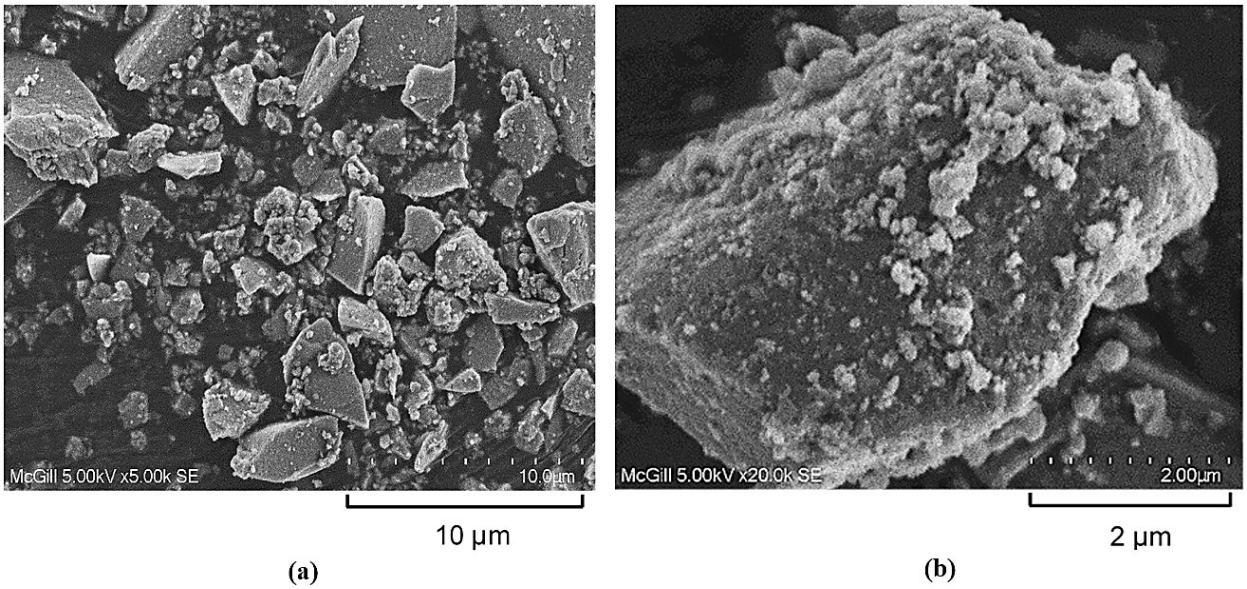

Figure 4.12 – *SEM micrographs of the washed and dried precipitate, (a) 10µm scale, (b) 2µm scale.*

4.4 Hydrothermally treated precipitate

The washed and dried precipitate was hydrothermally treated in a pressure bomb at 200 ^{o}C for 12 hrs. The solution pH was adjusted to 1 with sulfuric acid in order to facilitate dissolution of any amorphous material and recrystallization into higher crystalline tripuhyite.

The hydrothermal product was pressure filtered and washed before being subjected to subsequent stability tests. Figure 4.14 displays the filtrate concentrations as a function of wash cycles, with most iron, antimony, and sodium removed, suggesting minimal entrainment of impurities within the powder. By comparison to the as–prepared precipitate (Figure 4.10) that yielded ~ 10 mg·L^{-1} Sb and Na in the wash water, the hydrothermally treated precipitate yielded no more than 0.1 mg·L^{-1}, a 100–fold reduction. This reduction provides a powerful early signal of the effectiveness of hydrothermal treatment in stabilizing Sb in the precipitate via some recrystallization mechanism.

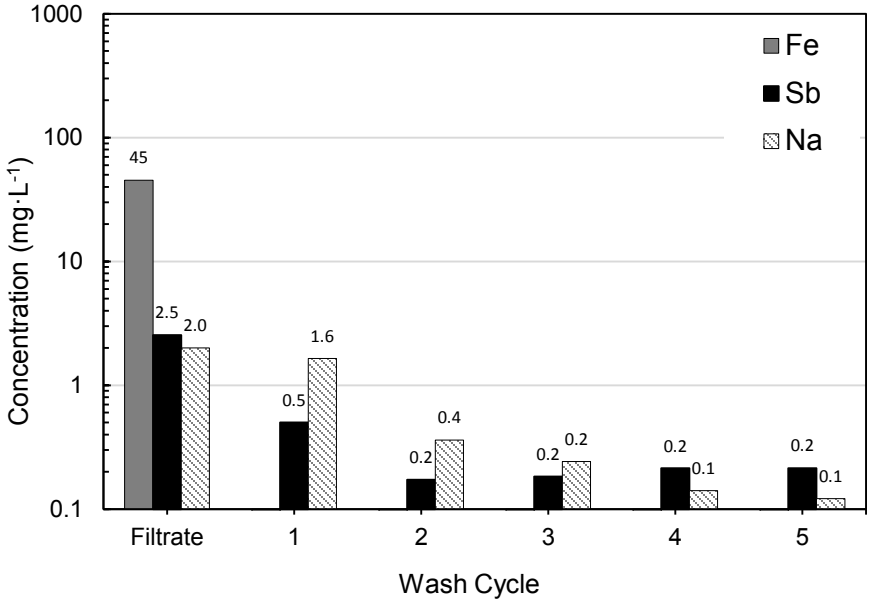

Figure 4.13 – *Iron, antimony and sodium filtrate concentrations at different wash cycles.*

X–ray powder diffraction analysis indeed provided direct confirmation of the positive hydrothermal treatment effect on the crystallinity of the tripuhyite precipitate, as shown in Figure 4.15. There are clearly stronger and sharper peaks with significant decrease in the broad background when compared to the untreated precipitate. By comparing the width at half–height of the main peaks (32.2, 41.3, 63.5 °2θ angles) with the assistance of TOPAZ (v4.2) software[15], the primary particle size was found to increase from 1.8 to 3.3 nm. This primary crystallite growth was also reflected in the BET specific surface area that was dropped from 161.5 $m^2 \cdot g^{-1}$ to 130.5 $m^2 \cdot g^{-1}$ after treatment, yielding a BET calculated primary particle size of 7.9 nm (drop from 6.4 nm). Both calculations of particle size (Scherrer and BET method), although estimations, are in agreement, indicating particle size increase as a result of hydrothermal treatment.

[15] TOPAZ uses Scherrer's equation to estimate crystallite particle size; particle size (nm) = $0.9\lambda/(\beta \cdot \cos\theta)$; λ is the X–ray wavelength (nm), β is the width at half height ($\Delta(2\theta)$), θ is the diffraction angle.

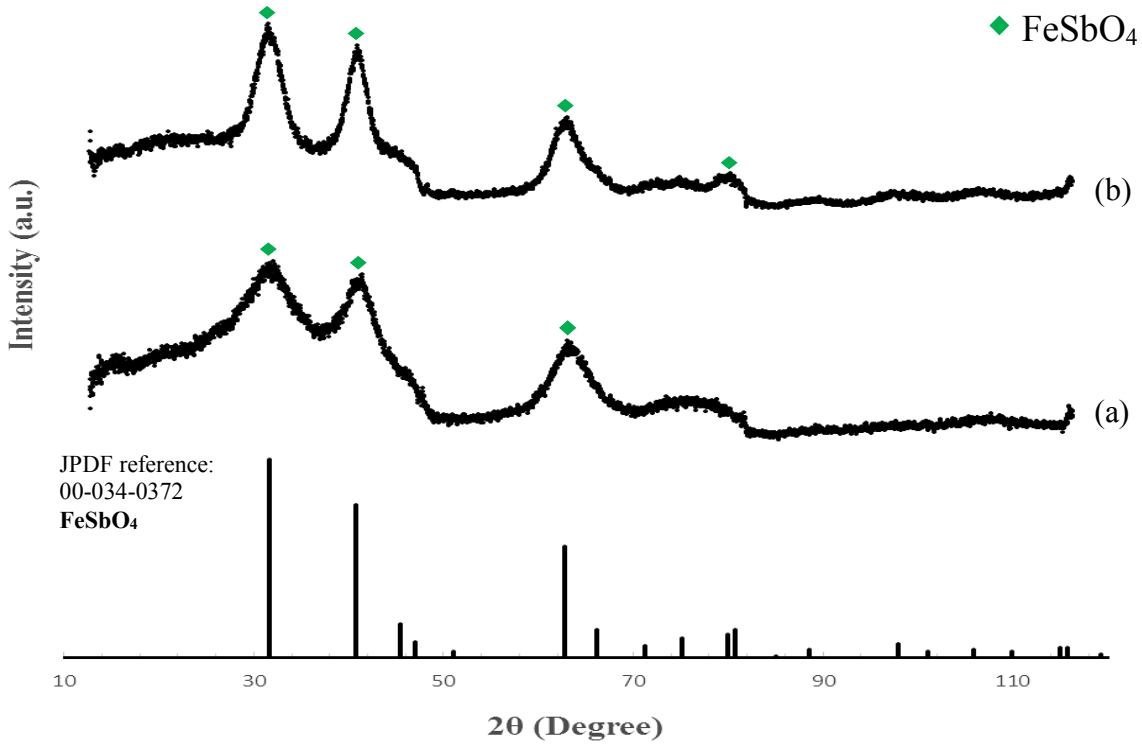

Figure 4.14 – *X–Ray powder diffraction patterns; (a) Untreated precipitate, (b) Hydrothermally treated precipitate, and reference tripuhyite pattern ($FeSbO_4$) – JPDF (00-034-0372).*

In addition to primary crystallite, secondary particle size was also increased upon hydrothermal treatment as reflected in the PSD results reported in Figure 4.16 and also in the SEM micrographs presented in Figure 4.17.

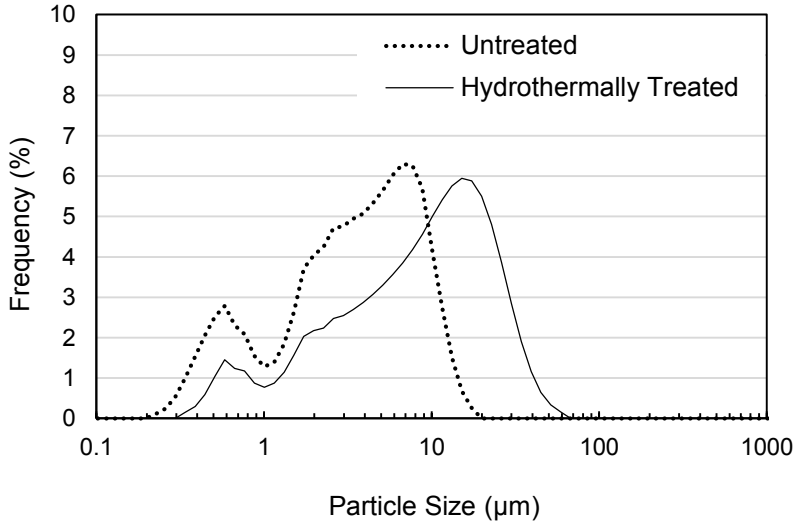

Figure 4.15 – *Particle size distribution of the precipitate before and after hydrothermal treatment.*

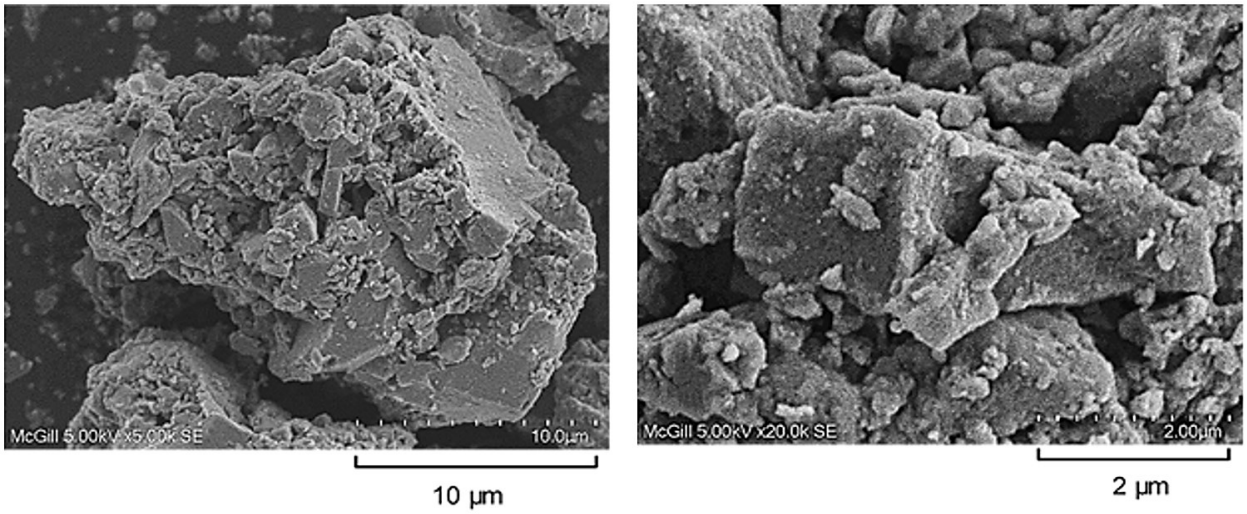

(a) **(b)**

Figure 4.16 – *SEM micrographs of the hydrothermally treated precipitate, (a) 10µm scale, (b) 2µm scale.*

4.5 Calcined precipitate

The as–prepared precipitate was also subjected to thermal treatment by calcination to promote the crystallization of tripuhyite. Following calcination at 950 °C for 12 hrs, the resultant product was subjected to wash cycles. Wash waters contained near consistent sodium and antimony concentrations in the 0.5 – 2 $mg \cdot L^{-1}$ range, respectively, Figure 4.18(a)[16], whereas iron was not detected after cycle 1.

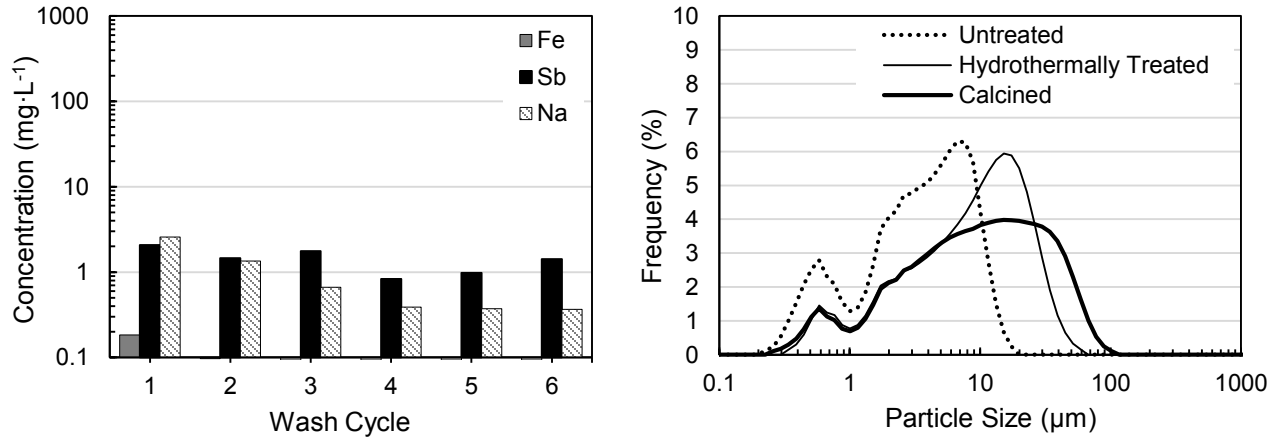

(a) **(b)**

Figure 4.17 – *(a) Iron, antimony and sodium filtrate concentrations at different wash cycles, (b) particle size distribution of the calcined precipitate.*

[16] A detailed version of Figure 4.18(a) giving numerical values for the ion concentrations can be found in the Appendix.

X–ray powder diffraction analysis, Figure 4.19, found calcination of the precipitate to yield highly crystalline $FeSbO_4$ but with a secondary $NaSbO_3$ phase as impurity. The presence of the impurity proved problematic in the subsequent stability tests discussed in the next section. The origin of the impurity phase was traced to the fact that the precipitate had not been completely washed of the sodium contaminant prior to calcination. As such, upon water evaporation the soluble sodium antimonate salt apparently crystallized out as $NaSb(OH)_6$ after which calcination converted to $NaSbO_3$, which is the thermal decomposition product referenced to be thermally stable up to 1100 ºC (Olmi and Sabelli, 1994). Nevertheless calcination was effective in producing highly crystalline $FeSbO_4$ with primary crystallite size of 18.4 nm, according to the Scherrer method (TOPAZ v4.2) or 31.6 nm according to the BET method, which determined its specific surface area to have reduced to 32.6 $m^2 \cdot g^{-1}$. In other words, significant crystallite growth was induced at the high temperature of calcination (950 °C).

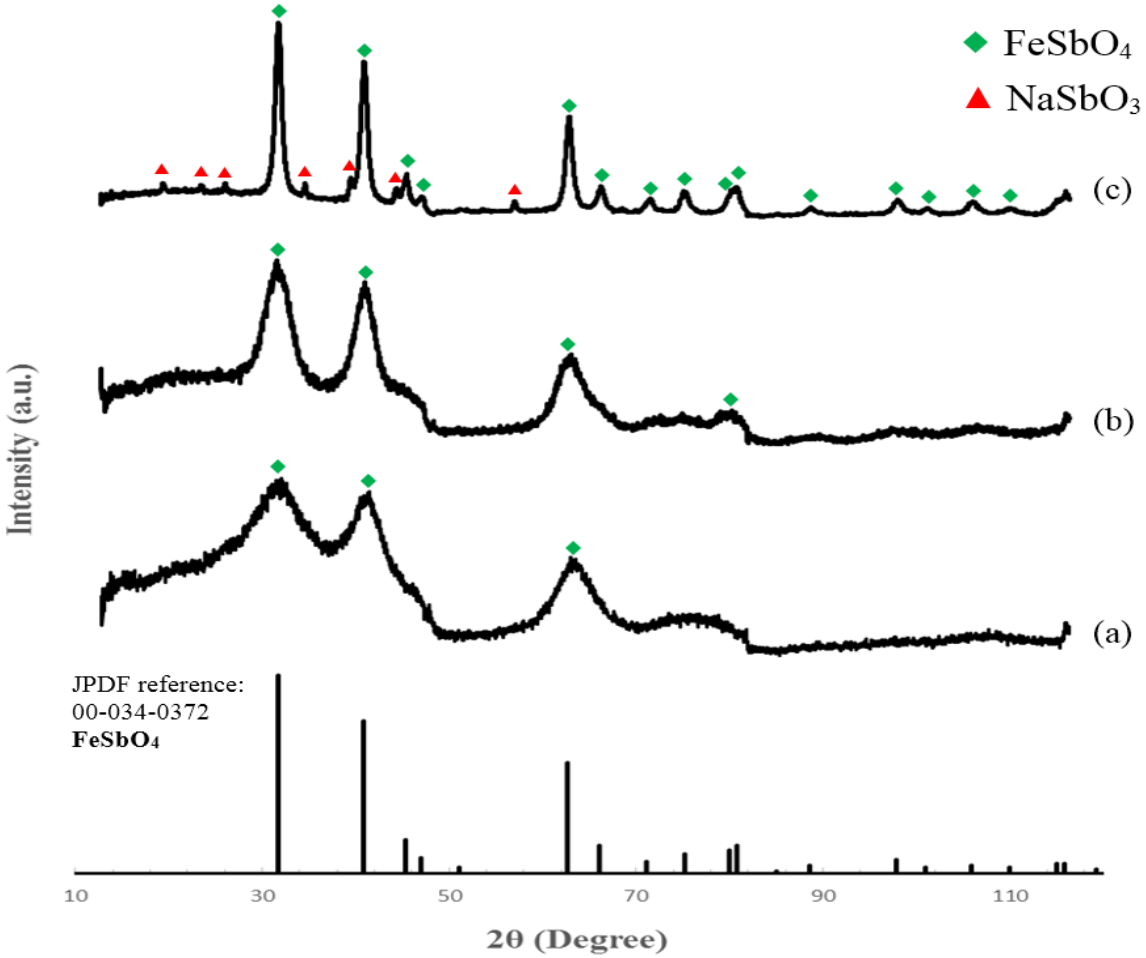

Figure 4.18 – *X–ray powder diffraction patterns; (a) Untreated precipitate, (b) Hydrothermally treated precipitate, (c) Calcined precipitate, "◆" reference tripuhyite pattern ($FeSbO_4$) – JPDF (00-034-0372), "▲" reference brizziite pattern ($NaSbO_3$) – JPDF (00-042-0223).*

Particle size analysis, Figure 4.18(b), and SEM imaging, Figure 4.20(a), provided further evidence of significant crystal size increase as compared to the untreated and hydrothermally treated precipitates. For example, the displayed secondary particle in Figure 4.20(a) is at least 100 μm in size. Upon collecting higher magnification SEM images, an interesting feature was observed with new smaller crystals protruding from the large tripuhyite ($FeSbO_4$) mineral surface as shown in Figure 4.20(b). By performing energy dispersive X–ray spectroscopy analysis (EDS) as shown in Figure 4.21, the small protruding crystals were identified to be $NaSbO_3$ and in agreement with the XRD findings (Figure 4.19). The concentrated sodium regions coincide with $NaSbO_3$, which was further supported by the hexagonal shape of the small crystals, characteristic of $NaSbO_3$ as the SEM images in Figure 4.22 clearly show.

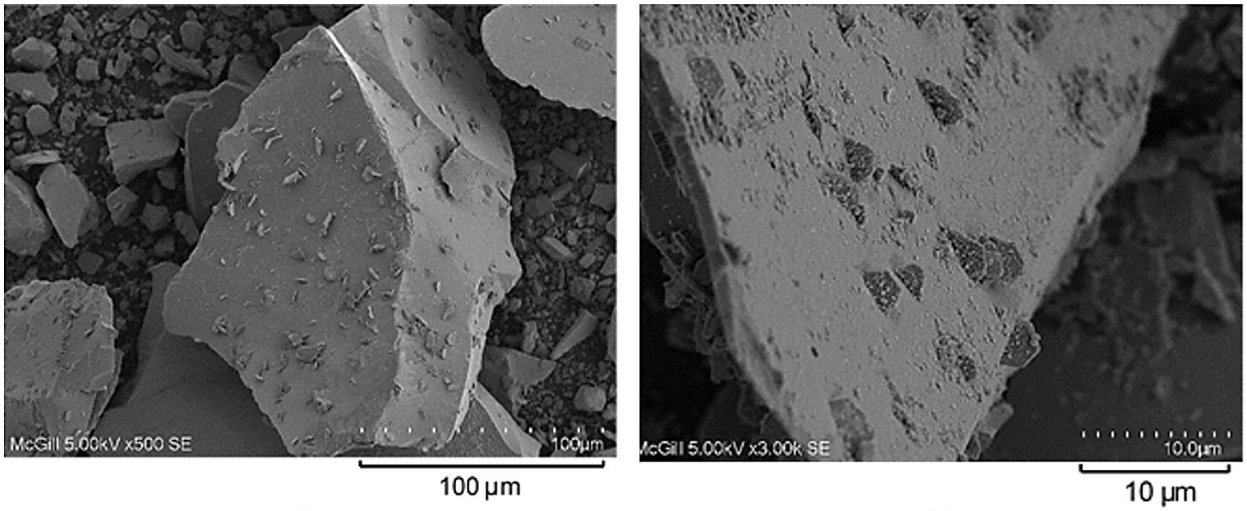

Figure 4.19 – *SEM micrographs of the calcined precipitate, (a) 100μm scale, (b) 10μm scale.*

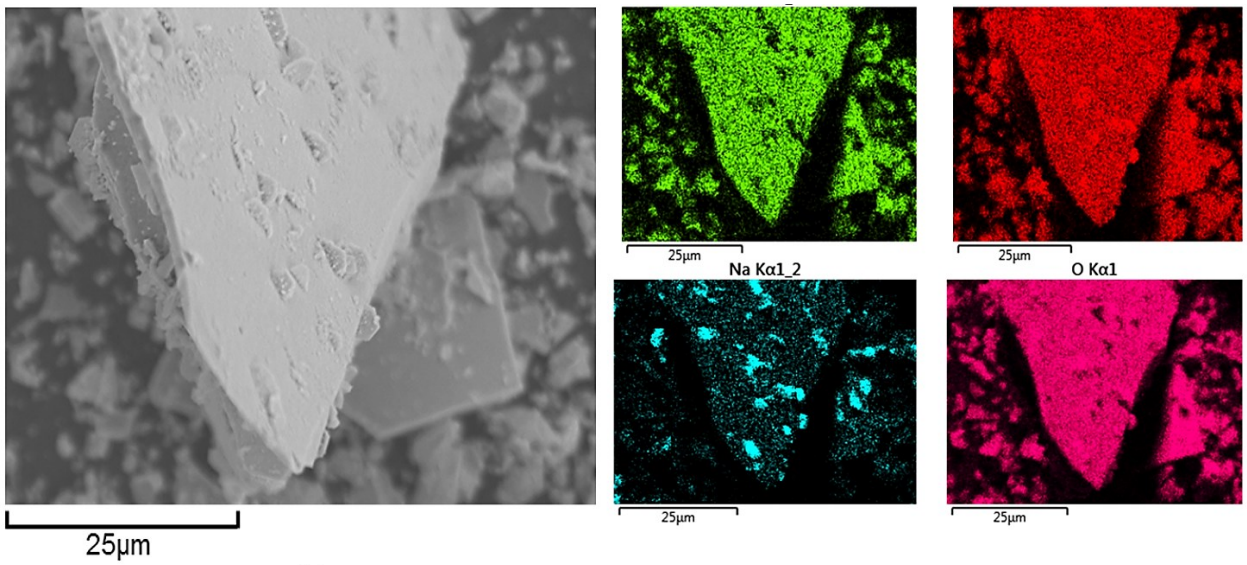

(a) **(b)**

Figure 4.20 – *(a) SEM micrograph and; (b) iron, antimony, sodium, and oxygen energy dispersive X–ray spectroscopy (EDS) maps of the calcined precipitate surface.*

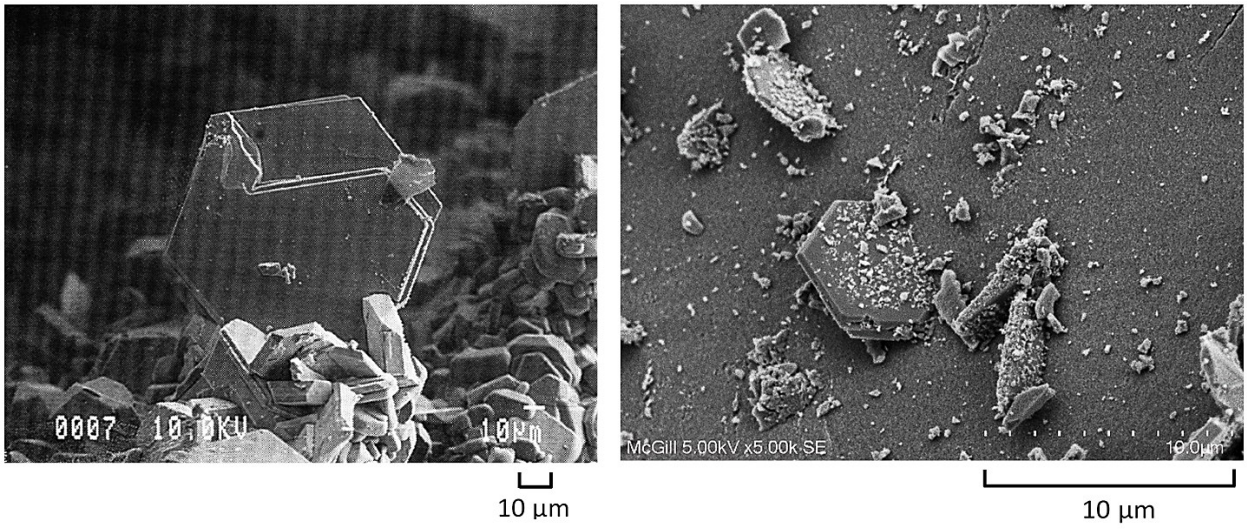

(a) **(b)**

Figure 4.21 – *SEM micrographs of brizziite ($NaSbO_3$), (a) reproduced from Olmi and Sabelli (1994), (b) present study.*

4.6 Synthesis of reference tripuhyite ($FeSbO_4$)

Crystalline tripuhyite reference material was synthesized using a modification of the high temperature solid–state method previously reported by Martinelli et al. (2002), in which reagent grade goethite (FeOOH) and antimony pentoxide (Sb_2O_5) were substituted for hematite (Fe_2O_3) and antimony trioxide (Sb_2O_3), respectively. The flowchart of the preparation protocol is shown in Figure 4.23. Initial tests employing Fe_2O_3 and Sb_2O_3 resulted in incomplete reaction with mixed

phase product, hence the substitution with FeOOH and Sb_2O_5. Both FeOOH and Sb_2O_5 were in the form of powders and used in equimolar amounts (Fe/Sb of one). The powders were calcined at 950 ^oC for 12 hrs.

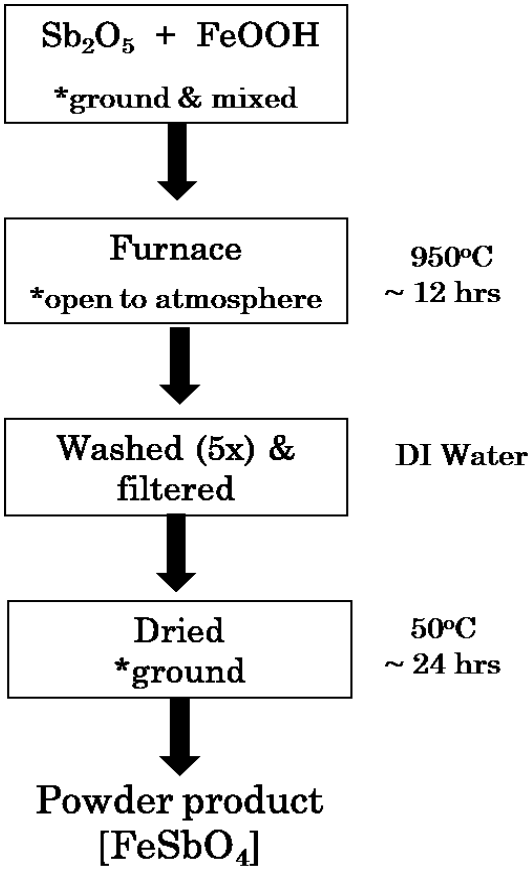

Figure 4.22 – *Flowchart of solid–state synthesis of reference tripuhyite material.*

X–ray powder diffraction analysis, Figure 4.24, confirmed the synthesized material to be of high quality tripuhyite in terms of purity and crystallinity, evident by the sharpness and complete matching of all peaks. As such, the synthetic tripuhyite produced from FeOOH and Sb_2O_5 made for an excellent reference material in the subsequent stability tests.

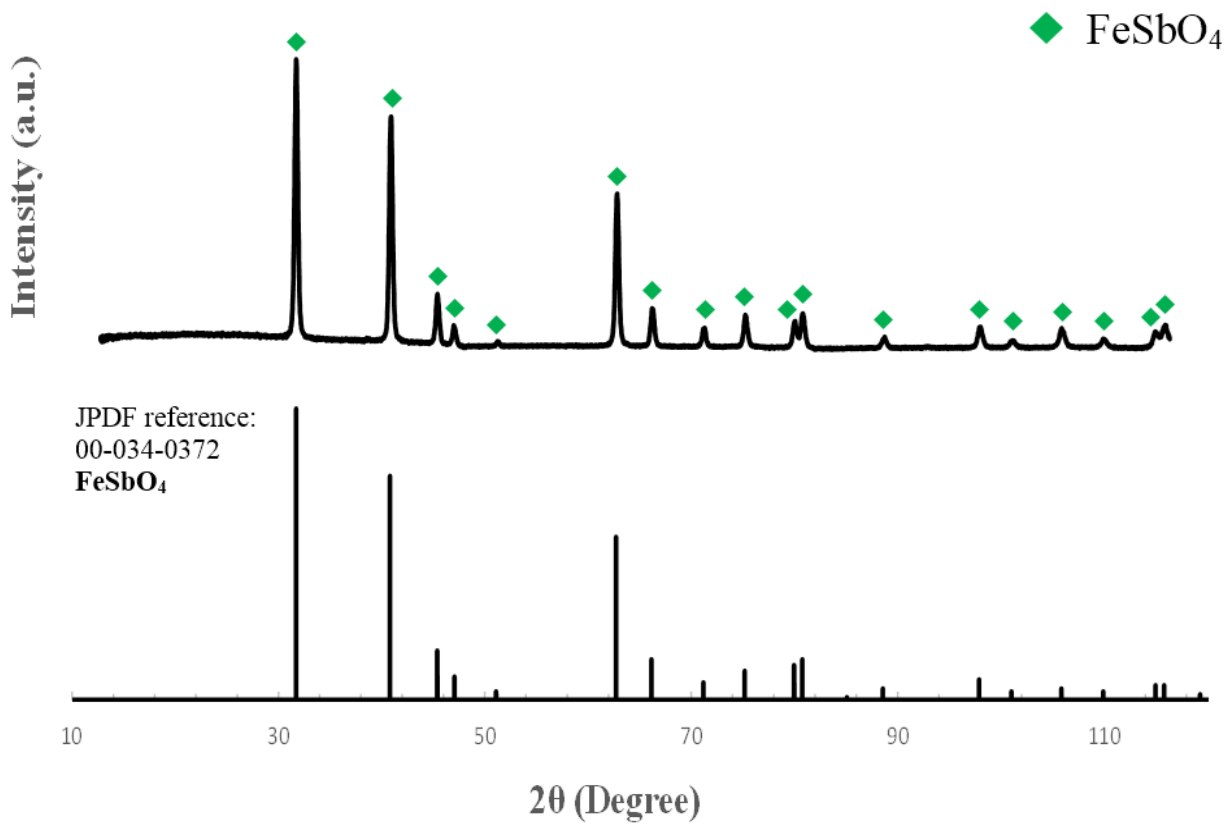

Figure 4.23 – X–ray powder diffraction pattern of tripuhyite ($FeSbO_4$) produced by solid–state synthesis compared to reference tripuhyite pattern ($FeSbO_4$) – JPDF (00-034-0372).

SEM analysis, Figure 4.25, revealed the synthetic tripuhyite to be in the form of large spherical agglomerates in the order of 50 μm in size; after ultra–sonication in isopropanol the agglomerate size was reduced below 20 μm (full particle size distribution data can be found in the Appendix). Individual primary crystallites appeared to be in the 100 – 200 nm size range, Figure 4.25(d).

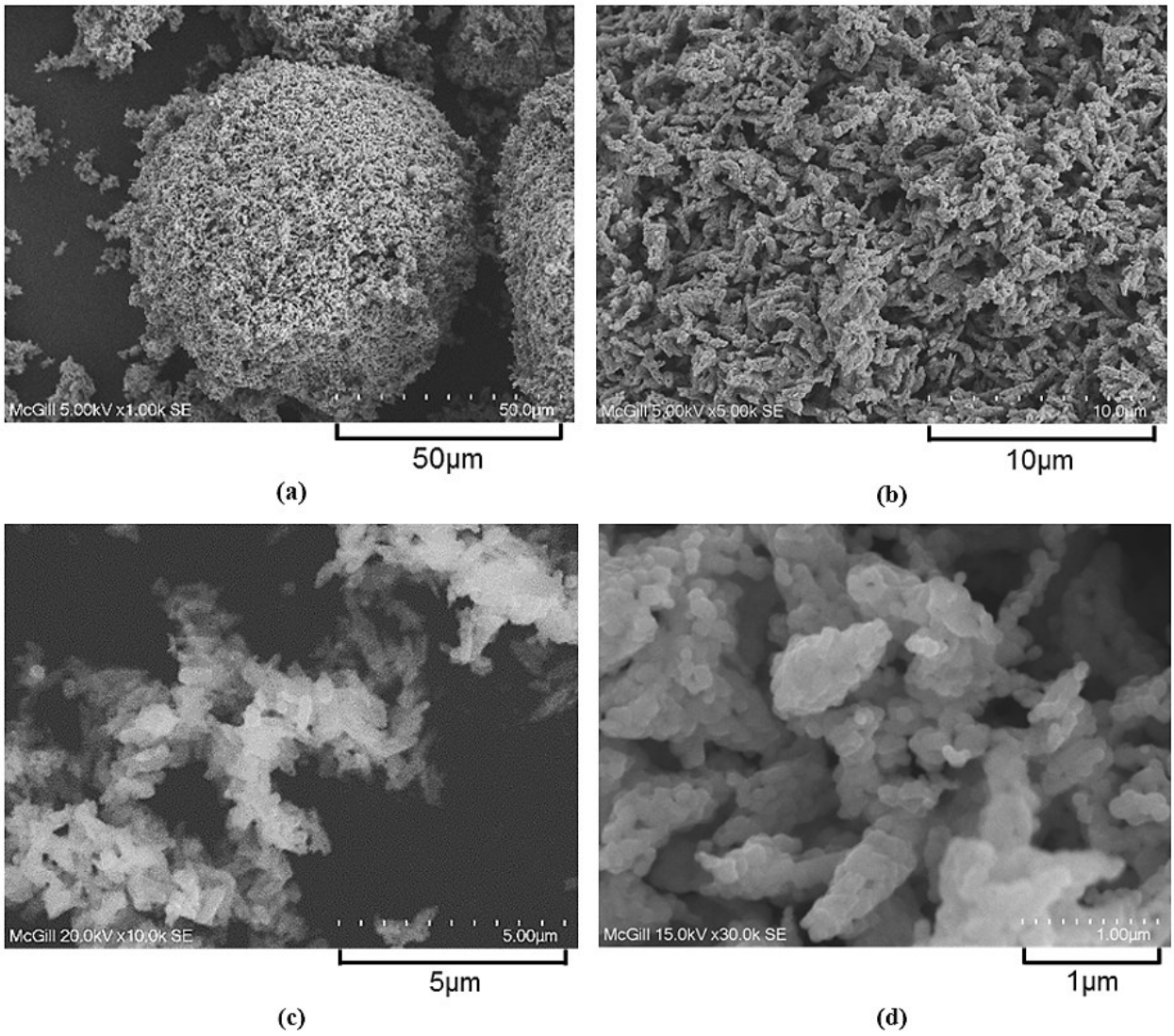

Figure 4.24 – *SEM micrographs of synthetic tripuhyite ($FeSbO_4$), (a) 50µm scale, (b) 10µm scale, (c) 5µm scale, and (d) 1µm scale.*

4.7 Stability

4.7.1 Leachability results

The washed precipitates; untreated, hydrothermally treated, calcined, as well as the reference tripuhyite were subjected to stability testing. Powder samples of each material, 1g, were placed in 100 mL of deionized water with the solution pH kept constant at 6, 7, and 8. In addition to pH−controlled stability tests for each material, a separate test was carried out without pH adjustment to assess its stability at its natural equilibrium pH.

Figure 4.26 displays the stability test results for all four materials; it was determined that all material/solution systems had reached pseudo−equilibrium at most after 15 days of equilibration. Each

sub–plot in Figure 4.26 depicts the pH effect on the leachability of each respective material, whereas Figure 4.27 and the sub–plots therein compare the leachability of all materials at a specific pH. Finally in Figure 27(d), the evolution of pH in the case of the pH–drift series for each material is given. According to the latter data, pseudo–equilibrium was reached in 5 days (except for the calcined product, which was about 9 days), i.e. at shorter time than the tests in which pH was adjusted. As it can be seen the pH dropped in general modestly during leachability evaluation to pH between 6 and 7.8 except the hydrothermally treated material that saw the drift pH to drop considerably down to 3.5. The general leachability reaction that involves proton release is given below. In the reaction, incongruent dissolution is assumed with ferric iron undergoing hydrolysis due to relatively elevated pH in analogy to the scorodite system (Bluteau and Demopoulos, 2007):

$$FeSbO_4 + 5H_2O \rightarrow Sb(OH)_6^- + Fe(OH)_3 + H^+$$

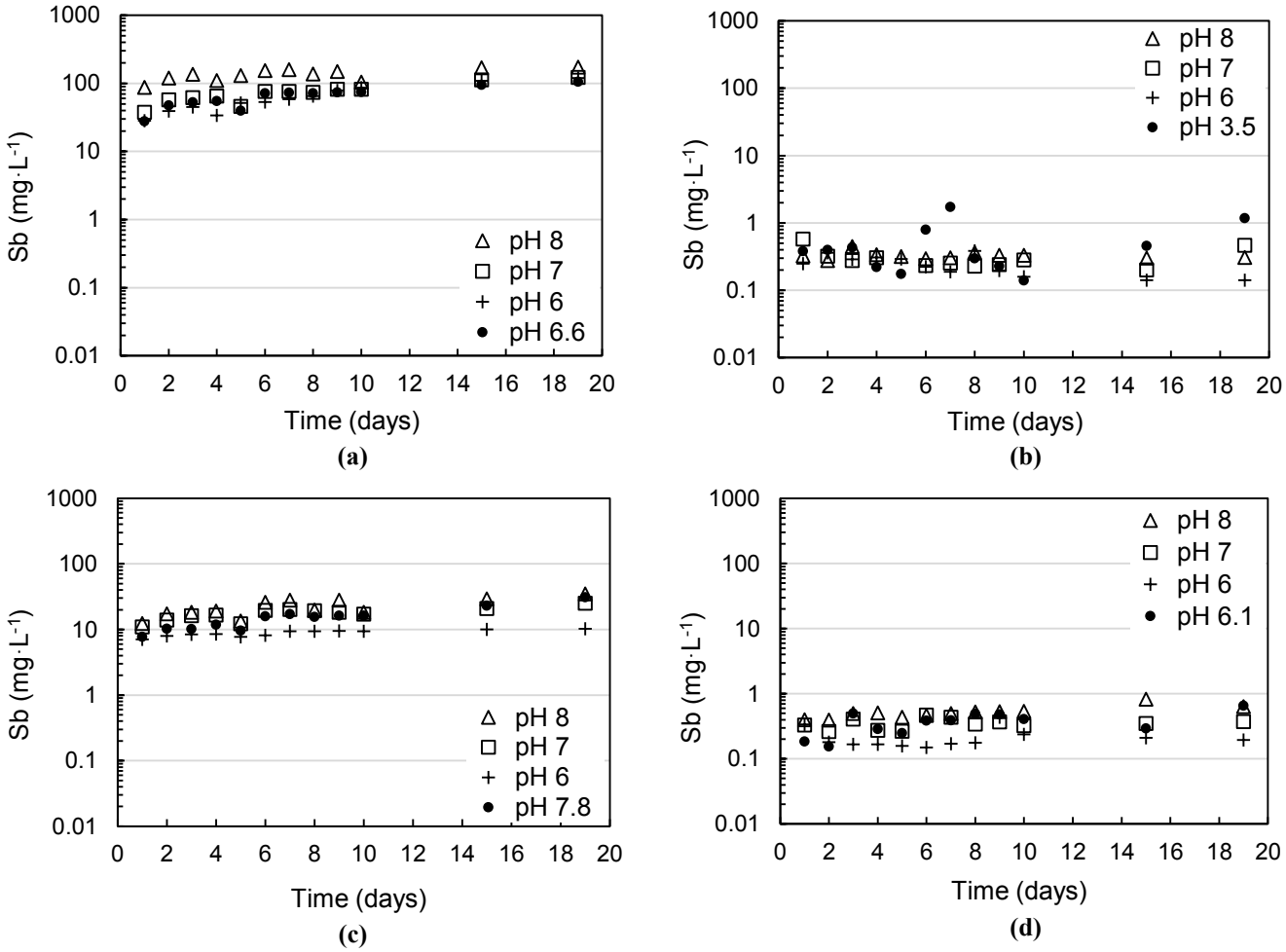

Figure 4.25 – *Antimony concentration (mg·L^{-1}) as a function of time, where "•" denotes the final unadjusted pH of the solution; (a) Untreated precipitate; (b) Hydrothermally treated precipitate; (c) Calcined precipitate, (d) Reference tripuhyite ($FeSbO_4$).*

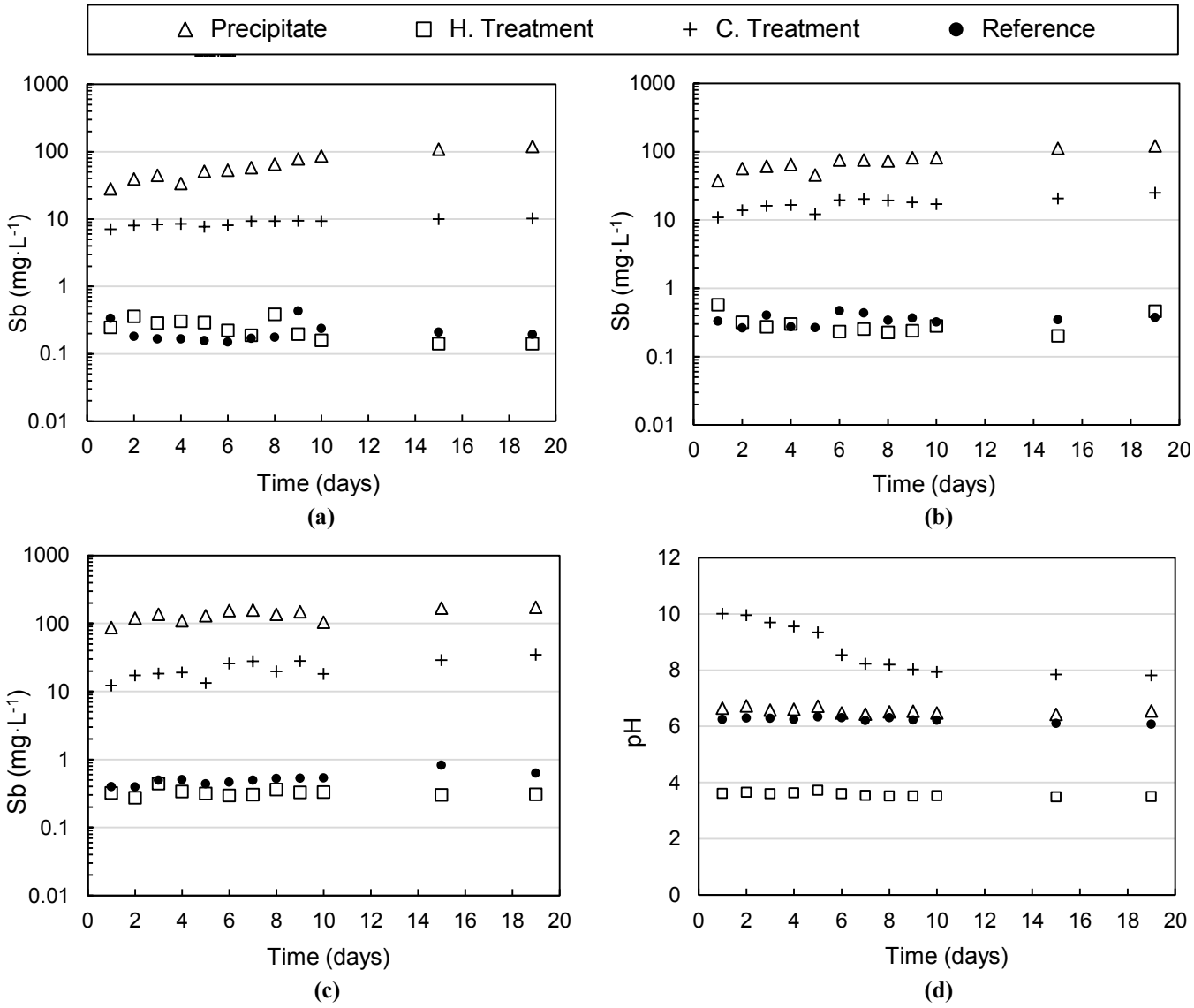

Figure 4.26 – *Antimony concentration (mg·L^{-1}) of all precipitates as a function of time at specific pH; (a) pH = 6; (b) pH = 7; (c) pH = 8; and (d) pH evolution as a function of time.*

For the untreated precipitate, Figure 4.26(a), the final (pseudo–equilibrium) antimony concentration was significant, namely 119, 105, 122, and 172 mg·L^{-1} at pH 6, 6.6, 7, and 8 respectively. The significant amounts of antimony release, regardless of solution pH, highlights the fact that the untreated precipitate was in the form of poorly crystalline and nano–sized tripuhyite. By contrast the pseudo–equilibrium leachability data for the hydrothermally treated precipitate, Figure 4.26(b), and reference tripuhyite, Figure 4.26(d) were in the order of 0.5 mg·L^{-1} Sb, i.e. more than 200 times lower than the as–prepared precipitate. These results demonstrate that hydrothermal treatment was very effective in stabilizing antimony in the Fe(III)–Sb(V) form. A noteworthy result is the fact that the antimony release from the hydrothermally treated

precipitate was comparable to that of the reference tripuhyite, Figure 4.26(d), despite the fact that according to XRD results, the latter was significantly more crystalline. It is postulated that the acidic solution (< pH 1) under the hydrothermal conditions (200 ^{o}C) prevailing in the autoclave favours the dissolution of the ultrafine (nano) and less crystalline particles, which upon recrystallization, yielded coarser and better crystalline particles. The recrystallization was believed to follow the mechanism of Ostwald ripening, where smaller particles slowly dissolve and become nucleation sites for crystal growth, resulting in coarser and more stable crystalline particles (Ratke and Voorhees, 2002, and Brantley et al., 2008). These stability results agree with the general trend that as crystallinity and crystallite size increase the solubility of the compound decreases as also reported in the case of scorodite (Krause and Ettel, 1989; Langmuir et al., 2006; Le Berre et al., 2007; Demopoulos, 2009).

The calcined precipitate, Figure 4.26(c), was initially expected to have the best performance out of the three precipitates in terms of stability as it had the highest degree of crystallinity. Instead, it was found to release 10 – 50 times more Sb than the hydrothermally treated precipitate, namely 10, 25, 31, and 35 mg·L^{-1} at pH 6, 7, 7.8, and 8 respectively. The unexpected higher Sb release levels were attributed to the presence of the secondary phase brizziite, $NaSbO_3$, already identified in the earlier characterization section. Stability and solubility data on brizziite is scarce in literature mainly due to its relatively recent discovery (mid–1990s) and rare occurrence in the natural environment (Olmi and Sabelli, 1994; Roper et al., 2012). Studies that use synthetic brizziite also do not address its thermodynamic stability. The origin of $NaSbO_3$ stems from the fact that the precipitate had not been completely freed of sodium contamination after the wash cycles prior to calcination. The treated precipitates, hydrothermal and calcination products, were also subjected to washing prior to stability tests to ensure the removal co–precipitated or adsorbed impurities. However in the case of calcined precipitate, even after 6 cycles of washing, antimony and sodium were still present in the filtrate, Figure 4.18(a). Continued washing was deemed impractical as there was a minimal decline in antimony and sodium concentrations in the filtrate, however, in retrospect, acid wash cycles may have been more effective in removing impurities as well as dissolving the $NaSbO_3$ crystals as indeed it happened with the acidic water used during hydrothermal treatment. The issue of antimony release is discussed further later in this chapter by making reference to some theoretical calculations.

Figure 4.26(d) demonstrates the stability of the reference crystalline tripuhyite ($FeSbO_4$). In all solutions including the unadjusted–pH, the antimony concentration was always below 1 $mg \cdot L^{-1}$. The slight antimony release is the result of a very stable crystal structure hence tripuhyite proves very promising phase to immobilize antimony in aqueous solutions. Recent thermodynamic studies have alluded to tripuhyite, as well as schafarzikite ($FeSb_2O_4$), as being "ultimate sinks" for antimony in the environment, and the stability data collected in this work seems to support this statement (Diemar et al., 2009; Leverett et al., 2012; Roper et al., 2012).

All pseudo–equilibrium solubility data (precipitates and reference mineral) were also compared based on pH to determine the effect of pH on antimony stability, depicted in Figure 4.27, where one material may be more stable at a certain pH than another, however, less stable at a different pH. In all pH conditions (pH 6, 7, and 8), lowest antimony release was observed from the reference mineral as well as the hydrothermally treated precipitate; both materials demonstrated similar behaviour. The calcined precipitate released much more antimony with respect to the two previously mentioned materials, typically one order of magnitude more, this being the result of the presence of the $NaSbO_3$ impurity phase. The precipitate without treatment proved to have the poorest stability at all pH; it consistently released significant amounts of antimony, 2 orders of magnitude more than the reference material and hydrothermally treated precipitate. It becomes evident that although pH does play a role, where increasing pH results in increased antimony release (within the range tested), material stability was found to be primarily a function of crystallinity rather than pH within the range (6 – 8) investigated. The exception to this statement is the calcined precipitate, as iterated previously, the instability was the result of the secondary phase impurity, which may be removed through acid wash treatments prior to stability testing.

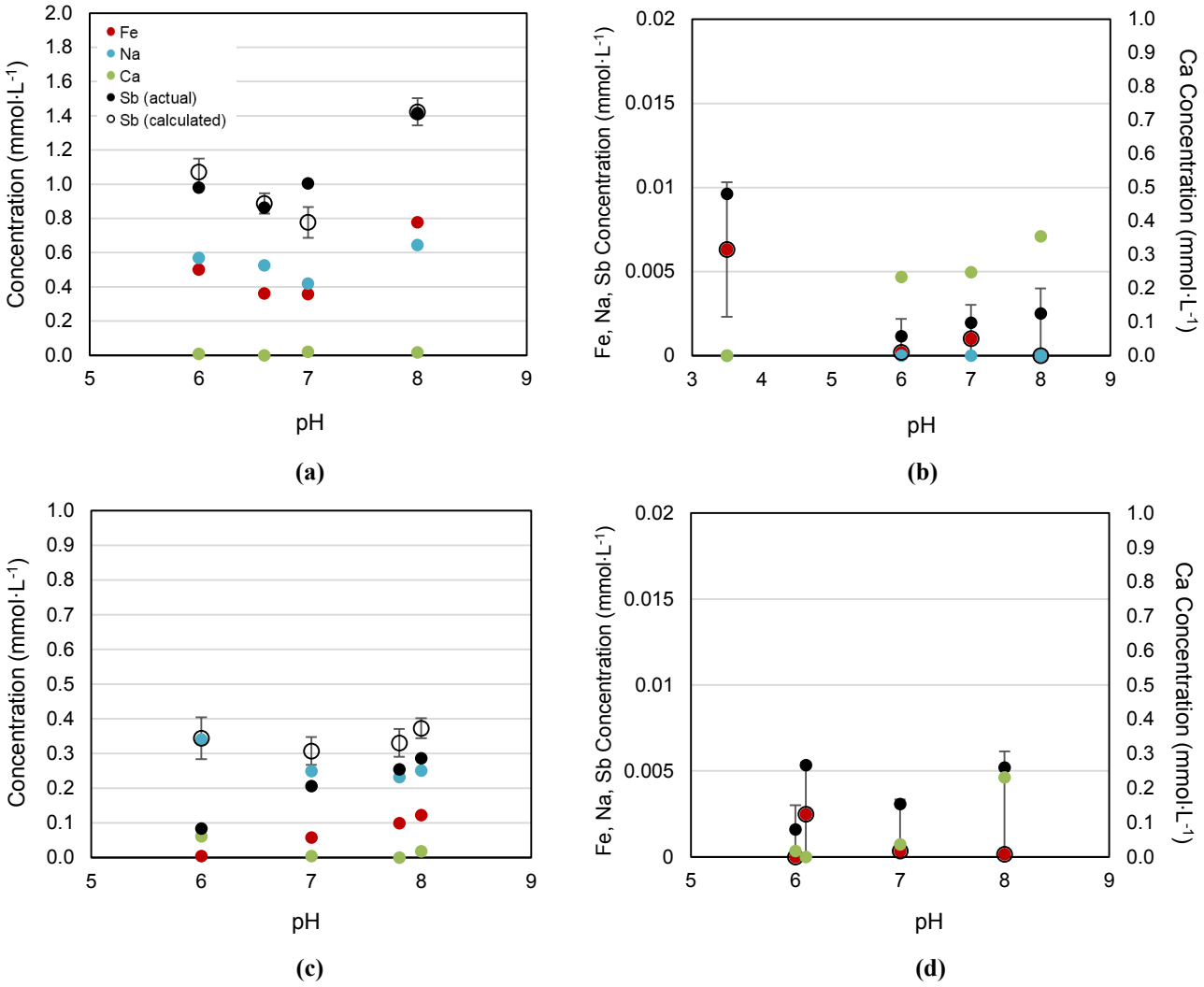

Figure 4.27 – *Pseudo–equilibrium iron, sodium, calcium, and antimony (actual and stoichiometrically calculated) concentrations (mmol·L^{-1}) as function of pH: (a) Untreated precipitate; (b) Hydrothermally treated precipitate; (c) Calcined precipitate; (d) Reference tripuhyite ($FeSbO_4$), error bars represent 2 standard deviations.*

4.7.2 Discussion

From the pseudo–equilibrium concentrations of iron and sodium for all materials, a theoretical antimony equilibrium concentration was calculated based on equimolar Sb/Fe[17] and Sb/Na ratios. This approach gave good agreement between actual and calculated Sb concentrations in the case of untreated and calcined precipitates (Figure 4.28 (a) and (c)), the two precipitates that were contaminated with $NaSbO_3$.

[17] It must be clarified that any iron released during the leachability test is expected to hydrolyze into ferric hydroxide (incongruent dissolution). The finding of iron in solution (data in Figure 4.28) most likely represents colloidal hydroxides that due to their nano–size have passed the filter that was used (200 nm pore size). Similar observations were made by Bluteau and Demopoulos (2007) during the scorodite solubility study.

For the calcined precipitate, Figure 4.28(c), the observed and calculated antimony concentrations were closer in agreement where there was minimal calcium present (7, 7.8, and 8). At pH 6, the antimony concentration was expected to be much higher based on the sodium concentration, in spite of this, the true concentration deviated the most from the calculated, coinciding with the highest calcium concentration[18]. This may imply the formation of a phase like roméite, $Ca_2Sb_2O_7$, that is known to be very stable especially in alkaline waters (Diemar et al., 2009; Roper et al., 2012; Okkenhaug et al., 2013). To verify this possibility, the post–stability test precipitates were analyzed by X–ray powder diffraction (as well as with the OLI solution thermodynamics software (OLI Stream Analyzer v3.2.4))[19] to determine if new phases, especially roméite had formed, however, this proved inconclusive with the results being similar with the starting solids (Figure 4.19(c)). This may well reflect the fact that if any new phase was present, its trace amount would have made it undetectable by XRD and not to mention the likely poorly crystalline character as it was likely present in its hydrated form: $Ca[Sb(OH)_6]_2$.

The hydrothermally treated precipitate, Figure 4.28(b), actual and calculated antimony concentrations were within the error of the calculation, however, due to very low concentrations (< 1 $mg \cdot L^{-1}$) and high degree of error, it is difficult to conclude with confidence whether the two are in good agreement. Similarly for the reference tripuhyite material, Figure 4.28(d) demonstrates the differences in the actual and calculated antimony concentrations, however, due to very low concentrations and higher relative error in the calculations, there does not appear to be any observable trend. The actual pseudo–equilibrium antimony concentrations at pH 5, 6, 7, 8, and 9 were 0.064, 0.194, 0.374, 0.632, and 0.644 $mg \cdot L^{-1}$, respectively, where pH 5 and 9 data was not shown previously to reduce confusion. The important finding from the solubility data of the reference mineral is that at pH 5, the antimony concentration (~ 60 $\mu g \cdot L^{-1}$) was in the range of that cited by Selim et al. (2012).

A discussion of the solubilities of some key compounds based on literature information, which can potentially be linked to the measured antimony concentration after dissolution, follows. The solubility of synthetic roméite, $Ca_2Sb_2O_7$, as studied by Diemar et al. (2009) was calculated

[18] As a reminder, lime had been used to adjust the pH during the leachability tests.

[19] The use of OLI was not successful as its database does not include thermodynamic data for tripuhyite, roméite and other relevant antimony compounds and undertaking an extensive update of its database was beyond the scope of the present thesis.

to correspond to an antimony concentration of ~ 40 $\mu g \cdot L^{-1}$, whereas its "amorphous equivalent", typically referenced as the hydrated roméite – $Ca[Sb(OH)_6]_2$, was studied by Johnson et al. (2005) was found to release ~ 16 $mg \cdot L^{-1}$ antimony. It is noteworthy that the two solubilities differ largely, about 3 orders in magnitude, which, as explained by Cornelis et al. (2011) is most likely the result of mineral crystallinity, Sb:Ca ratio, and pH at which the minerals were synthesized. Given that the stability tests were carried out at room temperature, it may be deduced that if Ca–Sb precipitates had formed, they would have been the poorly crystalline/amorphous variety ($Ca[Sb(OH)_6]_2$) and not the crystalline roméite ($Ca_2Sb_2O_7$). Therefore, other than the case of as–prepared precipitate and the calcined precipitate that recorded "solubilities" in the order of tens of $mg \cdot L^{-1}$, it is derived that at all likelihood Ca played no role in the attainment of very low solubility by the reference and the hydrothermal materials.

In the case of tripuhyite solubility data, Selim et al. (2012) reflect upon the work of other authors and cite the antimony concentration to be a few $\mu g \cdot L^{-1}$ (in laboratory conditions). Since variation in the degree of crystallinity and crystallite size can influence solubility, then the data obtained for the hydrothermal and reference materials can be attributed indeed to this compound as the one controlling Sb release. Lastly, the solubility of mopungite, $NaSb(OH)_6$, is accepted as ~ 390 $mg \cdot L^{-1}$ antimony (Blandamer et al., 1974; and Selim et al., 2012). From the solubility data[20], it is reasonable to state the formation of mopungite is highly unlikely in the presence of iron.

[20] Brizziite ($NaSbO_3$) solubility data was not available in the literature, thus its formation was not speculated upon.

Chapter 5 – Synopsis

5.1 Global conclusions

Antimony removal as poorly crystalline tripuhyite ($FeSbO_4$) via a novel supersaturation control scheme involving slow co–oxidation of Fe(II) and Sb(III) (via drop–wise addition of H_2O_2) was demonstrated. Preliminary precipitation tests (pH 1.5 – 5.3) at 95 °C showed sub–stoichiometric removal of Fe(II) (~ 80%) but complete precipitation of Sb(III). The Sb/Fe molar ratio of the precipitate decreased with increasing pH, reaching 1.14 at pH 5.3, which was found to be the closest to the stoichiometric ratio (Sb/Fe = 1) and thus was the preferred reaction pH. The slight Sb excess (over Fe) in the precipitate was likely due to co–precipitation of a secondary minor phase (possibly $Fe_3(SbO_4)_2$ or $FeSb_2O_4$), however, these could not be directly ascertained.

As the oxidation–precipitation reaction resulted in a poorly crystalline material, thermal treatments on the original precipitate, hydrothermal (200 °C) and calcination (950 °C), were employed to promote tripuhyite crystallization. Both treatments yielded products with increased crystallite size (BET surface area reduced from 165.1 m^2/g down to 130.5 m^2/g and 32.6 m^2/g respectively) and crystallinities, with calcination having a much higher degree of crystallinity than the hydrothermal treatment. Unfortunately, the calcined precipitate contained a secondary brizziite phase ($NaSbO_3$) due to sodium impurity that was not completely washed out of the original precipitate. This was deduced from washing prior to leachability/stability tests of the different precipitates. Thus, the calcined precipitate continued releasing antimony and sodium even after 5 wash cycles, while the hydrothermal precipitate did not show this trend. This is so owing to the nature of the hydrothermal treatment, where acidic water was used (pH = 1) that effectively removed all entrained elements in addition to enhancing particle crystallinity.

For comparison reasons, a reference material was synthesized by a modified solid state reaction (950 °C) involving goethite (FeOOH) and antimony pentoxide (Sb_2O_5) as starting powders (equimolar Sb(V) and Fe(III)) that yielded high purity and extremely high crystallinity tripuhyite.

From the leachability/stability tests the following can be concluded; (1) pseudo–equilibrium was attained by all materials in ~ 15 days (for controlled pH solutions) and 5 – 9 days (for "drift pH" solutions); (2) untreated precipitate released 119, 122, and 172 $mg \cdot L^{-1}$ Sb at pH 6, 7, and 8, respectively, hydrothermally treated precipitate released ~ 0.5 $mg \cdot L^{-1}$ Sb at all pH,

calcined precipitate released 10, 25 and 35 $mg \cdot L^{-1}$ Sb at pH 6, 7, and 8, respectively, and reference tripuhyite released less than 1 $mg \cdot L^{-1}$ Sb at all pH. The hydrothermally treated precipitate released 200 times less Sb than the untreated precipitate after pseudo–equilibrium, whereas the calcined precipitate was found to release 10 – 50 times more than the hydrothermally treated precipitate. Furthermore, Sb release from the hydrothermal product was comparable to the reference tripuhyite, even though the latter contained a higher degree of crystallinity, thus hydrothermal treatment was very effective in controlling antimony release. The elevated Sb release by the calcined precipitate was attributed to $NaSbO_3$ contamination; (3) comparing the stability of all precipitates over the pH range 6, 7, and 8, it was concluded that crystallinity (notwithstanding the presence of contaminating impurity phases) rather than pH is most critical.

Under the tested leachability conditions, the results suggest that the removal of antimony from aqueous solutions with post–precipitation hydrothermal treatment can yield a semi–crystalline tripuhyite material with very low solubility, releasing < 1 $mg \cdot L^{-1}$ Sb, and thus may be a viable option in fixing antimony from metallurgical waste streams.

5.2 Proposal for future research

Further to precipitation tests, post–reaction treatments, as well as tripuhyite leachability/stabilities studied and reported in this thesis, more research is required in order to characterize iron–antimony aqueous systems, especially where the synthesis of crystalline tripuhyite is concerned. The research presented thus far demonstrates the plausibility of removing antimony from concentrated aqueous solutions as crystalline tripuhyite (after thermal treatments), however, recommendations for future work are made to either clarify missing gaps or address several practical implementation issues: (1) characterize both solutions and solids as function of time during co–oxidation to ascertain the speciation of iron (Fe(II) vs. Fe(III)) and antimony (Sb(III) vs. Sb(V); (2) study the effectiveness of less costly oxidants (air and oxygen), hydrogen peroxide was used in the present work as a proof of concept and due to its decomposition issues, the study of other oxidants is suggested; (3) study tripuhyite precipitation in the presence of seed while controlling supersaturation in terms of pH and/or oxygen sparging, in order to promote particle growth and crystallization similar to scorodite systems (Demopoulos, 2005; Fujita et al., 2009); (4) to mitigate sodium impurity uptake during precipitation (due to NaOH), the

investigation of other common bases such as lime[21] or magnesia, is proposed; (5) examination of tripuhyite synthesis at various, in particular higher, antimony concentrations (>> 6 $g \cdot L^{-1}$) is suggested to reflect more concentrated industrial waste streams; (6) study the oxidation–precipitation reaction at room temperature (25 ^{o}C), 95 ^{o}C was used in the current study to promote mineral crystallization during precipitation, however, lower reaction temperatures are more industrially attractive due to lower energy demand; (7) optimize the interfacing of atmospheric precipitate formation, solid/liquid separation and hydrothermal treatment (lowering temperature and time); and (8) investigate direct precipitation of tripuhyite in an autoclave since hydrothermally treated precipitates were observed to be very stable (insoluble) and demonstrated better filterability.

[21] As alluded to earlier, in the presence of high calcium concentration, the roméite precursor $Ca[Sb(OH)_6]_2$ may also form during tripuhyite precipitation.

References

Accornero, M., Marini, L., & Lelli, M. (2008). The Dissociation Constant of Antimonic Acid at 10–40 °C. *Journal of Solution Chemistry*, *37*(6), 785–800.

Álvarez–Ayuso, E., Otones, V., Murciego, A, & García–Sánchez, A. (2013). Evaluation of different amendments to stabilize antimony in mining polluted soils. *Chemosphere*, *90*(8), 2233–9.

Anderson, C. G. (2001). Hydrometallurgically Treating Antimony–Bearing Industrial Wastes. *JOM*, 53(1), 18–20.

Anderson, C. G., & Twidwell, L. G. (2008). The alkaline sulfide hydrometallurgical separation, recovery and fixation of tin, arsenic, antimony, mercury and gold. *Lead and Zinc*, (3), 121–132.

Anderson, C. G. (2012). The Metallurgy of Antimony. *Chemie Der Erde – Geochemistry*, *72*(S4), 3–8.

Andreae, M. O., & Froelich, P. N. (1984). Arsenic, antimony, and germanium biogeochemistry in the Baltic Sea. *Tellus*, *36B*(2), 101–117.

Asai, T. (1975). Refinement of the Crystal Structure of Sodium Hexahydroxo–antimonate(V), $NaSb(OH)_6$. *Bulletin of the Chemical Society of Japan*, *48*(10), 2677–2679.

Awe, S. A., Sundkvist, J. –E., Bolin, N. –J., & Sandström, Å. (2013). Process flowsheet development for recovering antimony from Sb–bearing copper concentrates. *Minerals Engineering*, *49*, 45–53.

Aylmore, M., & Muir, D. (2001). Thiosulfate leaching of gold—A review. *Minerals Engineering*, *14*(2), 135–174.

Baes C.F., & Mesmer, R.S. (1986). *The Hydrolysis of Cations*. Florida, USA: R.E. Krieger Publishing Co., pp. 373.

Belzile, N., Chen, Y. –W., & Wang, Z. (2001). Oxidation of antimony(III) by amorphous iron and manganese oxyhydroxides. *Chemical Geology*, *174*, 379–387.

Belzile, N., Chen, Y. –W., & Filella, M. (2011). Human Exposure to Antimony: I. Sources and Intake. *Critical Reviews in Environmental Science and Technology*, *41*(14), 1309–1373.

Berlepsch, P., Armbruster, T., Brugger, J., Criddle, A. J., & Graeser, S. (2003). Tripuhyite, $FeSbO_4$ revisited. *Mineralogical Magazine*, *67*(1), 31–46.

Berry, F. J., Holden, J. G., Loretto, M. H., & Urch, D. S. (1987). Iron antimonate. *Journal of the Chemical Society, Dalton Transactions*, (7), 1727–1731.

Berry, F. J., & Ren, X. (2004). The formation of metal antimonates by mechanical milling and the conversion of α–Sb_2O_4 to β–Sb_2O_4. *Journal of Materials Science*, *39*(4), 1179–1183.

Blandamer, M.J., Burgess, J. & Peacock, R.D. (1974). Solubility of sodium hexahydroxoantimonate in water and in mixed aqueous solvents. *Journal of the Chemical Society, Dalton Transactions*, (10), 1084–1086.

Bluteau, M.-C., & Demopoulos, G. P. (2007). The incongruent dissolution of scorodite – Solubility, kinetics and mechanism. *Hydrometallurgy*, *87*(3–4), 163–177.

Brantley, S., Kubicki, J., & White., A. (2008). *Kinetics of Water–Rock Interaction* (pp. 292). Springer, New York, USA.

Canadian Council of Ministers of the Environment (1999), *Canadian Environmental Quality Objectives, Canadian National Ambient Air Quality Objectives: Appendix 1*. [Online]. Available: http://ceqg-rcqe.ccme.ca/download/en/133/. [Accessed: March, 2014].

Cao, H., Chen, J., Yuan, H., & Zheng, G. (2010). Preparation of pure SbCl3 from lead anode slime bearing high antimony and low silver. *Transactions of Nonferrous Metals Society of China*, *20*(12), 2397–2403.

Centi, G., & Trifiro, F. (1986). Oxidation Catalysts Based on Antimony Mixed Oxides with Rutile–Type Structures. *Catalysis Reviews*, *28*(2–3), 165–184.

Cornelis, G., Johnson, C. A., Gerven, T. Van, & Vandecasteele, C. (2008). Leaching mechanisms of oxyanionic metalloid and metal species in alkaline solid wastes: A review. *Applied Geochemistry*, *23*(5), 955–976.

Cornelis, G., Gerven, T. Van, Snellings, R., Verbinnen, B., Elsen, J., & Vandecasteele, C. (2011). Stability of pyrochlores in alkaline matrices: Solubility of calcium antimonate. *Applied Geochemistry*, *26*(5), 809–817.

Cornell, R.M., & Schwertmann, U. (2003). *The Iron Oxides: Structure, Properties, Reactions, Occurrence and Uses*. WILEY-VCH Verlag GmbH & Co. KGaA, Weinheim, Germany.

Council of the European Union, (1998). Council Directive 98/83/EC of 3 November 1998 on the quality of water intended for human consumption. *Official Journal L 330*, 05/12/1998, pp. 32–54. [Online]. Available: http://eur-lex.europa.eu/legal-content/EN/TXT/?uri=celex:31998L0083. [Accessed: September 2014].

Dabekaussen, R., Droppert, D., & Demopoulos, G.P. (2001). Ambient Pressure Hydrometallurgical Conversion of Arsenic Trioxide to Crystalline Scorodite. *CIM Bulletin*, *Vol. 94 (No. 1051),* 116–122.

Daenzer, R., Xu, L., Doerfelt, C., Jia, Y., & Demopoulos, G.P. (2014). Precipitation behaviour of As(V) during neutralization of acidic Fe(II)−As(V) solutions in batch and continuous modes. *Hydrometallurgy*, *146*, 40–47.

Demopoulos, G. P. (2005). On the preparation and stability of scorodite. *Arsenic Metallurgy, 2005 TMS Annual Meeting in San Francisco, California, U.S.A*, 25–50.

Demopoulos, G. P. (2009). Aqueous precipitation and crystallization for the production of particulate solids with desired properties. *Hydrometallurgy*, *96*(3), 199–214.

Diemar, G. A., Filella, M., Leverett, P., & Williams, P. A. (2009). Dispersion of antimony from oxidizing ore deposits. *Pure and Applied Chemistry*, *81*(9), 1547–1553.

Elleouet, C., Quentel, F., Madec, C. –L., & Filella, M. (2005). The effect of the presence of trace metals on the oxidation of Sb(III) by hydrogen peroxide in aqueous solution. *Journal of Environmental Monitoring*, *7*(12), 1220–5.

Filella, M., Belzile, N., & Chen, Y. (2002a). Antimony in the environment: a review focused on natural waters. I. Occurrence. *Earth–Science Reviews*, *57*, 125–176.

Filella, M., Belzile, N., & Chen, Y. (2002b). Antimony in the environment: a review focused on natural waters. II. Relevant solution chemistry. *Earth–Science Reviews*, *59*, 265–285.

Filella, M., & May, P. M. (2003). Computer simulation of the low–molecular–weight inorganic species distribution of antimony(III) and antimony(V) in natural waters. *Geochimica et Cosmochimica Acta*, *67*(21), 4013–4031.

Filella, M., Williams, P. a., & Belzile, N. (2009). Antimony in the environment: knowns and unknowns. *Environmental Chemistry*, *6*(2), 95.

Filippou, D., & Demopoulos, G. P. (1997). Arsenic Immobilization by Controlled Scorodite Precipitation. *Journal of the Minerals Metals & Materials Society*, *14*(12), 52–55.

Fujita, T., Taguchi, R., Abumiya, M., Matsumoto, M., Shibata, E., & Nakamura, T. (2009). Effect of pH on atmospheric scorodite synthesis by oxidation of ferrous ions: Physical properties and stability of the scorodite. *Hydrometallurgy*, *96*(3), 189–198.

Gannon, K., & Wilson, D. J. (1986). Removal of Antimony from Aqueous Systems. *Separation Science and Technology*, *21*(5), 475–493.

Gadgil, M. M., & Kulshreshtha, S. K. (1995). CO oxidation over Pd/$FeSbO_4$, catalyst. *Journal of Molecular Catalysis A: Chemical*, 211–222.

Gebel, T. (1997). Arsenic and antimony: comparative approach on mechanistic toxicology. *Chemico–Biological Interactions*, *107*(3), 131–44.

Government of Canada (2014). Schedule 4 – Metal Mining Effluent Regulations. Nov 25, 2014. [Online]. Available: http://laws-lois.justice.gc.ca/eng/regulations/SOR-2002-222/page-17.html#h-51. [Accessed: Dec. 1, 2014].

Guo, X., Wu, Z., & He, M. (2009). Removal of antimony(V) and antimony(III) from drinking water by coagulation–flocculation–sedimentation (CFS). *Water Research*, *43*(17), 4327–35.

He, M., Wang, X., Wu, F., & Fu, Z. (2012). Antimony pollution in China. *The Science of the Total Environment*, *421–422*(19), 41–50.

Helz, G. R., Valerio, M. S., & Capps, N. E. (2002). Antimony speciation in alkaline sulfide solutions: role of zerovalent sulfur. *Environmental Science & Technology*, *36*(5), 943–8.

Huang, Y., & Ruiz, P. (2005). Antimony dispersion and phase evolution in the Sb_2O_3–Fe_2O_3 system. *The Journal of Physical Chemistry. B*, *109*(47), 22420–5.

Huang, Y., & Ruiz, P. (2006). The nature of antimony–enriched surface layer of Fe–Sb mixed oxides. *Applied Surface Science*, *252*(22), 7849–7855.

IARC (1980). Antimony Trioxide and Antimony Trisulfide. *Lyon*, *47*, 291–305.

Jeffrey, M., & Anderson, C.G. (2003). A fundamental study of the alkaline sulfide leaching of gold. *The European Journal of Mineral Processing and Environmental Protection*, *3*(3), 336–343.

Johnson, C. A., Moench, H., Wersin, P., Kugler, P., & Wenger, C. (2005). Solubility of Antimony and Other Elements in Samples Taken from Shooting Ranges. *Journal of Environmental Quality*, *254*, 248–254.

Kabata–Pendias, A. (2011). *Trace Elements in Soils and Plants* (4th ed., p. 534). Boca Raton, Florida: CRC Press.

Keskinen, S. (2013). *Comparison of Cyanide and Thiosulphate Leaching for Gold Production (A Literature Review)*. Lappeenranta University of Technology, Finland.

Krause, E., & Ettel, V. A. (1989). Solubilities and Stabilities of Ferric Arsenate Compounds. *Hydrometallurgy*, *22*, 311–337.

Krupka, K. M., & Serne, R. J. (2002). *Geochemical Factors Affecting the Behavior of Antimony, Cobalt, Europium, Technetium, and Uranium in Vadose Sediments* (p. 95). Report – PNNL–14126.

Kyle, J. H., Breuer, P. L., Bunney, K. G., Pleysier, R., & May, P. M. (2011). Review of trace toxic elements (Pb, Cd, Hg, As, Sb, Bi, Se, Te) and their deportment in gold processing. Part I: Mineralogy, aqueous chemistry and toxicity. *Hydrometallurgy*, *107*(3–4), 91–100.

Langmuir, D., Mahoney, J., & Rowson, J. (2006). Solubility products of amorphous ferric arsenate and crystalline scorodite ($FeAsO_4 \cdot 2H_2O$) and their application to arsenic behavior in buried mine tailings. *Geochimica et Cosmochimica Acta*, *70*(12), 2942–2956.

Lauwers, L. F., Roelants, A., Rosseel, P. M., Heyndrickx, B., & Baute, L. (1990). Oral antimony intoxications in man. *Critical Care Medicine*, *18*(3), 324–6.

Le Berre, J. F., Gauvin, R., & Demopoulos, G. P. (2007). Characterization of Poorly-Crystalline Ferric Arsenate Precipitated from Equimolar Fe(III)-As(V) Solutions in the pH Range 2 to 8. *Metallurgical and Materials Transactions B*, *38*(5), 751–762.

Leuz, A. –K., & Johnson, C. A. (2005). Oxidation of Sb(III) to Sb(V) by O_2 and H_2O_2 in aqueous solutions. *Geochimica et Cosmochimica Acta*, *69*(5), 1165–1172.

Leuz, A. –K., Hug, S. J., Wehrli, B., & Johnson, C. A. (2006a). Iron–mediated oxidation of antimony(III) by oxygen and hydrogen peroxide compared to arsenic(III) oxidation. *Environmental Science & Technology*, *40*(8), 2565–71.

Leuz, A., Monch, H., & Johnson, C. A. (2006b). Sorption of Sb(III) and Sb(V) to Goethite: Influence on Sb(III) Oxidation and Mobilization. *Environmental Science & Technology*, *40*(23), 7277–7282.

Leverett, P., Reynolds, J. K., Roper, A. J., & Williams, P. A. (2012). Tripuhyite and schafarzikite: two of the ultimate sinks for antimony in the natural environment. *Mineralogical Magazine*, *76*(4), 891–902.

Lide, D.R., Taylor and Francis, Boca Raton, FL (2007), "The Elements", in *CRC Handbook of Chemistry and Physics, (87th Edition).*

Lin, C. C., Smith, F. R., Ichikawa, N., Baba, T., & Itow, M. (1991). Decomposition of Hydrogen Peroxide in Aqueous Solutions at Elevated Temperatures. *International Journal of Chemical Kinetics*, *23*(11), 971–987.

Mitsunobu, S., Takahashi, Y., Terada, Y., & Sakata, M. (2010). Antimony(V) incorporation into synthetic ferrihydrite, goethite, and natural iron oxyhydroxides. *Environmental Science & Technology*, *44*(10), 3712–8.

Mitsunobu, S., Takahashi, Y., Utsunomiya, S., Marcus, M. A., Terada, Y., Iwamura, T., & Sakata, M. (2011). Identification and characterization of nanosized tripuhyite in soil near Sb mine tailings. *American Mineralogist*, *96*(7), 1171–1181.

Mosselmans, J. F. W., Helz, G. R., Pattrick, R. A. D., Charnock, J. M., & Vaughan, D. J. (2000). A study of speciation of Sb in bisulfide solutions by X–ray absorption spectroscopy. *Applied Geochemistry*, *15*, 879–889.

Nag, P., Banerjee, S., Lee, Y., Bumajdad, A., Lee, Y., & Devi, P. S. (2012). Sonochemical Synthesis and Properties of Nanoparticles of FeSbO4. *Inorganic Chemistry*, *51*(2), 844 – 850.

Oh, S. J., Cook, D. C., & Townsend, H. E. (1998). Characterization of iron oxides commonly formed as corrosion products on steel. *Hyperfine Interactions*, *112*, 59–65.

Okkenhaug, G., Zhu, Y. –G., Luo, L., Lei, M., Li, X., & Mulder, J. (2011). Distribution, speciation and availability of antimony (Sb) in soils and terrestrial plants from an active Sb mining area. *Environmental Pollution*, *159*(10), 2427–34.

Okkenhaug, G., Breedveld, G. D., Kirkeng, T., Lægreid, M., Mæhlum, T., & Mulder, J. (2013). Treatment of air pollution control residues with iron rich waste sulfuric acid: does it work for antimony (Sb)? *Journal of Hazardous Materials*, *248–249*, 159–66.

Olmi, F., & Sabelli, C. (1994). Brizziite, $NaSbO_3$, a new mineral from the Cetine mine (Tuscany, Italy): description and crystal structure. *European Journal Mineralogy*, (6), 667–672.

Pacyna, J.M., and Pacyna, E.G. (2001). An assessment of global and regional emissions of trace metals to the atmosphere from anthropogenic sources worldwide. *Environmental Reviews, 9*(4), 269–298.

Quentel, F., & Filella, M. (2002). Determination of inorganic antimony species in seawater by differential pulse anodic stripping voltammetry: stability of the trivalent state. *Analytica Chimica Acta*, *452*(2), 237–244.

Quentel, F., Filella, M., Elleouet, C., & Madec, C. –L. (2004). Kinetic studies on Sb(III) oxidation by hydrogen peroxide in aqueous solution. *Environmental Science & Technology*, *38*(10), 2843–8.

Ratke, L., Voorhees, P. W. (2002). *Growth and Coarsening: Ostwald Ripening in Material Processing* (pp. 117–118). Springer, Berlin.

Rawat, J. P., & Singh, D. K. (1976). Synthesis, ion–exchange properties and analytical applications of Iron(III) Antimonate. *Analytica Chimica Acta*, *87*, 157–162.

Rawat, J. P., & Singh, B. (1984). Ion Exchange Equilibria between Alkali Metals and Hydrogen Ions on Iron(III) Antimonate, an Inorganic Ion Exchanger. *The Chemical Society of Japan*, *57*(3), 862–865.

Roper, A. J., Williams, P. A., & Filella, M. (2012). Secondary antimony minerals: Phases that control the dispersion of antimony in the supergene zone. *Chemie Der Erde – Geochemistry*, *72*(S.4), 9–14.

Sasaki, Y. (2000). Preparation and performance of iron antimonate catalysts for fluid–bed ammoxidation. *Applied Catalysis A: General*, *194–195*, 497–505.

Schwertmann, U., & Fechter, H. (1994). The formation of green rust and its transformation to lepidocrocite. *Clay Minerals*, *29*(1), 87–92.

Selim, H. M. (Ed.). (2012). *Competitive Sorption and Transport of Heavy Metals in Soils and Geological Media Sorption*. Florida, USA: CRC Press, pp. 119–145.

Sherman, D. M., Ragnarsdottir, K. V., & Oelkers, E. H. (2000). Antimony transport in hydrothermal solutions : an EXAFS study of antimony (V) complexation in alkaline sulfide and sulfide – chloride brines at temperatures from 25 C to 300 ^{o}C at Psat. *Chemical Geology*, *167*, 161–167.

Shortland, A. J. (2002). The use and origin of antimonate colorants in early Egyptian glass. *Archaeometry*, *44*(4), 517–530.

Sugimoto, T. (1987). Preparation of Monodispersed Colloidal Particles. *Advances in Colloid and Interface Science*, *28*, 65–108.

Swaminathan, K., & Sreedharan, O. M. (2003). High temperature stabilities of interoxides in the system Fe–Sb–O and their comparison with the interoxides in other M–Sb–O (M=Cr, Ni or Co) systems. *Journal of Alloys and Compounds*, *358*, 48–55.

Tella, M., & Pokrovski, G. S. (2012). Stability and structure of pentavalent antimony complexes with aqueous organic ligands. *Chemical Geology*, *292–293*, 57–68.

Teller, G., Brazdil, F., Grasselli, K., & Sohio, T. (1985). Phase cooperation in oxidation catalysis. Structural studies of the iron antimonate–antimony oxide system. *Journal of the Chemical Society, Faraday Transactions 1: Physical Chemistry in Condensed Phases*, *81*, 1693–1704.

Tianshu, Z., & Hing, P. (1999). $FeSbO_4$ semiconductor ceramics : a new material for sensing liquid–petroleum gas. *Journal of Materials Science: Materials in Electronics*, *10*, 509–518.

Tojo, T., Zhang, Q., & Saito, F. (2008). Mechanochemical synthesis of $FeSbO_4$–based materials from FeOOH and Sb_2O_5 powders. *Powder Technology*, *181*(3), 281–284.

Ubaldini, S., Vegliò, F., Fornari, P., & Abbruzzese, C. (2000). Process flow–sheet for gold and antimony recovery from stibnite. *Hydrometallurgy*, *57*(3), 187–199.

United States Environmental Protection Agency. (1998). Toxics Release Inventory. USEPA, Washington, DC, USA, Doc. 745–R–00–007.

United States Environmental Protection Agency. (1999). National Primary Drinking Water Standards. USEPA Office of Water, Washington, DC, USA, Doc. 810–F–94–001.

U.S. Geological Survey. (2014). *Mineral commodity summaries 2014*. U.S. Geological Survey.

Vink, B. W. (1996). Stability relations of antimony and arsenic compounds in the light of revised and extended E_h–pH diagrams. *Chemical Geology*, *130*(1–2), 21–30.

WHO. (2006). *Guidelines for Drinking–water Quality.* 3rd Edition. World Health Organization, Geneva (Vol. 1, p. 595).

Wilson, N. J., Craw, D., & Hunter, K. (2004). Antimony distribution and environmental mobility at an historic antimony smelter site, New Zealand. *Environmental Pollution*, *129*(2), 257–66.

Wilson, S. C., Lockwood, P. V, Ashley, P. M., & Tighe, M. (2010). The chemistry and behaviour of antimony in the soil environment with comparisons to arsenic: a critical review. *Environmental Pollution*, *158*(5), 1169–81.

Wu, Z., He, M., Guo, X., & Zhou, R. (2010). Removal of antimony(III) and antimony(V) from drinking water by ferric chloride coagulation: Competing ion effect and the mechanism analysis. *Separation and Purification Technology*, *76*(2), 184–190.

Zakaznova–Herzog, V. P., & Seward, T. M. (2006). Antimonous acid protonation/deprotonation equilibria in hydrothermal solutions to 300°C. *Geochimica et Cosmochimica Acta*, *70*(9), 2298–2310.

Appendix

Fe(II) titration procedure

Slurry samples were digested in HCl solution prior to titration. The procedure involved the following steps:

Step 1 – Add 20 mL of concentrated HCl into a 250 mL Erlenmeyer flask, ensure an inert atmosphere in the flask (i.e. purge with nitrogen gas or work under vacuum)

Step 2 – Digest 1 mL of slurry/filtrate into the flask

Step 3 – Dilute the mixture with 50 to 100 mL of deionised water (add slowly)

Step 4 – Add 25 mL of mixed acid (15% v/v H_3PO_4, 15% v/v H_2SO_4) into the mixture

Step 5 – Add 5 – 10 drops of sodium diphenylamine sulfonate indicator

Step 6 – Titrate the solution against a known concentration of $K_2Cr_2O_7$ titrant (i.e. 0.01 N)

Step 7 – Calculate Fe(II) concentration in the sample from the volume of titrant used by the following Equation:

$$[\text{Fe(II)}]\left(\frac{\text{g}}{\text{L}}\right) = MW_{Fe} \cdot N_{K2Cr2O7}\,(\text{N}) \cdot \frac{\text{Volume of titrant used (mL)}}{\text{Volume of sample used (mL)}}$$

* $MW_{Fe} = 55.847\left(\frac{\text{g}}{\text{mole}}\right)$

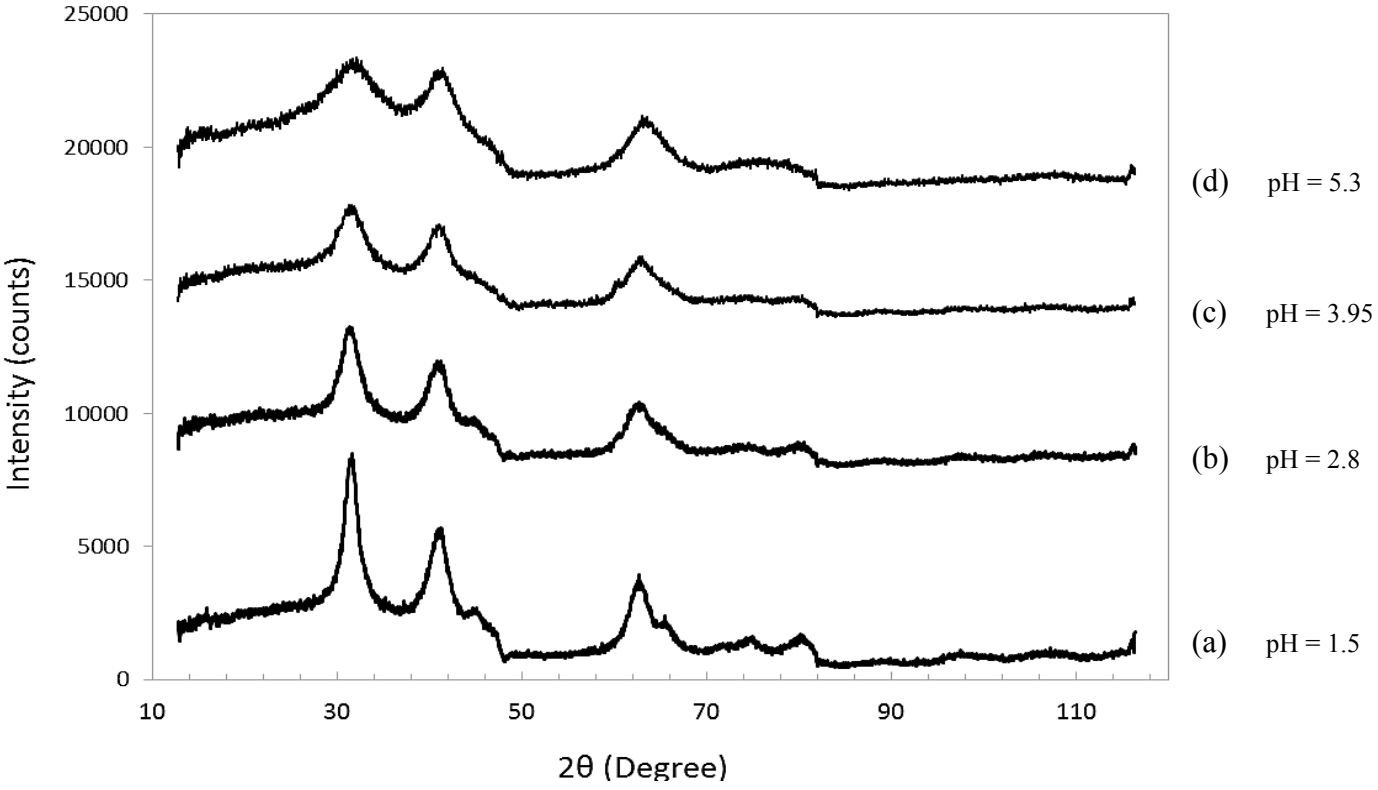

Figure A.1 – *X–ray powder diffraction patterns of the precipitates produced at different pH are given (counts), supplementary to Figure 4.4 (Section 4.2); (a) pH = 1.5, (b) pH = 2.8, (c) pH = 3.95, (d) pH = 5.3.*

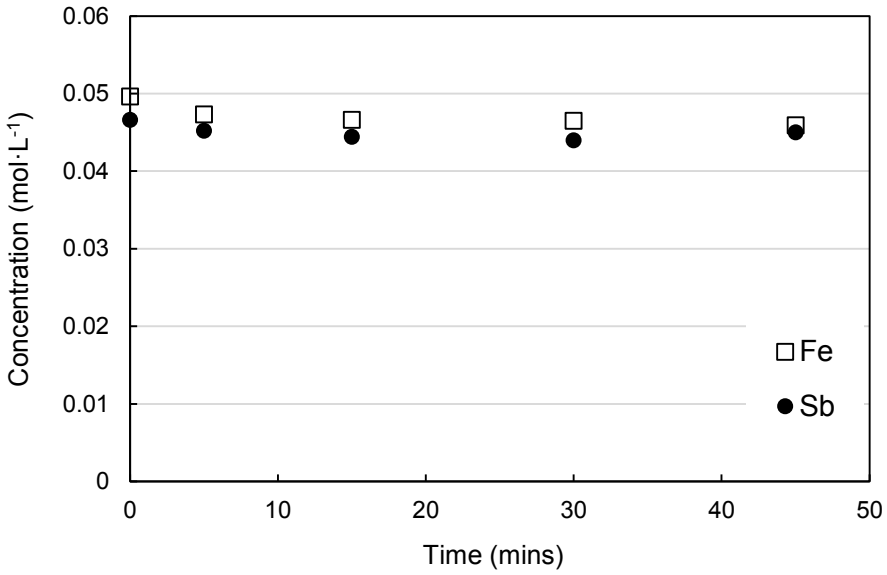

Figure A.2 – *Antimony(III) and iron(II) concentrations (mol·L^{-1}), constant pH 5.3, 95 °C, no oxidant used, supplementary to Figure 4.6 (Section 4.3).*

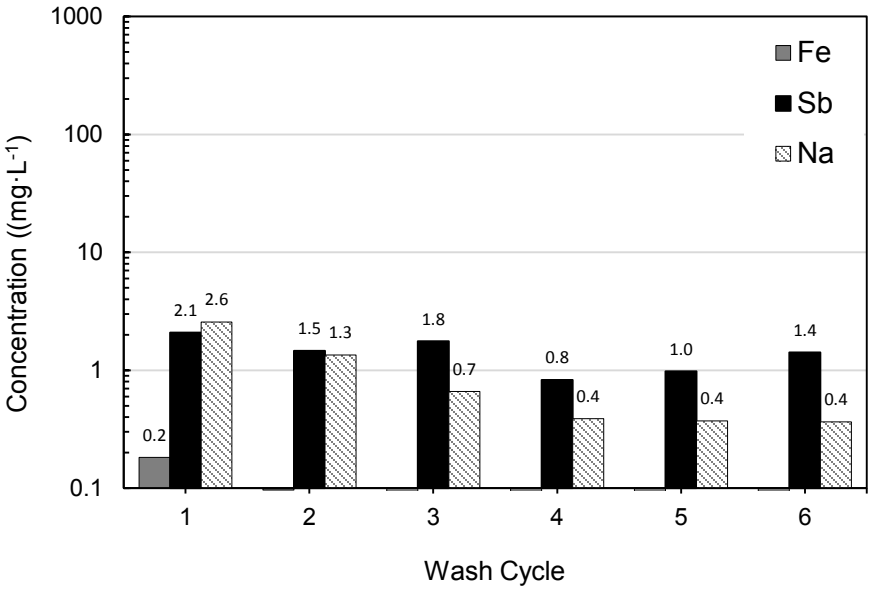

Figure A.3 – *Figure 4.18 (Section 4.4) data is presented with numerical iron, antimony and sodium filtrate concentrations at different wash cycles for the calcined precipitate.*

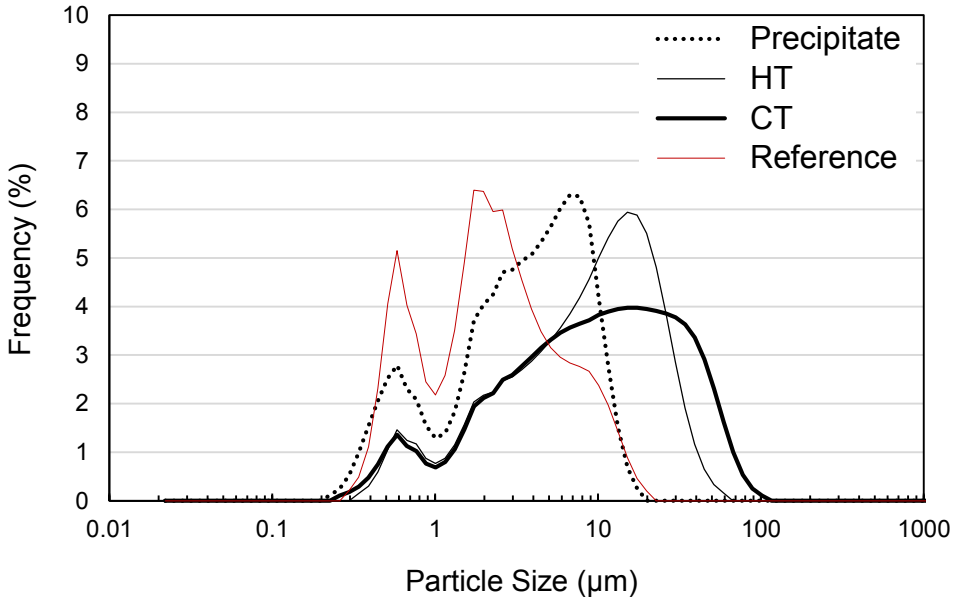

Figure A.4 – *Particle size distribution of all 4 materials (Chapter 4, Section 4.6); (1) untreated precipitate; (2) hydrothermally treated precipitate (HT); (3) calcined precipitate (CT), and synthetic tripuhyite (reference).*

Table A.1 – *In reference to Chapter 2 (Section 2.8), best stability constant values for all acid–base and oxide antimony species are presented, adapted from Filella and May (2003). Note, pKa = – log β.*

Reaction	log β
$Sb(OH)_3^0 + 6H^+ + 6e^- = 3H_2O + \mathbf{SbH_3(g)}$	−13.62
$2Sb(OH)_3^0 = 3H_2O + \mathbf{Sb_2O_3(s)}$	8.480
$Sb(OH)_3^0 = \mathbf{Sb(OH)_3(s)}$	0.2327
$2Sb(OH)_3^0 = 3H_2O + \mathbf{Sb_2O_3(cubic,s)}$	11.44
$2Sb(OH)_3^0 = 3H_2O + \mathbf{Sb_2O_3(rhombic,s)}$	10.00
$Sb(OH)_3^0 = H_2O + \mathbf{SbOOH(s)}$	4.371
$2Sb(OH)_3^0 = 2H^+ + 2e^- + 2H_2O + \mathbf{Sb_2O_4(s)}$	−1.680
$4Sb(OH)_3^0 = 6H_2O + \mathbf{Sb_4O_6(s)}$	18.53
$2Sb(OH)_3^0 = 4e^- + 4H^+ + H_2O + \mathbf{Sb_2O_5(s)}$	−37.26
$4Sb(OH)_3^0 = 6H_2O + \mathbf{Sb_4O_6(rhombic,s)}$	17.71
$4Sb(OH)_3^0 = 6H_2O + \mathbf{Sb_4O_6(cubic,s)}$	18.56
$Sb(OH)_3^0 + 3H^+ + 3e^- = 3H_2O + \mathbf{Sb(s)}$	12.26
$Sb(OH)_3^0 + 3H^+ = 3H_2O + \mathbf{Sb^{3+}}$	−0.01864
$Sb(OH)_3^0 + 2H^+ = 2H_2O + \mathbf{Sb(OH)^{2+}}$	1.190
$Sb(OH)_3^0 + H^+ = H_2O + \mathbf{Sb(OH)_2^+}$	1.371
$2Sb(OH)_3^0 + 4H^+ = 4H_2O + \mathbf{Sb_2(OH)_2^{4+}}$	3.545
$Sb(OH)_3^0 + H_2O = H^+ + \mathbf{Sb(OH)_4^-}$	−11.70
$Sb(OH)_3^0 + H_2O = 2e^- + H^+ + \mathbf{Sb(OH)_4^+}$	−24.61
$Sb(OH)_3^0 + 2H_2O = 2e^- + 2H^+ + \mathbf{Sb(OH)_5^0}$	−22.33
$Sb(OH)_3^0 + 3H_2O = 2e^- + 3H^+ + \mathbf{Sb(OH)_6^-}$	−25.15

Table A.2 – *In reference to Chapter 2 (Section 2.8), best stability constant values for all antimony–sulfide species are presented, reproduced from Filella and May (2003). Note, pKa = – log β.*

Reaction	log β
$2Sb(OH)_3^0 + 3S^{2-} + 6H^+ = 6H_2O + \mathbf{Sb_2S_3(s)}$	91.83
$2Sb(OH)_3^0 + 4S^{2-} + 7H^+ = 6H_2O + \mathbf{Sb_2HS_4^-}$	102.4
$2Sb(OH)_3^0 + 4S^{2-} + 6H^+ = 6H_2O + \mathbf{Sb_2S_4^{2-}}$	90.94
$2Sb(OH)_3^0 + 4S^{2-} + 8H^+ = 6H_2O + \mathbf{Sb_2H_2S_4^0}$	105.9
$2Sb(OH)_3^0 + 2S^{2-} + 4H^+ = 4H_2O + \mathbf{Sb_2(OH)_2S_2}$	57.67
$Sb(OH)_3^0 + 3S^{2-} + 3H^+ = 3H_2O + \mathbf{SbS_3^0}$	46.80
$Sb(OH)_3^0 + 2S^{2-} + 3H^+ = 3H_2O + \mathbf{SbS_2^-}$	47.92
$4Sb(OH)_3^0 + 7S^{2-} + 12H^+ = 12H_2O + \mathbf{Sb_4S_7^{2-}}$	183.2
$Sb(OH)_3^0 + 4S^{2-} + 3H^+ = 3H_2O + 2e^- + \mathbf{SbS_4^{3-}}$	68.20
$Sb(OH)_3^0 + S^{2-} + H^+ = H_2O + \mathbf{Sb(OH)_2S^-}$	14.78

Experimental data for the oxidation – precipitation tests presented in Figures 4.3 and 4.9 (Chapter 4 – Section 4.2 and 4.3, respectively) are presented in Tables A.3 – A.6.

Table A.3 – *Iron and antimony concentration data over 3 – 3.5 hrs of oxidation time at constant pH 1.5.*

Sample #	Time (min)	Fe (mol/L)	Sb (mol/L)
1	0	0.0508	0.0509
2	5	0.0505	0.0470
3	16	0.0504	0.0400
4	40	0.0487	0.0254
5	60	0.0485	0.0189
6	90	0.0479	0.0122
7	120	0.0338	0.0032
8	150	0.0193	0.0025
9	165	0.0177	0.0019
10	180	0.0171	0.0019
11	195	0.0167	0.0017
12	210	0.0165	0.0018

Table A.4 – *Iron and antimony concentration data over 3 – 3.5 hrs of oxidation time at constant pH 2.8.*

Sample #	Time (min)	Fe (mol/L)	Sb (mol/L)
1	0	0.0500	0.0495
2	7	0.0493	0.0462
3	14	0.0491	0.0450
4	26	0.0488	0.0421
5	46	0.0425	0.0362
6	65	0.0385	0.0325

Sample #	Time (min)	Fe (mol/L)	Sb (mol/L)
7	85	0.0307	0.0244
8	105	0.0232	0.0180
9	125	0.0126	0.0111
10	155	0.0068	0.0006
11	185	0.0162	0.0000
12	215	0.0152	0.0000

Table A.5 – *Iron and antimony concentration data over 3 – 3.5 hrs of oxidation time at constant pH 3.95.*

Sample #	Time (min)	Fe (mol/L)	Sb (mol/L)
1	0	0.0500	0.0500
2	3	0.0496	0.0496
3	11	0.0493	0.0467
4	30	0.0407	0.0346
5	60	0.0321	0.0261
6	90	0.0185	0.0171
7	120	0.0042	0.0088
8	150	0.0102	0.0000
9	165	0.0141	0.0000
10	180	0.0149	0.0000
11	195	0.0145	0.0000
12	210	0.0147	0.0000

Table A.6 – *Iron, antimony, sodium (actual and calculated) concentration data over 3 – 3.5 hrs of oxidation time at constant pH 5.3.*

Sample #	Time (min)	Fe (mol/L)	Sb (mol/L)	Na - actual (mol/L)	Na - calculated (mol/L)
1	0	0.0490	0.0490	0.0230	0.0210
2	5	0.0478	0.0444	0.0305	0.0310
3	15	0.0436	0.0371	0.0442	0.0410
4	40	0.0319	0.0236	0.0627	0.0635
5	60	0.0201	0.0128	0.0733	0.0755
6	90	0.0088	0.0088	0.0744	0.0815
7	122	0.0061	0.0027	0.0922	0.1040
8	165	0.0080	0.0003	0.0962	0.1090
9	180	0.0076	0.0002	0.0914	0.1090
10	195	0.0074	0.0002	0.0893	0.1090